Syracuse University

SURFACE

Dissertations - ALL   SURFACE

1-1-2015

Investigation of Electrostatic Assembly of Gold Nanoparticles Mediated by Giant Polyoxomolybdate Clusters

Jonathan Gooch
Syracuse University

Follow this and additional works at: https://surface.syr.edu/etd

Part of the Physical Sciences and Mathematics Commons

Recommended Citation

Abstract

Nanoscience has shifted its focus from studying properties of individual nanoparticles toward using these nanoparticles as building blocks to assemble larger systems. One approach to this end is to exploit electrostatic self-assembly through the interaction of oppositely charged nanoparticles to form larger superstructures and even crystalline superlattices. Metal nanoparticles, such as gold, have been used to design such structures, but understanding the mechanics of the self-assembly can be elusive due to their random size and charge distributions. However, a certain class of polyoxomolybdates can provide insights into how electrostatic self-assembly occurs with their precise size dimensions and charges.

In the first investigation, the electrostatic assembly between a series of the differently charged polyoxomolybdate-type Keplerates of

$(NH_4)_{42}[\{(Mo^{VI})Mo^{VI}_5O_{21}(H_2O)_6\}_{12}\{Mo^V_2O_4(CH_3COO)\}_{30}] \cdot \approx 300\ H_2O \cdot \approx 10\ CH_3COONH_4$ (Mo-132a), $(NH_4)_{72}[\{(Mo^{VI})Mo^{VI}_5O_{21}(H_2O)_6\}_{12}\{Mo^V_2O_4(SO_4)\}_{30}] \cdot \approx 200\ H_2O$ (Mo-132b) and $Na_{10}(NH_4)_{62}[\{(Mo^{VI})Mo^{VI}_5O_{21}(H_2O)_6\}_{12}\{Mo^V_2O_4(HPO_4)\}_{30}] \cdot \approx 300\ H_2O \cdot \approx 2Na^+ \cdot \approx 2NH_4^+ \cdot \approx 4\ H_2PO_4$ (Mo-132c) with cationic gold nanoparticles (AuNPs) was explored for the first time. The rapid electrostatic assembly from nanoscopic entities to micron scale aggregates was observed upon precipitation, which closely matched the point of aggregate electroneutrality. Successful assembly was demonstrated using UV–vis, DLS, TEM, and zeta-potential analysis. Results indicate that the point at which precipitation occurs is related to charge balance or electroneutrality, and that counter-ions at both the Mo-132 and AuNP play a significant role in assembly.

The subsequent investigation, focused on certain counterintuitive results of the previous study of Mo-132 and AuNP aggregates by manipulating the AuNP core diameter. We hypothesized that a AuNP core diameter of comparable size to Mo-132 would lower the r_{E0} (equivalence molar ratio, r = [Mo-132]:[Au]) between the nanomaterials, whereas a larger AuNP core would raise the r_{E0}. The range of sizes allowed assessment of how counter-ions affect assembly based on comparable dimensions of the nanomaterials. It was found that a smaller AuNP core size of 1.6 nm produced the naively anticipated results based on charge yielding a r_{E0}, molar ratio of ca. 1.0 at electroneutrality. However, even at this favorable r_{E0} unorganized aggregates were observed. These findings suggested that crystallization could not be based on charge considerations alone, but that the size relation between the nanomaterials must also be taken into account to induce crystallization.

In the last investigation, the electrostatic self-assembly of the polyoxomolybdate $(NH_4)_{28}[Mo_{154}(NO)_{14}O_{420}(OH)_{14}(H_2O)_{70}] \cdot 350\ H_2O$ (Mo-154) and AuNPs of different size was studied to explore the aspect of asymmetry in these colloidal systems. The aim of this work was to observe the dependence electrostatic interactions may have on asymmetric shaped nanomaterials. The ring-shaped Mo-154 structure gave this study a unique view on how the polarity of electron density can affect the molar ratio, r = [Mo-154]:[Au]. It was shown that the van der Waals attraction forces of Mo-154, in comparison to Mo-132, were stronger resulting in a lower r_{E0}.

Investigation of Electrostatic Assembly of Gold Nanoparticles

Mediated by Giant Polyoxomolybdate Clusters

by

Jonathan W. Gooch

B.S. Misericordia University, 2010

DISSERTATION

Submitted to the Department of Chemistry in partial
fulfillment of the requirements for the degree of

Doctor of Philosophy in *Chemistry*

Syracuse University
August 2015

Acknowledgements

I would like to express my deepest gratitude for my advisor, Dr. Jon Zubieta, for his guidance, patience and inspiration throughout my graduate career. I am very thankful for all he has done for my growth as a student, chemist, and person.

I would like to express my great appreciation for my collaborator, Dr. Mathew Maye, who has bestowed upon me his guidance, patience, and wisdom for the field of nanoscience. I am very thankful for all his advice and guidance in pursuing my career beyond Syracuse University.

I would like to thank the members of my committee, Dr. Kevin Sweder, Dr. James Spencer, Dr. Karin Ruhlandt, Dr. Mathew Maye and Dr. Michael Sponsler for their support and time during the defense process. I would especially like to thank Dr. James Spencer and Dr. Karin Ruhlandt for their guidance during my time at Syracuse University.

I would like to acknowledge both the Zubieta and Maye lab group members, past and present, who provided their own wisdom and insight throughout my graduate career. I would also like to thank past undergraduate and REU students that I have had the pleasure of working with and mentoring, including Candace Benjamin, Stephanie Luquis, and Shannon Walter.

I would like to acknowledge all of the friends that I have made throughout my years at Syracuse University. You all have gotten me through the ups and downs of graduate school. Without you all, I would have lost my sanity a long time ago. Special thanks to the Hougland lab for their craziness, laughter, and free spirits to lighten the weight graduate school can place on a person.

I am very thankful for my fiancée, Kayleigh, whose support, patience, and love has guided me through this process. She has never stopped believing in me, motivating me, and giving me the strength to be the best person I can be every day. Her companionship has made this journey one of the most memorable. I would also like to thank my future in-laws, the McGoverns, Bubbins, and all of my future extended family for their support and encouragement.

Finally, I would not be the person I am today without my family. My parents, Adrian and Marie Gooch, have guided me since my first steps in this world. Their guidance, support, patience, and understanding throughout the years have been the biggest reason I got to where I this point in my life and I could not be any more appreciative. To my sisters, Megan and Jennifer, for just being my sisters, always having my back, and just always being there for me. Lastly, all of my extend family for their support and encouragement.

Table of Contents

Chapter 4: Electrostatic Assembly of Gold Nanoparticles Meditated by $(NH_4)_{28}[Mo_{154}(NO)_{14}O_{420}(OH)_{14}(H_2O)_{70}] \cdot 350\ H_2O$ (Mo-154)

Chapter 5: Conclusions and Future Outlook

List of Figures

acid capped gold nanoparticles (AuMUA). Aggregation occurs upon charge balancing of the individual entities. Reprinted with permission from reference 118. Copyright 2006 American Chemical Society.

Figure 5.1: Illustration of the density of states. For bulk metals, condensed energy levels lead to formation of the valence and conduction band. As diameter of particles decreases, these energy levels separate and form discrete energy levels which yield a band gap (E_g).

List of Schemes

List of Tables

Abbreviations

A	Hamaker constant
AgNPS	Silver Nanoparticles
AuNPs	Gold Nanoparticles
AuTMA	Gold Nanoparticles capped with TMA (see abbrev.)
D_h	Hydrodynamic radius
DLS	Dynamic Light Scattering
ε	molar absorptivity
HOPG	Highly Ordered Pyrolytic Graphite
IVCT	Intervalence Charge Transfer
Mo-132	Keplerate clusters
Mo-132a	$(NH_4)_{42}[\{(Mo^{VI})Mo^{VI}_5O_{21}(H_2O)_6\}_{12}\{Mo^V_2O_4(CH_3COO)\}_{30}] \cdot \approx 300\ H_2O \cdot \approx 10\ CH_3COONH_4$
Mo-132b	$(NH_4)_{72}[\{(Mo^{VI})Mo^{VI}_5O_{21}(H_2O)_6\}_{12}\{Mo^V_2O_4(SO_4)\}_{30}] \cdot \approx 200\ H_2O$
Mo-132c	$Na_{10}(NH_4)_{62}[\{(Mo^{VI})Mo^{VI}_5O_{21}(H_2O)_6\}_{12}\{Mo^V_2O_4(HPO_4)\}_{30}] \cdot \approx 300\ H_2O \cdot \approx 2Na^+ \cdot \approx 2NH_4^+ \cdot \approx 4\ H_2PO_4$
Mo-154	$(NH_4)_{28}[Mo_{154}(NO)_{14}O_{420}(OH)_{14}(H_2O)_{70}] \cdot 350\ H_2O$
MUA	11-mercaptoundecanoic acid
NP	Nanoparticle
POMs	Polyoxomolybdates or Polyoxometalates
Q	Charge
R	internuclear separation distance
r	[POM]:[Au]
r_{E0}	[POM]:[Au] at equivalence point
SAM	Self-assembled monolayer

SEM	Scanning electron microscope
SPR	Surface plasmon resonance
TEM	Transmission electron microscope
TGA	Thermogravimetric Analysis
TMA	N,N,N-trimethyl(11-mercapto)undecylammonium chloride
TOAB	Tetraoctylammonium bromide
UV-vis	Ultraviolet-visible spectroscopy
XPS	X-ray photoelectron spectroscopy
Vdw	van der Waals
ζ-Pot.	Zeta potential

Chapter 1

Introduction

1.1   Nanoparticles: What Makes the Nanoscale Unique?

Today, the scientific community generally agrees that nanomaterials, by definition, are chemical substances or materials with dimensions between 1and 100 nm.[1] This size regime positions these materials between the molecular scale of individual atoms and the macro scale of bulk materials. Although new, the history of nanomaterials begins with nature providing us with the nanomaterial DNA.[2] With a separation of only 0.3 nm, base pairs of DNA store information that allows for organisms to perform specific functions, such as, movement and reproduction. In 1959, Richard P. Feynman, a physicist at Cal Tech, anticipated the advent of nanomaterials. In one of his classes he said, "There is plenty of room at the bottom," and suggested that scaling down to nanoscale and starting from the bottom was the key to future technology and advancement.[3] Over 20 years later, the scientific community began to embrace the expansion of the nanomaterial world. This was due in large part to the advances in microscopic instrumentation, such as TEM and SEM, allowing the unique properties nanomaterials possess to be observed.[3-4]

Nanomaterials possess very unique physiochemical properties related to their surface area and quantum confinement that affect their physical[5], optical[6], electronic[7], and magnetic[8] properties. It is equally noteworthy that these properties change with their size and/or shape.[9-10] For example, nanomaterials consisting of high surface-to-volume ratios possess higher reactivity, which paired with the ability to change size and shape potentially allows for better catalysts.[3,9] For semiconductors, quantum confinement of the electronic motion to a length scale is comparable to or smaller than that of bulk material. For noble metals that are tens of nanometers in size, a strong absorption is observed resulting from a collective oscillation of the electrons in

the conduction band from one particle surface to another.[9] This phenomenon known as Surface Plasmon Resonance will be further discussed in Section 1.2.3.

1.2   Gold Nanoparticles

1.2.1   History

Gold has always been placed on the highest pedestal of the noble metals. Since the Copper Age, gold has been known by artisans and has been considered a highly desired metal for coinage, jewelry, and other arts. Colloidal gold first appeared around the 5th century in China and Egypt.[11] The vibrant colors displayed by colloidal gold has been used to produce decorative stained glass for windows and pottery glazes dating back to mediaeval times and earlier. The most famous examples of these are the Lycurgus Cup (**Fig. 1.1**) and the pigment "Purple of Cassius".[11-13]

Figure 1.1: Photographs of the famous Lycurgus Cup from the 4th century Roman Empire, where a jade hue is observed in reflected light. However, vibrant ruby red to violet shades appear from transmitted light through the cup.

As for gold nanoparticles (AuNPs), they are well-documented in the scientific world. In 1857, Faraday investigated colloidal gold, noting the unusually prominent red color in contrast to the yellow appearance of bulk gold. He observed the formation of deep red solutions of colloidal gold by reduction of an aqueous solution of $AuCl_4^-$ using phosphorus in CS_2.[14] Starting in the 20th century, the first colloidal gold in a dilute solution was prepared by Richard Adolf Zsigmondy.[15] Gold synthetic methodology has blossomed since the early 1950's and includes the Turkevich[11] and Brust-Schiffrin[12] methods. While these methods set the foundation for colloidal gold synthesis, novel syntheses have flourished greatly in recent years. These advances exploit the strong affinity various ligands containing functional groups such as thiols, phosphines, and amines exhibit for the gold surface.[16-17]

1.2.2   Synthetic Methods for Gold Nanoparticles

Synthetic methods for developing AuNPs have only been developed within the last 100 years. The main feature of these methods follows a similar pattern that starts out with the reduction of Au^{+3} to Au^0, typically using the gold salt $HAuCl_4^-$. Nucleation begins with the growth of unbound Au^0 atoms or aggregation of unreacted metal species onto the nuclei to form seeds.[18] The final composition of AuNPs is comprised of Au^0 atoms surrounded by an outer layer of negative ions. This layer can be $[AuCl_2]^-$ ions, borohydride ions or citrate ions which are used to control the size of the nanoparticles. These ions increase the electrostatic interactions between AuNPs which stabilize and prevent further growth. AuNPs typically take on a face centered cubic (fcc) crystal lattice and have a size domain of 1-200 nm depending on reaction conditions.[18,19]

4

Likely the most widely used method today was first described by J. Turkevich[16,17,20] in 1951. The synthetic design allows for large scale reactions that yield a high degree of monodisperse gold-citrate nanoparticles by using trisodium citrate as a reducing agent as well as a stabilizing ligand. In 1973, Frens[16, 17, 21] refined the Turkevich method by varying the ratio of trisodium citrate and $HAuCl_4^-$ which typically yields nanoparticles ranging from 5-200 nm.[17, 22]

In 1994, Mathias Burst and David J. Schiffrin developed a two-phase synthesis in which stabilized monodisperse AuNPs could be produced. In their method, an organically soluble capping ligand, such as tetraoctylammonium bromide ($N(C_8H_{15})_4Br$), is used to phase transfer $AuCl_4^-$ from the aqueous phase to organic layer.[23] Typically, an alkane-thiolate[17] is used as a stabilizing agent during the reduction period **(Figure 1.2)**.

$$HAuCl_4^- + \text{Alkane-thiolate} \xrightarrow{\text{Reducing Agent}} Au$$
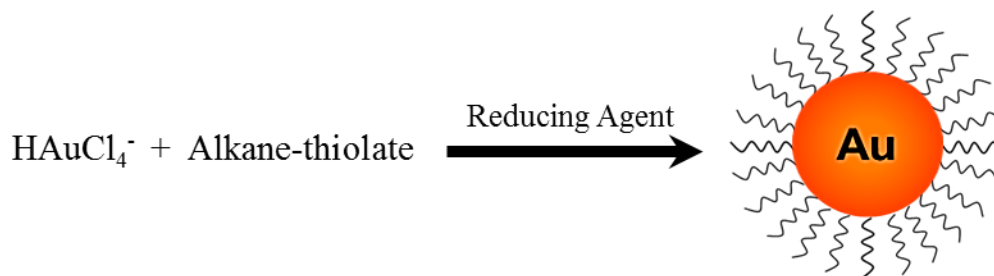
Figure 1.2: Illustration describing the reduction of Au^{3+} to Au^0 using a alkane-thiolate as a capping ligand under reducing conditions.

Since then, the Brust-Schiffrin method has been modified to yield monodisperse AuNPs depending on the size desired. Time-dependent additions of sodium borohydride ($NaBH_4$) or concentrations of alkane-thiolates yield AuNPs ranging from 1-6 nm.[22-26] For example, in an adaptation of the Brust-Schiffrin method, triphenylphosphine (PPh_3) is used to improve the synthesis of Schmid's cluster[27] [$Au_{55}(PPh_3)_{12}Cl_6$]. To a water-toluene mixture of $HAuCl_4^-$ and

$N(C_8H_{15})_4Br$, PPh_3, and $NaBH_4$ are added to synthesize the cluster $[Au_{101}(PPh_3)_{21}Cl_5]$ which has a diameter of ca. 1.5 nm.[23, 25]

More recently, the expansion of the field has led to novel approaches to gold synthetic methods. For example, the Perrault method uses hydroquinone to reduce $HAuCl_4^-$ in aqueous solutions giving monodispersed nanoparticles in a range of 50-200 nm.[28] Martin and Eah use varying ratios of $NaBH_4$-$NaOH$ to $HAuCl_4$-HCl to produce negatively charged "naked" nanoparticles that are stabilized in aqueous solutions by the ions that surround the cores.[29] Lastly, A. Sahasrabudhe has successfully used the polyoxometalate $(NH_4)_{42}[\{(Mo^{VI})Mo^{VI}_5O_{21}(H_2O)_6\}_{12}\{Mo^V_2O_4(CH_3COO)\}_{30}] \cdot 10\ CH_3COONH_4 \cdot 300\ H_2O$, Mo-132, as a reducing and stabilizing agent for the synthesis of AuNPs.[30]

1.2.3   Surface Plasmon Resonance

All AuNPs have a characteristic color in solution that ranges from a ruby red to violet. This unique nanoscale property is due to the size-dependent phenomena called surface plasmon resonance (SPR). Surface plasmon resonance is caused by the interaction between the electric field of visible light and the confined electron of a nanoparticle. The excitation of the electron located in the conduction band of a gold atom interacts with an electromagnetic wave causing a collective oscillation of the conductance electrons immediately above the Fermi level.[31]
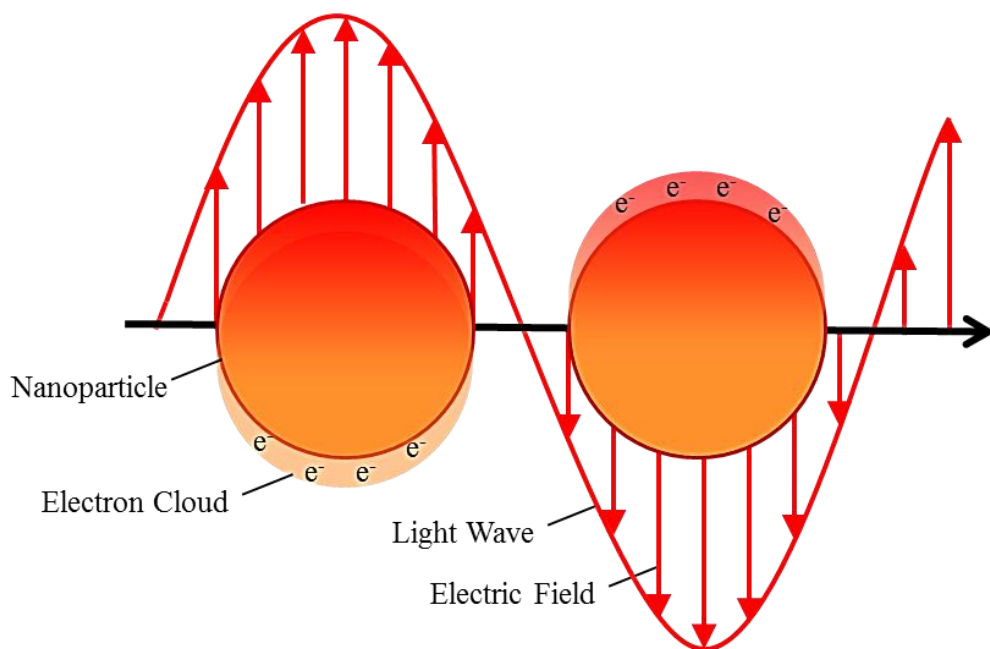
Figure 1.3: Illustration of the interaction between metal nanoparticles with a light wave to produce a collective oscillation called Surface Plasmon Resonance.

This oscillation of electrons displaces them relative to the nuclei which generates a resonant of less than or matching frequency of the incident light.[32-35] The term "surface" stems from the fact that although all electrons are oscillating with respect to positive-ion background, the main effect producing the restoring force is the surface polarization. Thus, the surface plays a critical role by altering the boundary condition for the polarizability of the metal and solution medium, therefore shifting the resonance to optical frequencies.[33]

The Mie theory[34], developed in 1907, first provided a method for calculating the SPR spectra by solving a set of Maxwell equations for spherical nanoparticles. This theory uses Maxwell's equations with the electronic and magnetic fields along with the spherical coordinates of the nanoparticle to give an approximation of the interaction of light with spherical

nanoparticles. Applied to UV-vis spectroscopy, the theory describes extinction coefficients of spherical nanoparticles of arbitrary sizes.[33]

For AuNPs, the surface plasmon resonance yields a characteristic UV-vis absorption between 500-600 nm which is dependent on the size and shape of the nanoparticle, as well as the dielectric properties of the medium.[34-37] Spherical nanoparticles with a diameter of ca. 10 nm have a surface plasmon resonance at approximately 520 nm.[16] As the diameter increases in size, a red-shift in the UV-vis spectra is observed due to a retardation effect of the electromagnetic field.[16,33] In contrast, smaller spherical nanoparticles (1.4-3.2 nm) show a decrease in intensity of the plasmon peak (~520 nm) with an complete absence of the peak below approximately 2.0 nm.[25, 33, 38] This is due to fewer electrons interacting at the Fermi level (quantum size effects).[33]
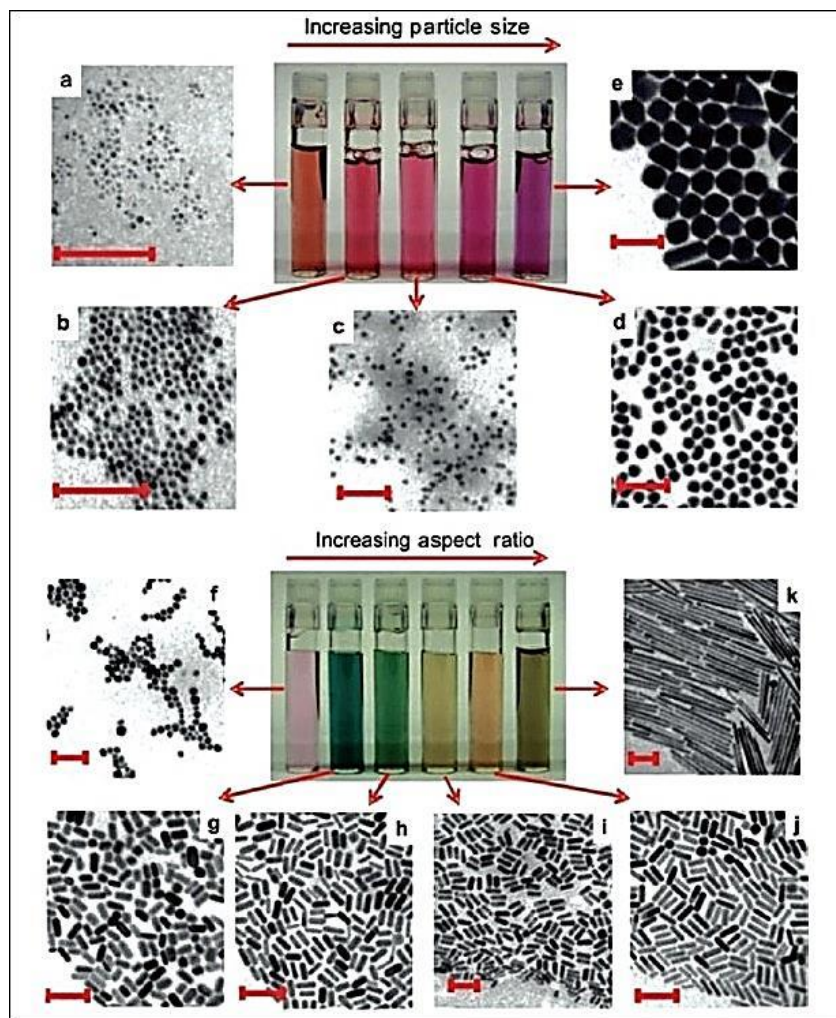
Figure 1.4: Photographs of aqueous solutions of gold nanospheres (upper panels) and gold nanorods (lower panels) as a function of increasing dimensions. Corresponding transmission electron microscopy images of the nanoparticles are shown (all scale bars 100 nm). Reproduced with permission from reference 16. Copyright © 2010 Journal of Pharmacy and Bioallied Sciences.

SPR plays an essential role in our studies by supporting the characterization of various gold core sizes. Gold core diameters of ca. 1.6 nm exhibited an absence of the SPR peak (~520 nm). A diameter of ca. 4.4 exhibited a SPR peak at ca. 520 nm, and the core diameter of ca. 8.6 nm exhibited a peak at ca. 530 nm. SPR also supported the extinction of individual Au nanoparticles that assembled with various polyoxomolybdate clusters. As the [POM]:[Au] ratio

increased, polyoxomolybdates acted as screening mechanisms to the Au cores. This, as well as

the formation of large aggregates, resulted in a disappearance of the SPR band.

1.3   Electrostatic Interactions of Spherical Systems

1.3.1   DLVO Theory

Nanoparticles in aqueous solutions show great potential for application to biomedical

fields and catalysis.[39-44] Therefore, depending on the nature of the application, nanoparticle

aggregation may need to be controlled or avoided.[45] Before any advances are able to occur,

surface interactions must be well understood. These surface interactions play a key role in

electrostatic assemblies. Taking a closer look at these interactions, one must take into account

the surface forces between the nanoparticle and the aqueous medium. Typically for aggregation,

surface charge on nanomaterials is approximately zero.   This allows for nanomaterials of

opposite charge to aggregate by offsetting the others' charge, thus, forming larger assemblies

which precipitate due to gravitational force.[46] On the other hand, when particles possess "like"

charges, they have a shared electrostatic repulsion that allows them to avoid aggregation and

remain in a stable solution.[47]

To further explain these interactions, one must take into account the classic DLVO theory

to determine the net electrostatic interactions of nanomaterials. DLVO theory, named after

Dejaguin, Landau, Verwey, and Overbeek, was developed to relate the stability of two particles

in suspension to their total potential energy.[47-49] The theory includes both Lifshitz-van der Waals

attraction forces and the repulsion of electrostatic forces.[50-52] Electrostatic repulsion arises due to

the overlapping electrical double layers of two particles, which contain same charge counter-ions

leading to this repulsive force. **(Fig. 1.5)**
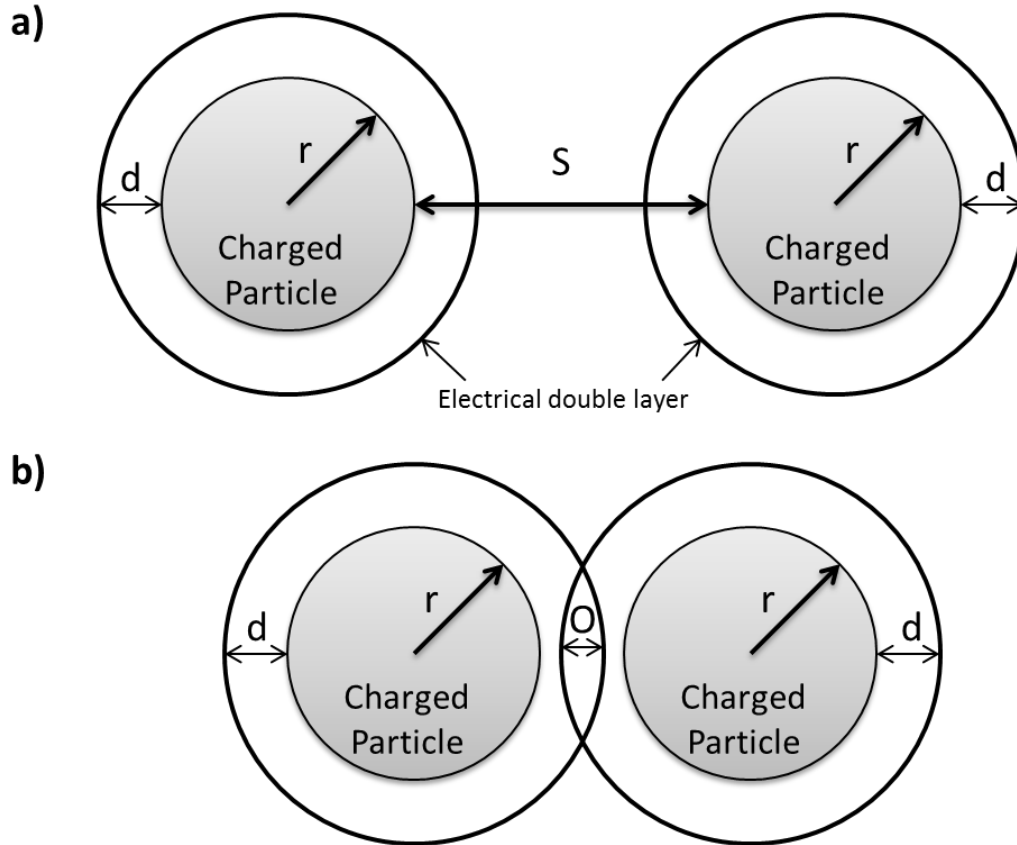
Figure 1.5: An illustration of the electrostatic interactions of two spherical particles. a) distance (S) between two particles, where S is greater than the distance between the electrical double layers of the particles. This results in no interactions between the two particles, thus no electrostatic repulsion. b) overlap (O) between two particles. This overlap increases the electrostatic repulsion between the two particles as the distance decreases.

The total potential energy relies on the internuclear distance between two particles. **(Fig. 1.6)**

Long range van der Waals attractions allow for two particles to approach each other. The double

layers of the approaching particles will begin to overlap leading to short range electrostatic

repulsion. The potential energy barrier arises as a consequence of the difference in magnitude of

electrostatic repulsion in comparison to van der Waals attraction forces. The particles will

agglomerate when attractive forces predominant; a stable suspension will occur if the repulsive

forces are stronger.[53-54] One must note, while the concept of attraction and repulsion seems

simple, the cumulative effects of all the charged entities in solution lead to a very complex and

usually difficult calculation.[55]
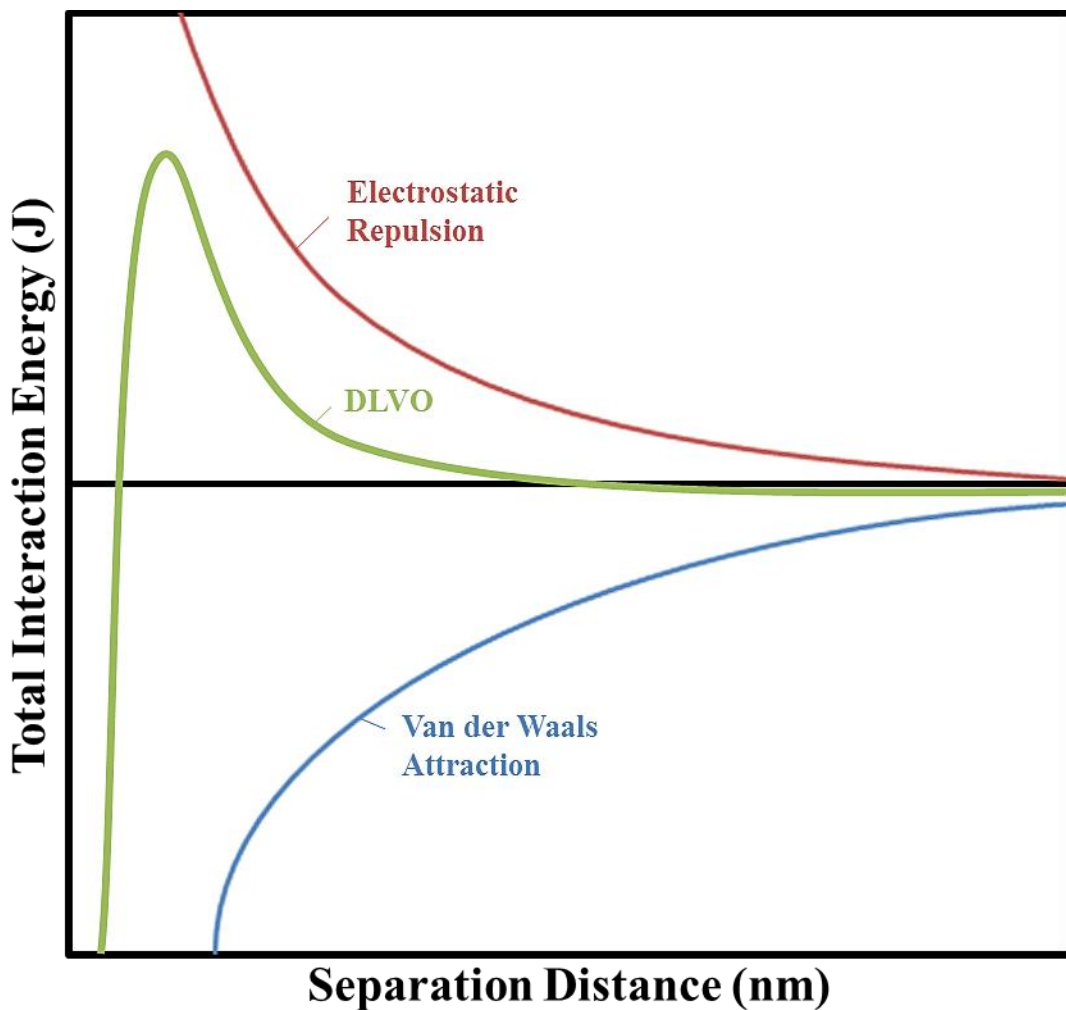
Figure 1.6: Dependence of Total Interaction Energy between two particles on internuclear
separation distance. This potential energy barrier arises as a consequence of the difference in
magnitude of repulsive forces in comparison with attractive electrostatic forces. When the

attractive forces are dominant, the particles will adhere; if the repulsive forces are stronger then the particles will remain suspended separately.

One model for the total interactions (V_{total}, Eq.1) between two spherical particles in solution calculates the van der Waals attraction (Eq. 2) and the electrostatic repulsion (Eq. 3) of spherical nanoparticles:[50, 51, 56]

$$V_{total} = V_{vdW} + V_{elec} \quad \text{Eq. 1}$$

$$V_{vdW} = -\frac{A}{6}\left[\frac{2a_1a_2}{R^2-(a_1+a_2)^2} + \frac{2a_1a_2}{R^2-(a_1-a_2)^2} + ln(\frac{R^2-(a_1+a_2)^2}{R^2-(a_1-a_2)^2})\right] \text{Eq. 2}$$

$$V_{elec} = 2\pi\varepsilon_r\varepsilon_0\psi_0^2 R k_B T \ln[1 + \exp(-kd)](\text{in the case of } kd > 5), \text{ Eq. 3}$$

$$\text{where } k = \left[\frac{1000e^2 N_A(2I)}{\varepsilon_r\varepsilon_0 k_B T}\right]^{1/2} \text{Eq. 4}$$

In these equations, A is a Hamaker constant, k_B is the Boltzmann constant, T is temperature, R is the radius of the particles, d is the separation distance between the particles, ε_r is a relative dielectric constant of the liquid, ε_0 is the permittivity of the vacuum, ψ_0 is the surface potential of the particles, k is the inverse Debye length, e is the elementary charge, N_A is Avogadro's number, and I is the ionic strength of the solution.

DLVO theory allows us to describe the electrostatic interactions between AuNPs and POMs. As the solution environment changes with an increase in [POM], the potential energy barrier is approached. This approach decreases the electrostatic repulsion forces that allow for a

13

stable suspension and increase the attractive forces until the attractive forces dominate the solution. This leads to the flocculation and sequentially precipitation of AuTMA+Mo-132 aggregates.

1.3.2   Zeta Potential (Double Layer) for Nanoparticles

There are many natural and man-made processes directed by electrostatic interactions due to nanoparticle surface charge. The properties that these materials possess at the solid/liquid interface are essential to the stability and aggregation of these systems.[57] Understanding these properties is fundamental to the design and characterization of these materials; such that analysis can assess the charge stability of a disperse system, and can aid in the formulation of colloidal stable products, e.g. liposomal formulations.[57-58]

At this time, technology does not have a satisfactory method to determine surface charge of particles in a polar liquid.[59]   Therefore, the analysis of the electric potential, termed zeta potential (ζ-potential), is observed at a distance from the particle surface at, what is known as, the slipping plane. The slipping plane is the interface located between the electrical double layer and the liquid solvent where the direct velocity measurements for particles moving in an applied electric field are measured.[60] To clarify, **Figure 1.7** illustrates the electrical potential layers surrounding a positive charged particle. The electrical double layer is comprised of a Stern layer and a diffuse layer. The Stern layer contains ions tightly bound to the particle surface. Beyond the Stern layer is the diffuse layer of loosely bound counter-ions and co-ions that freely flow about the liquid through the influences of thermal motion and electrical attraction.
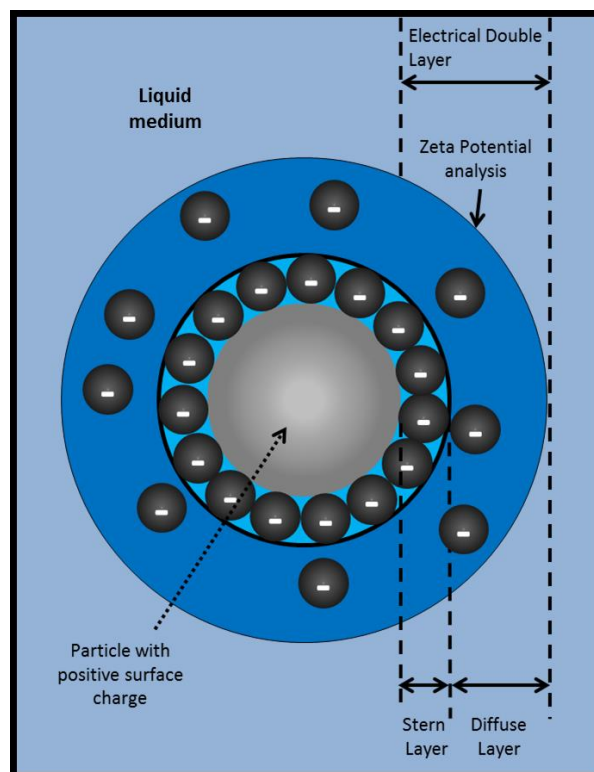
Figure 1.7: Illustration of the interface of zeta potential measurements. Together, the stern layer and diffuse layer form the electrical double layer. The boundary between the diffuse layer and the liquid medium, called the slipping plane, is where the zeta potential is observed.

Zeta potential is measured through electrophoretic light scattering experiments, in which, a laser beam is split into a reference and excitation beam. The excitation beam is directed through a sample while an applied voltage induces electrophoresis. The difference in frequency of the two beams is measured by the detector to provide the electrophoretic drift velocity.[61] These measurements are greatly affected by the environmental factors such as pH, ionic strength, and concentration.[62] Zeta potential values without these parameters are meaningless. For example, depending on protonation of carboxyl groups on mixed-thiol capped AuNPs, the zeta potential can range from 29 mV to -35 mV between pH values 3-11.[63]   The ionic strength determines the thickness of the double layer. At higher ionic strength, the double layer

compresses due to more charge repulsion from counter-ion components yielding a more stabilized environment.[64]

This analysis is vital to the study of electrostatic interactions between AuNPs and POMs because it assists in understanding how the specific nanoscopic entities play a role in the self-assembly of the aggregates formed. The interactions of positively charged AuTMA mediated with negatively charged POMs are predominately based on electrostatic interactions rendering zeta potential analysis an effective technique for these studies.

1.4   Polyoxometalates

In general, POMs can form a wide variety of structures.[65-71] Their chemically robust building units provide metal-organic frameworks through diverse structural chemistry.[72-82] This broad range of structural motifs exhibits interesting properties leading to developments in areas such as catalysis and photochemistry.[79, 83-86]

The array of POM dimensionalities includes isolated tetrahedral and octahedral moieties, several different polyanions including giant nanoscopic clusters, two-dimensional layers, and three-dimensional frameworks. Octahedral building units have played an important role in the development of large polyoxomolybdates. These octahedral moieties form systems of pentagons that come together to generate spherical structures. Various clusters have been synthesized to provide structures with numbers of molybdenum atoms that include Mo_{57},[87] Mo_{132},[88] Mo_{154},[89] Mo_{368},[90] etc.
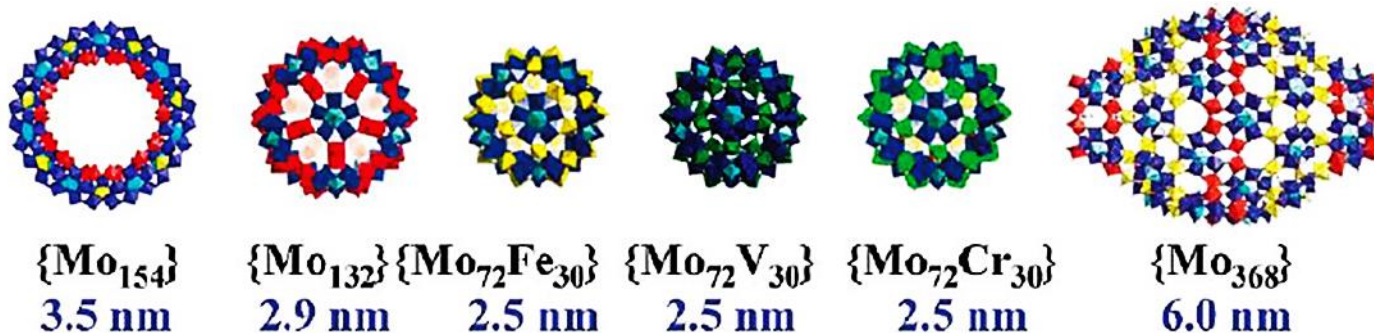
Figure 1.8: Some typical giant polyoxometalate molecular clusters and their sizes. For this work, {Mo_{154}} and {Mo_{132}} will be focused on.

1.4.1 Keplerates (Mo-132)

When Keplerates (Mo-132) were first discovered, they were considered quite remarkable due to their high symmetry and spherical shape which could be described as icosahedral inorganic superfullerenes.[88] The first crystallographically determined structure contained 132 molybdenum atoms with the formula
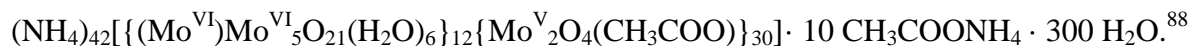
$(NH_4)_{42}[\{(Mo^{VI})Mo^{VI}_5O_{21}(H_2O)_6\}_{12}\{Mo^V_2O_4(CH_3COO)\}_{30}]\cdot 10\ CH_3COONH_4 \cdot 300\ H_2O.$[88] (Mo-132a)

The structure of Mo-132 exhibits a building unit of an 11 atom pentagonal moiety of molybdenum centers. The molybdenum substructure can be formulated as {Mo_{11}}$_{12}$, which describes the linking of twelve pentagonal units to create the sphere. The {Mo_{11}} motif exhibits of C_5 symmetry **(Fig. 1.9a)** and contains a central pentagonal bipyramidal MoO_7 unit with five edge-sharing MoO_6 octahedra, with an additional five corner-sharing MoO_6 octahedron.[88, 91-94] These pentagonal units are bridged by the corner-sharing MoO_6 octahedra to form {Mo_2O_4}$^{2+}$ linkers in reduced molybdate solutions that bring the twelve {$(Mo)Mo_5$} inner pentagons together to form the icosidodecahedral symmetry.[88] **(Fig. 1.9a)** This gives a formula of

17

$(NH_4)_n[\{(Mo^{VI})Mo^{VI}_5O_{21}(H_2O)_6\}_{12}\{Mo^V_2O_4(L^{n-})\}_{30}]^{(12+30n)-}$ in which the molybdate cage has an overall charge of -12, with 30 ligands (L^{n-}) bound to the $\{Mo_2O_4\}^{2+}$ linkers that face inward on the sphere.[95]
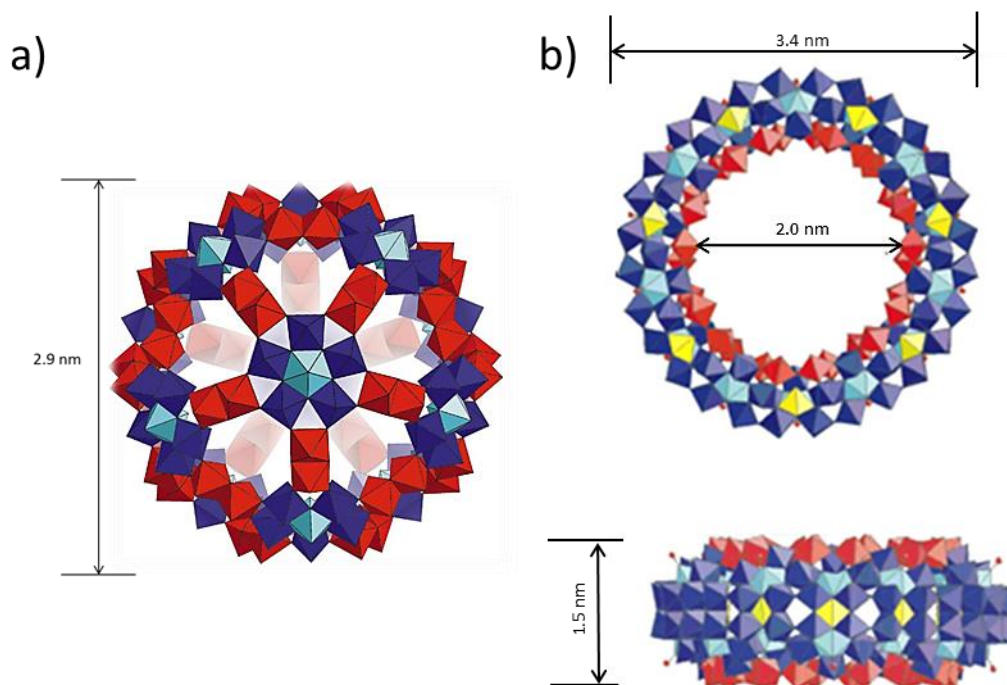
Figure 1.9: Polyhedra representations of the giant polyoxometalate anions (a) $[Mo^{VI}_{72}Mo^V_{60}O_{372}(CH_3COO)_{30}(H_2O)_{72}]^{-42}$ and (b) $[Mo_{154}(NO)_{14}O_{420}(OH)_{14}(H_2O)_{70}]^{-28}$ with the $\{Mo_{11}\}$ motif shown in dark gray.[88, 89]

Keplerates are synthesized using one-pot reactions, however, the synthesis requires specific optimal conditions to produce these large polyoxomolybdate structures. Starting with an acidic molybdenum solution containing Mo^{VI}, addition of a reducing agent yields Mo^V which forms the Mo_2 linkers. An abundance of these linking units is needed to form larger groups that can be linked in different ways. While slow evaporation of H_2O promotes the growth of crystals, this growth is limited due to the molybdenum-oxygen multiple bond (Mo=O) capping off the

cluster.[88] The "parent" cluster formed from this synthesis contains 30 CH_3COO^- groups giving a precise charge of -42 to the compound which is counter-balanced by 42 NH_4^+ ions.[95]

One fascinating thing about these clusters occurs at the reduced Mo^V linkers, the binuclear $\{Mo_2O_4\}^{2+}$ sites. At these reduced centers, the acetate ligand can be exchanged for a variety of ligands. Consequently, the acetate cluster is used as precursor to create various cluster derivatives through ligand exchange. Two Keplerates synthesized from this precursor are $(NH_4)_{72}[\{(Mo^{VI})Mo^{VI}_5O_{21}(H_2O)_6\}_{12}\{Mo^V_2O_4(SO_4)\}_{30}]$[96] (Mo-132b) and $(NH_4)_{72}[\{(Mo^{VI})Mo^{VI}_5O_{21}(H_2O)_6\}_{12}\{Mo^V_2O_4(HPO_4)\}_{30}]$.[97] (Mo-132c) Since CH_3COO^- is monovalent compared to both SO_4^{2-} and HPO_4^{2-} are divalent, the overall negative charge of compounds Mo-132b and Mo-132c increases from -42 in the acetate derivative to -72 which also increases the cation affinity of each structure.[94, 96-98]

1.4.2 "Big Wheel" cluster (Mo-154)

Along with the Mo-132 cluster, a ring-shaped cluster with the formula $(NH_4)_{28}[Mo_{154}(NO)_{14}O_{420}(OH)_{14}(H_2O)_{70}] \cdot 350\ H_2O$ (Mo-154 **Fig. 1.9b**) was first synthesized in 1995.[89] This structure comprised of 140 MoO_6 units and 14 pentagonal bipyramidal sites has been recognized as one of the main components in molybdenum blue.[98-99] The driving force for the isolation of this cluster is the symmetry of the cluster itself. For Mo-132, a strong reducing agent allows for all five bridging units of MoO_6 bound to the 12 pentagonal units to reduce to Mo^V units; yielding C_5 symmetry. However, for Mo-154 a weaker reducing agent only allows for partial reduction of the five bridging units yielding a mixed-valent (Mo^{VI}/Mo^V) diamagnetic compound.[88-89]

Since the $\{Mo_{11}\}_{14}$ motifs contain both Mo^V and Mo^{VI} centers, C_S symmetry **(Fig. 1.10b)** is present rather than C_5 symmetry **(Fig. 1.10a)** of Mo-132 and the overall structure can be described as a tetradecamer with D_{7d} symmetry.[100] The $\{Mo_{11}\}$ units may also be considered to be constructed from 14 $\{Mo_8\}$, $\{Mo_2\}$, and $\{Mo_1\}$ units.[88, 101-103] **(Fig. 1.10b)** To complete a $\{Mo_{11}\}$ unit, $\{Mo_8\}$ units are fused together through $\{Mo_2\}$units, thus completing the inner-ring portions of the both the upper and lower halves. Likewise, along the "equator" of the ring, $\{Mo_1\}$ units are fused to complete the ring system with the second half rotated by 360/14° relative to the first half.[88,104]
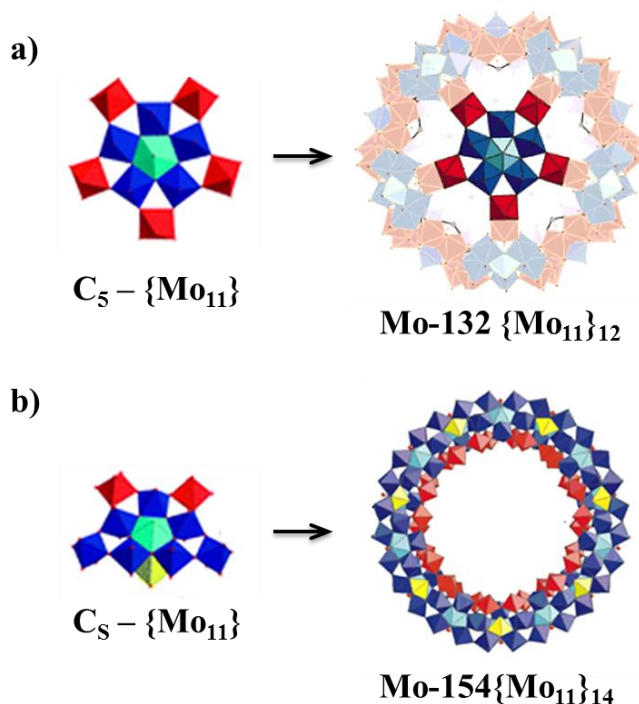
Figure 1.10: a) Polyhedral representation of the C_5 symmetry of the $\{Mo_{11}\}_{12}$ units. The light/dark blue polyhedral depict Mo^{VI}units with the Mo^V linker units in red. b) Polyhedral representation of the C_S symmetry of the $\{Mo_{11}\}_{14}$ units where $\{Mo_8\}$ clusters (light/dark blue) are fused by $\{Mo_2\}$units (red) with an equatorial$\{Mo_1\}$ unit (yellow).

These two classes of polyoxometalates may allow promising advancements in various applications such as catalysis, photochemistry, electrochemistry, self-assembly, and sensors.[105-109] One field of interest to us is the electrostatic self-assembly of novel metal nanoparticles. With the nanoscopic dimensions of $(NH_4)_n[\{(Mo^{VI})Mo^{VI}_5O_{21}(H_2O)_6\}_{12}\{Mo^V_2O_4(L^{n-})\}_{30}]^{(12+30n)-}$ and $[Mo_{154}(NO)_{14}O_{420}(OH)_{14}(H_2O)_{70}]^{-28}$ together with their precise negative charges make these compounds excellent candidates for investigating electrostatic self-assembly.

1.5   Self Assembly

Using these properties discussed in Section 1.1, scientists have been able to build frameworks and controlled aggregates that can provide advances in the medical, sensory, technological, and environmental fields. The strategy, known as self-assembly, provides two general approaches: 1) "top-down" and 2) "bottom-up".[110-112]

The "top-down" method forms nanoscale particles through the physical or chemical break down of bulk material, relying on various techniques used to cut, mill, and shape materials into desired shapes and order. These materials are deposited through various lithographic techniques such as, electron beam lithography, silicon photolithography, and inkjet printing into patterned materials. The "bottom-up" method employers techniques of molecular synthesis, colloidal chemistry, polymer chemistry, and other related fields using building blocks in the solid, liquid, or gas phase to fabricate nanoscale structures.[113]

The assembly of nanoparticles with controlled morphologies occurs when the building blocks interact with one another via weak covalent and non-covalent intermolecular forces such as van der Waals, electrostatic, hydrophobic, and hydrogen bonding interactions, in such a way that the interactions are controllable and reversible.[114] The determination of the type of

21

architecture formed in these assemblies relies on the flexibility and positioning of these interactions when aggregates form. For example, highly ordered crystalline structures form when nanoparticles have free range of motion about one another in the aggregate yielding thermodynamically favorable structures.

A great deal of work has been published using these techniques to provide a range of precedents from DNA,[115] proteins,[116] self-assembled monolayers (SAMs),[117] and metal nanoparticles.[118] For example, the Grzybowski[118] group has extensively studied the interactions of charged AuNPs and silver nanoparticles (AgNPs). They have discovered that cationic AgNPs will aggregate and subsequently precipitate from a solution only when their charge is compensated by anionic AuNPs **(Fig. 1.11)**.
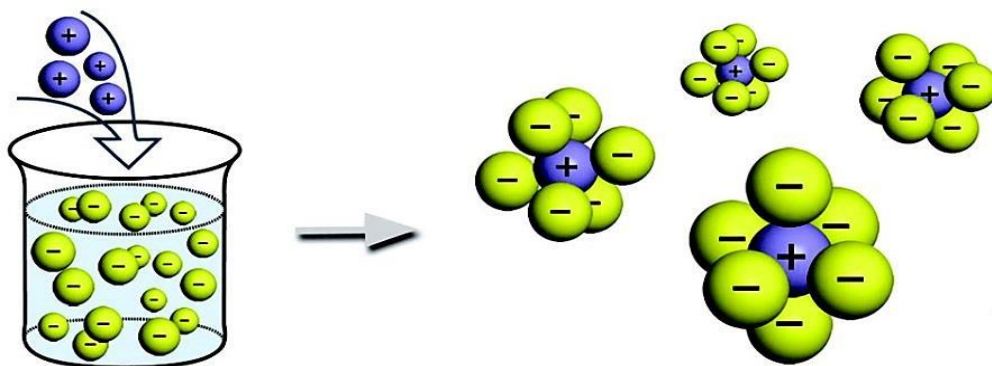
Figure 1.11: Illustration of N,N,N-trimethyl(11-mercaptoundecyl)ammomium chloride (TMA) capped silver nanoparticles (AgTMA) being combined with a mixture of 11-mercaptoundecanoic acid capped gold nanoparticles (AuMUA). Aggregation occurs upon charge balancing of the individual entities. Reprinted with permission from reference 118. Copyright 2006 American Chemical Society.

These findings have led our own group to explore the effects of charge balancing with with cationic AuNPs and a variety of POMs described in Section 1.4.

1.6 General Research Considerations

This work encompasses the detailed investigation of electrostatic interactions between spherical AuNPs and giant anionic POMs of Mo-132 and Mo-154. The stability, aggregation, and behavior of aqueous solutions containing variable concentration ratios of the two nanoscopic entities were examined. A number of determinants were revealed, including counter-ion screening, ionic strength, charge and shape of the POM, along with the AuNP size yielding a better understanding for the behavior and interaction between the two entities. This understanding will aid in the further work towards developing highly ordered structures; allowing for advances in applications that incorporate the plasmonic properties of AuNPs along with the redox and catalytic properties of these giant POMs.

1.7 References

[1]   S. Horikoshi, N. Serpone, *Nanotechnology: Microwaves in Nanoparticle Synthesis* 1st Ed. **2013**, Wiley-VCH.

[2]   Editorial, *Nature Nanotechnology* **2009**, 4, 203.

[3]   T. Appenzeller, R. Feynman, *Science.* **1991,** 254, 5036,1300-1301.

[4]   (a) J.A. Blackman; C. Binns; *Metallic Nanoparticles* **2009** Ed, Elsevier B.V. (b) P. W. Atkins et al., *Shriver & Atkins Inorganic Chemistry* 4th Ed. **2006**, Oxford Press.

[5]   S. Ghorai, PhD. Dissertation, University of Iowa, **2013**.

[6]   K.L. Kelly, E. Coronado, L.L. Zhao, G.C. Schatz, *J. Phys. Chem. B* **2003**, 107, 668-677.

[7]   J.A. Rogers, M.G. Lagally, R.G. Nuzzo, *Nature* **2011**, 477, 45-53.

[8]   T.K. Indira, P.K. Lakshmi, *International Journal of Pharmaceutical Sciences and Nanotechnology* **2010**, 3, 3 1035-1042.

[9]   C. Burda, X. Chen, R. Narayanan, M.A. El-Sayed, *Chem. Rev.* **2005**. 105, 1025-1102

[10]   C.B. Murray, *Nano Lett.* **2013**, 13, 4980-4988.

[11]   B. Bhushan, *Encyclopedia of Nanotechnology: Synthesis of Gold Nanoparticles*, Springer, **2012**.

[12]   D.J. Barber, I.C. Freestone, *Archaeometry* **1990**, 32, 33.

[13]   I. Borgia, B. Brunetti, I. Mariani, A. Sgamellotti, F. Cariati, P. Fermo, M. Mellini, C. Viti, G. Padeletti *Appl. Surf. Sci.* **2002**, 185, 206.

[14]   M. Faraday, *Phil. Trans. R. Soc.* London, 147, **1857**.

[15]   R.A. Zsimondy, Properties of Colloids, Nobel lecture, **1926**.

[16]   V.V. Mody, R. Siwale, A. Singh, H.R. Mody, Introduction to Metallic Nanoparticles. *J. Pharm. Bio. Sci.* **2010**, 2, 282-289.

[17]   D.A. Giljohann, D.S. Seferos, W.L. Daniel, M.D. Massich, P.C. Patel, C.A. Mirkin, *Angew. Chem. Int. Ed. Engl.* **2010,** 49, 19,3280-3294.

[18]   Y. Xia, Y. Xiong, B. Lim, S.E. Skrabalak, *Angew. Chem. Int. Ed.* **2009**, 48, 1, 60–103.

[19]   M.R.K. Ali, B. Snyder, M.A. El-Sayed, *Langmuir* **2012**, 28, 25, 9807–9815.

[20]   J. Turkevich, P. C. Stevenson, J. Hillier, *Faraday. Soc.* **1951**, 11, 55–75.

[21]   G. Frens, *Nature: Phys. Sci.* **1973**, *241*, 20-22.

[22]   M.C. Daniel, D. Astruc, *Chem. Rev.* **2004**, 104, 293-346.

[23]   M. Brust, M. Walker, D. Bethell, D.J. Schiffrin, R. Whyman, *Chem. Comm.* **1994**, 7, 801-802.

[24]   M. M. Maye, S. I-Im, J. Lim, Z. Luo, D. Rab, T. Rabinovich, C.-J. Liu, J. Zhong, *J. Am. Chem. Soc.* **2005**, 127, 1519-1529.

[25]   W.W. Weare, S.M. Reed, M.G. Warner, J.E. Hutchison, *J. Am. Chem. Soc.* **2000**, 122,12890-12891.

[26]   M. J. Hostetler, J.E. Wingate, C. J. Zhong, J.E. Harris, R.W. Vachet, M.R. Clark, J.D. Londono, S.J. Green, J.J. Stokes, G.D. Wignale, G.L. Glish, M.D. Porter, N.D. Evans, R. W. Murray, *Langmuir* **1998**, 14, 17.

[27]   G. Schmid, et. al. *Chem. Ber.* **1981**, 114, 3634–3642.

[28]   S.D. Perrault, W.C.W. Chan, *J. Am. Chem. Soc.* **2009**, 131, 47.

[29]   M.N. Martin, J.I. Basham, P. Chando, S.-K. Eah, *Langmuir* **2010**, 26, 10, 7410–7417.

[30]   A. Sahasrabudhe, S. Roy, *J. Mol. Eng. Mater.* **2014**, 02, 1440002.

[31]   K.J. Klabunde, R.M. Richards, *Nanoscale Materials in Chemistry*. 2nd Ed., **2009**, Wiley-VCH.

[32]   J.L. Hammond, N. Bhalla, S.D. Rafiee, P. Estrela *Biosensors* **2014**, *4*, 172-188.

[33]   S.K. Ghosh, T. Pal, *Chem. Rev.* **2007**, 107, 4797-4862.

[34]   G. Mie; *Annalen der Physik* **1908**, 330, 3, 377–445.

[35]   G. Schmid, B. Corain, *Eur. J. Inorg. Chem.* **2003**, 3081-3098.

[36]   P.L. Jain, K.S. Lee, I.H. El-Sayed, M.A. El-Sayed, *J. Phys. Chem. B* **2006**, 110, 7238-7248.

[37]   S.L. Logunov, T.S. Ahmadi, M.A. El-Sayed, J.T. Khoury, R.L. Whetten, *J. Phys. Chem. B* **1997**, *101*, 3713-3719.

[38]   M. M. Maye, W. X. Zheng, F. L. Leibowitz, N. K. Ly, C. J. Zhong, *Langmuir* **2000**, 16, 490-497.

[39]   P. Hervés, M. Pérez-Lorenzo, L. Liz-Marzán, J. Dzubiella, Y. Lu, M. Ballauff, *Chem. Soc. Rev.*, **2012**, 41, 5577–5587.

[40]   C. Fang, N. Bhattarai, C. Sun, M. Zhang, *Small* **2009**, 14, 1637-1641.

[41]   C. Blanco-Andujar, L.D. Tung, N.T.K. Thanh, *Annu. Rep. Prog. Chem., Sect. A* **2010**, 106, 553–568.

[42]   S.C. Tsang, C.H. Yu, X. Gao, K. Tam, *J.Phys. Chem. B* **2006**, 110, 16914.

[43]   S.I. Stoeva, F.W. Huo, J.S. Lee, C.A. Mirkin, *J. Am. Chem. Soc.* **2005**, 127, 15362-15363.

[44]   N.L. Rosi, C.A. Mirkin, *Chem. Rev.* **2005**, 105, 1547-1562.

[45]   B. Dubertret, P. Skourides, D.J. Norris, V. Noireaux, A.H. Brivanlou, A. Libchaber, *Science.* **2002**, 298, 1759-1762.

[46]   J.A. Blackman, C. Binns, *Metallic Nanoparticles.* **2009**, Elsevier B.V.

[47]   E.J. Verwey, J.T. Overbeek, *Theory of the Stability of Lyophilic Colloids,* 1st Ed. Amsterdam, **1948**, Elsevier.

[48]   B. Deryagin, L. Landau, *Acta Physicochimica URSS* **1941**, 14, 633-62.

[49]   T. Ndikubwimana, X. Zeng, N. He, Z. Xiao, Y. Xie, J-S. Chang, L. Lin, Y. Lu, *Biochemical Engineering Journal* **2015**. doi:10.1016/j.bej.2015.05.010

[50]   K. Lee, A.N. Sathyagal, A.V. McCormick, *Colliods and Surfaces A Physicochemical and Engineering Aspects*, **1998**, 144, 115-125.

[51]   R.J. Hunter, *Foundations of Colloid Science*. 2nd Ed. Oxford, **2001**, Oxford University Press.

[52]   P.K. Sharma,K.H. Rao, *Colloids and Surfaces B Biointerfaces.* **2009**, 29, 21-38.

[53]   P.C. Hiemenz, *Principles of Colloid and Surface Chemistry*, New York, **1986**, Marcel Dekker

[54]   D.H. Everett, *Basic Principles of Colloid Science*, London, **1988**, RSC Publications.

[55]   J.N. Israelachvili, *Intermolecular and Surface Forces.* Revised: 3rd Ed. **2011**. Academic Press.

[56]   T. Doane, C. Burda, *Advanced Drug Delivery Reviews*. **2013**, 65, 607-621.

[57]   M. Zembala, *Advances in Colloid and Interface Science* **2004**, 112, 59-92.

[58]   Coriolis-Pharma, *Zeta Potential* http://www.coriolis-pharma.com/contract-analytical-services/zeta-potential Accessed: December 14, 2014.

[59]   R. Xu, *Particuology* **2008**, 6, 112–115.

[60]   R. Hidalgo-Alvarez, A. Martin, A. Fernández, D. Bastos, F. Martínez, F.J. de las Nieves *Advances in Colloid and Interface Science* **1996**, 67, 1-118.

[61]   T.L. Doane, C-H. Chuang, R.J. Hill, C. Burda, *Accounts of Chemical Research*. **2012,** 45, 3, 317-326.

[62]   A.M. El-Badawy, T.P. Luxton, R.G. Silva, K.G. Scheckel, M.T. Suidan, T.M. Tolaymat, *Environ. Sci. Technol.* **2010**, 44, 1260–1266.

[63]   P.P. Pillai, S. Huda, B. Kowalczyk, B.A. Grzybowski, *J. Am. Chem. Soc*. **2013**, 135, 6392−6395.

[64]   *Zetasizer Nano Application Note* MRK654-01, www.malvern.com.

[65]   A. Müller, F. Peters, M.T. Pope, D. Gatteschi, *Chem. Rev.* **1998,** 98, 239-272.

[66]   P.A. Lorenzo-Luis, P. Gili, Recent Research *Developments in Inorganic Chemistry* **2000**, 2, 185-196.

[67]   J.M. Clemente-Juan, E. Coronado, A. Gaita-Arino, *World Scientific Series in Nanoscience and Nanotechnology,* **2013,** 8, 155-171.

[68]   N.G. Armatas, E. Burkholder, J. Zubieta, *Journal of Solid State Chemistry* **2005**, 178(8), 2430-2435.

[69]   S. Jones, A. Aldous, E. Burkholder, J. Zubieta, *Polyhedron*, **2013,** 52, 582-590.

[70]   K. Darling, K. T. Smith, J. Vargas, C.J. O'Connor, J. Zubieta, *Inorg. Chem. Comm*. **2013,** 32, 1-4.

[71]   K. Wassermann, M.T. Pope, *Inorg. Chem.* **2001**, 40, 2763-2768.

[72]   Y. Xu, *Curr. Opin. Solid State Mater. Sci.* **1999**, 4, 133.

[73]   A. Clearfield, *Prog. Cryst. Growth Charact. Mater.* **1991**, 21, 1.

[74]   *Perspectives in the Solid State Coordination Chemistry of the Molybdenum Oxides,* M. T. Pope, A. Müller, eds., Netherlands, **2001**, Kluwer Academic Publishers, The Dordrecht.

[75]   R. S. Rarig, P. Hagrman, J. Zubieta, *Solid State Sci.* **2002**, 4, 77.

[76]   M. T. Pope, *Heteropoly and Isopoly Oxometalates*, New York, **1983**, Springer.

[77]   Special thematic issue on polyoxometalates: C. L. Hill, ed., *Chem. Rev.* **1998**, 98, 1.

[78]   *Polyoxometalate Chemistry: From Topology Via Self-Assembly to Applications*, M. T. Pope, A. Müller, eds., Netherlands, **2001**, Kluwer Academic Publishers, The Dordrecht.

[79]   *Polyoxometalates: From Platonic Solids to Anti-Retroviral Activity*, M. T. Pope, A. Müller, eds., Netherlands, **1994**, Kluwer Academic Publishers, The Dordrecht.

[80]   J. P. Jolivet, *Metal Oxide Chemistry and Synthesis: From Solution to Solid State*, New York, **2000**, John Wiley.

[81]   D. E. Katsoulis, *Chem. Rev.* **1998**, 98, 359.

[82]   K. Pavani, S. E. Lofland, K. V. Ramanujachary, A. Ramanan, *Eur. J. Inorg. Chem.* **2007**, 568.

[83]   A. Baiker, P. Dollenmeier, A. J. Reller, *Catal.* **1987**, 103, 394.

[84]   T. Ressler, J. Wienold, R. E. J. Jentoft, *Catal.* **2002**, 210, 67.

[85]   T. Yamase, J. Chem. Soc., *Dalton Trans.* **1985**, 2585.

[86]   T. Yamase, M. T. Pope, *Polyoxometalate Chemistry for Nanocomposites Design*, Netherlands, **2002**, Kluwer Academic Publishers, The Dordrecht.

[87]   F. Caruso, D.G. Kurth, D. Volkmer, M.J. Koop, A. Müller, *Langmuir*, **1998,** 14, 3462-3465.

[88]   A. Müller, P. Kögerler, H. Bögge, *Structure and Bonding.* **2000**, *96*, 203-236.

[89]   A. Müller, E. Krickemeyer, J. Meyer, H. Bögge, F. Peters, W. Plass, E. Diemann, S. Dillinger, F. Nonnenbruch, M. Randerath, C. Menke, *Angew. Chem. Int. Ed. Engl.* **1995***, 34*, 2122-2124.

[90]   A. Müller, E. Beckmann, H. Bogge, M. Schmidtmann, A. Dress, *Angew. Chem. Int. Ed.* **2002,** 41, 7, 1162-1167.

[91]   L. Cronin, E. Diemann, A. Müller, *Inorganic Experiments;* J.D.Woollins Ed. Weinheim, **2003,** 340-346, Wiley-VCH

[92]   A. Müller, E. Krickemeyer, H. Bögge, M. Schmidtmann, F. Peters, *Angew. Chem. Int. Ed.* **1998***, 37*, 3359-3363.

[93]   A. Müller, P. Kögerler, A.W.M. Dress, *Coord. Chem. Rev.* **2001***, 222*, 193-218.

[94]   A. Müller, S. Polarz, S.K. Das, E. Krickemeyer, H. Bögge, M. Schmidtmann, B. Hauptfleisch, *Angew. Chem. Int. Ed.* **1999***, 38*, 3241-3245.

[95]   A. Müller, S.K. Das, E. Krickemeyer, C. Kuhlmann, M. Sadakane, M.H. Dickman, M.T. Pope, *Inorganic Synthesis.* **2004**, *34*, 191-200.

28

[96]   A. Müller, Y. Zhou, H. Bögge, M. Schmidtmann, T. Mitra, E.T.K. Haupt, A. Berkle, *Angewandte Chemie.* **2006**, *118*, 474-479.

[97]   A. Müller, S.K. Das, S. Talismanova, R. Soumyajit, K. Beckmann, H. Bögge, *Angewandte Chemie International Edition.* **2003**, *42*, 5039-5044.

[98]   A. Müller, E. Krickemeyer, H. Bögge, M. Schmidtmann, B. Botar, M.O. Talismanova, *Angew. Chem. Int. Ed.* **2003***, 42*, 2085-2090.

[99]   A. Müller, C. Serain, *Acc. Chem. Res.* **2000***, 33*, 2-10.

[100]   A. Müller, D. Fenske, P. Kögerler, *Curr. Opin. Solid State Mater. Sci.* **1999***, 4*, 141-153.

[101]   A. Müller, F. Peters, M.T. Pope, D. Gatteschi, *Chem. Rev.* **1998***, 98*, 239-272.

[102]   L. Cronin, C. Beugholt, A. Müller, *J. Mol. Struct. : THEOCHEM* **2000***, 500*, 181-193.

[103]   A. Müller, E. Krickemeyer, H. Bögge, M. Schmidtmann, C. Beugholt, S.K. Das, F. Peters, *Chem. - Eur. J.* **1999***, 5*, 1496-1502.

[104]   A. Müller, S.K. Das, P.F. Vladimir, E. Krickemeyer, C. Beugholt, H. Bögge, M. Schmidtmann, B.Z. Hauptfleisch, *Anorg. Allg. Chem.* **1999**, 625, 1187-1192.

[105]   A. Müller, P. Gouzerh, *Chem. Soc. Rev.* **2012,** 41, 7431-7463.

[106]   Y. Zhou, L. Qin, C. Yu, T. Xiong, L. Zhang, W. Ahmad, H. Han, *RSC Adv*., **2014**, 4, 54928–54935.

[107]   A. Nakhaei, A. Davoodnia, *Chinese Journal of Catalysis* **2014,** 35, 1761–1767.

[108]   D. Fan, J. Hao, *Journal of Colloid and Interface Science* **2009,** 333, 757–763.

[109]   H. Li, Y. Yang, Y. Wang, C. Wang, W. Li, L. Wu, *Soft Matter*, **2011,** 7, 2668-2673.

[110]   C.M. Lieber, *MRS Bull.* **2003,** 28, 486-491.

[111]   S.W. Hecht, *Angew. Chem., Int. Ed. Engl.* **2003,** 42, 24-26.

[112]   G.M. Whitesides, B.A. Grzybowski, *Science*. **2002,** 295, 2418-2421.

[113]   G.M. Whitesides, J.K. Kriebel, B.T. Mayers, *Self-assembly and nanostructured materials. In Nanoscale Assembly;* W.T.S. Huck, Ed.;: New York, 2005; pp 217- 239, Springer.

[114]   M. Grzelczak, J. Vermant, E.M. Furst, L.M. Liz-Marzan, *ACS Nano* **2010,** 4, 3591.

[115]   K.L. Hamner, C.M. Alexander, K. Coopersmith, D. Reishofer, C. Provenza, M.M. Maye, *ACS Nano* **2013,** 7, 7011-7020.

[116]   S.K. Lee, M.M. Maye, Y-B. Zhang, O. Gang, D. van der Lelie, *Langmuir* **2009,** 25, 657-660.

[117] T. Zaba, A. Noworolska, C.M. Bowers, B. Breiten, G.M. Whitesides, P. Cyganik, *J. Am. Chem. Soc.*, **2014,** 136, 34, 11918–11921.

[118] A.M. Kalsin, B. Kowalczyk, S.K. Smoukov, R. Klajn, B.A. Grzybowski, *J. Am. Chem. Soc.* **2006,** 15046–15047.

Chapter 2

Keplerate Cluster (Mo-132) Mediated Electrostatic Assembly of Gold Nanoparticles

2.1   Introduction

The organization of matter across length scales exploiting well-defined building-blocks is a fundamental strategy in the rational design of advanced functional devices and materials. This strategy can be used in polyoxometalate chemistry[1-6], as well as in the specific case of nanoparticle assembly. The focus of research has recently turned toward the preparation and characterization of architectures composed of nanoscopic components[7,8]. Most approaches to nanoparticle assembly have relied on dispersion forces, molecular interactions or differences in particle sizes. On the other hand, electrostatic attraction has received attention only in recent years and remains somewhat less developed in this context[9-13].

Electrostatic attraction between charged entities in solution and the properties of their binary aggregates are dictated by their size regime. For example, a solution of oppositely charged metal nanoparticles shows remarkable stability and does not precipitate until the point of overall electroneutrality is attained[14]. Based on charge considerations alone, microparticles should also only precipitate only when charges are fully compensated; however, they are unstable due to residual van der Waals forces and precipitate continuously[15]. Whether such charge balancing in a binary mixture of proteins, polyelectrolytes, functionalized carbon nanotubes or other charged nanoscopic entities with nanoparticles[6,7,12-18] or microparticles[11] leads to similar properties remains relatively unexplored[19]. Specifically, the electrostatic assembly between charged nanoparticles (NPs) with narrow charge and morphology characteristics has recently led to a number of structures. For example, the electrostatic assembly of gold nanoparticles (AuNPs) has resulted in superlattices with diamond-like organization[12], novel plasmonic signatures[13], and hybrid superlattices[17]. In addition, positively charged NPs have proven particularly useful for the binding of biomacromolecules, such as DNA and proteins[6,16].

32

In terms of this broader science, supramolecular materials based on oppositely charged nanoparticles have been described, such as the formation of supercrystalline $NaZn_3$ lattices from PbSe and γ-Fe_2O_3 nanocrystals where specific size ratios directs assembly into superlattices with tunable optical and magnetic properties[20]. Self-assembly of nanocrystals of different size and functionality has also been shown to provide ordered binary superlattices. Tailoring particle size and deposition conditions provides arrays isostructural with NaCl, CuAu, $MgZn_2$, etc., demonstrating the parallels between nanoparticle assembly and atomic scale crystal growth[21-23].

Polyoxometalates (POMs)[24-31] form another particularly attractive class of charged, nano-building blocks due to their wide range of structures, topologies and physicochemical properties. Furthermore, because of their sizes, structures and properties, POMs are considered as intermediates between small molecules and metal oxide solids. Of particular interest in this respect are the nanoscaled polyoxomolybdates of the $\{Mo_{11}\}_n$ class, of which the spherically-shaped (n = 12) or wheel-shaped (n = 14) anions, such as $[Mo_{132}O_{372}(CH_3CO_2)_{30}(H_2O)_{72}]^{42-}$, $[Mo_{132}O_{372}(SO_4)_{30}(H_2O)_{72}]^{72-}$, and $[Mo_{154}O_{462}H_{14}(H_2O)_{54}(H_2PO_2)_7]^{21-}$, respectively, as well as the related bimetallic clusters of the type $Mo_{72}M'_{30}$ of which $[\{Na(H_2O)_{12}\}\subset \{Mo_{72}Cr_{30}O_{282}(CH_3CO_2)_{19}(H_2O)_{94}\}]$ and $[Mo_{72}Fe_{30}O_{252}(CH_3CO_2)_{12}\{Mo_2O_7(H_2O)\}_2 \{H_2Mo_2O_8(H_2O)\}(H_2O)_{91}]$ are representative (the two latter are also of interest for magnetism and geochemical aspects)[32-38]. The different spherical porous Mo_{132} nanocapsules of the type $\{(pentagon)_{12}(linker)_{30}\}$ allow the investigation of a variety of processes in solution under confined conditions, for example, because they possess stepwise closable pores and tunable internal functionalities, and exhibit the ability to tune the hydrophobicity of their interiors to influence properties such as encapsulated water structures, as well as allowing the investigation of cation transport/separation in small spaces[3].

The compound $(NH_4)_{42}[Mo_{132}O_{372}(CH_3CO_2)_{30}(H_2O)_{72}]\cdot$hydrate (Mo-132a) is a strong electrolyte that completely dissociates in aqueous solution to give a nanoscopic cluster with a diameter of 2.9 nm and a quantized 42 negative charge per cluster[39]. Although surface cations can enter the cavity, these are not considered in the case of these highly charged capsules[3]. Mo-132a has shown, as have the other corresponding Keplerates, unique solution properties uncommon for other electrolytes[3], such as self-assembly in less polar solvents into "blackberry-type" supramolecular structures[40-43]. It can also be encapsulated with cationic surfactants to modify its surface properties and charge[44]. The electrostatic assembly of Mo-132a with cationic terminated poly(styrene) to give polyoxometalate-based supramolecular star polymers which can further assemble into vesicular aggregates has been recently reported[45]. Furthermore, controllable interactions of quaternary-ammonium-terminated polystyrene-polyoxometalate composite micelles with Mo-132a-based supramolecular star polymers exhibit behaviors from self-recognition to supramolecular recognition[46].

Although Mo-132a is subject to some variations in charge due to coordination of acetates at the pentagonal units, in addition to the linker sites or to release of some internal acetates depending on concentration and pH[47,48], we explored its use as a novel anionic mediator in the electrostatic self-assembly of AuNPs functionalized with positively charged self-assembled monolayers (SAMs), based on the generally precise number of charges and the nanoscale dimensions. Because of its generally monodisperse core with quantized charge and well-defined shape, we postulated that Mo-132a mediated assembly of AuNPs would lead to a sharp precipitation of the nanosystems at the point of overall electroneutrality, i. e., the equivalence point. Moreover, this scenario may lead to the use of Mo-132a as an analytical probe for the

precise determination of charges on other nanoscopic species within the limitations of the afore-mentioned charge variations.

In this study, Au nanoparticles of 4.4 nm diameter were functionalized with the self-assembled monolayer (SAM) of N,N,N-trimethyl(11-mercaptoundecyl)ammonium chloride (TMA), to render the surface positively charged. Au nanoparticles were also coated with a monolayer of 11-mercaptoundecanoic acid (MUA) to obtain negatively charged particle controls. The electrostatic assembly between the Mo-132a clusters and the AuTMA resulted in tailored aggregation that depended on the [Mo-132a]:[AuTMA] stoichiometry, and thus on the electrostatic screening. The assemblies were studied by dynamic light scattering (DLS), zeta-potential analysis (ζ-Pot), and absorption spectroscopy (UV-vis) of the AuTMA surface plasmon resonance band (SPR).

2.2   Experimental

All chemicals were used as obtained without further purification. Acetic acid, sulfuric acid, hydrochloric acid, ammonium acetate, sodium chloride, and sodium acetate, were all purchased from Fisher. Hydrazine sulfate, ammonium chloride, ethanol, diethyl Ether, and were all purchased from Sigma-Aldrich. Ammonium molybdate was purchased from Alfa Aesar. Ammonium hydroxide was purchased from J.T. Baker. Ammonium sulfate was purchased from VWR. The pH of the solutions were measured using pHydrion vivid 1-11® pH paper. Water was distilled above 3.0MΩ in-house using a Barnstead Model 525 Biopure Distilled Water Center.

2.2.1 Synthesis of $(NH_4)_{42}[\{(Mo^{VI})Mo^{VI}_5O_{21}(H_2O)_6\}_{12}\{Mo^V_2O_4(CH_3COO)\}_{30}]\cdot$ $\approx 300\ H_2O \cdot \approx 10\ CH_3COONH_4$ (Mo-132a)

Prepared according to the literature[50-54]:

Briefly, ammonium molybdate (5.610g, 4.534 mmol), ammonium acetate (12.495g, 162.14 mmol), hydrazine (0.799 g, 60.92 mmol) were added to a 250mL aqueous solution which was stirred for $\approx$ 10 minutes. Acetic acid (83 mL, 50%($^v/_v$)) was added after 10 minutes and stirred until the solution turned from blue to green. The solution was then left on the bench top at 20˚C for 5 days during which a slow color change to dark brown occurred. After 5 days the formed crystals were filtered off using a glass frit filter, were washed with ethanol and diethyl ether and dried in air. Yield 2.766g (39% based on Mo)

2.2.2 Synthesis of $(NH_4)_{72}[\{(Mo^{VI})Mo^{VI}_5O_{21}(H_2O)_6\}_{12}\{Mo^V_2O_4(SO_4)\}_{30}] \cdot \approx 200\ H_2O$ (Mo-132b)

Prepared according to the literature[53]:

Briefly, $(NH_4)_{42}[\{(Mo^{VI})Mo^{VI}_5O_{21}(H_2O)_6\}_{12}\{Mo^V_2O_4(CH_3COO)\}_{30}] \cdot \approx 300\ H_2O \cdot \approx 10$ CH_3COONH_4 (1.998 g, 0.07 mmol) and ammonium sulfate (8.010 g, 60.58 mmol) were added to 160 mL of water in a 400 mL Erlenmeyer flask. Sulfuric acid (21 mL, 2M) was then added with stirring. After approximately 5 min, the solution was placed on the bench top at 20˚C for two weeks, after which the precipitated brown crystals were filtered using a glass frit filter. Approximately 20 mL of isopropyl alcohol was used to wash the crystals followed by 5 mL of diethyl ether and dried in air. Yield: 1.582 g (76% based on Mo)

2.2.3   Synthesis of TOAB-, TMA-, and MUA-capped gold nanoparticles (AuTOAB).

N,N,N-trimethyl(11-mercaptoundecyl)ammonium chloride (TMA) and sodium 11-mercaptoundecanoic acid (MUA) were synthesized following procedures reported recently[55,56]. In a typical synthesis, tetra-n-octylammonium bromide (TOAB) protected gold nanoparticles (AuTOAB) were prepared[57]. Briefly, TOAB (0.553 g, 1.1 mmol) was dissolved in a solution of toluene (32 mL) with stirring. $HAuCl_4$ (0.0782 g, 1.9 mmol) was dissolved in H_2O (20 mL), allowed to stand for 15 min, and added to the toluene solution with stirring in which TOAB induced phase transfer. After continuing to stir for an additional 30 min, the toluene and aqueous layers were separated. The toluene layer was then transferred to a 100 mL round bottom flask, and a solution of $NaBH_4$ (0.036 g, 0.95 mmol, in excess) in H_2O (20 mL) was added dropwise, whereupon the solution changed from a red-orange to a dark red color, indicating the formation of TOAB-capped Au ($d = 4.4 \pm 0.7$ nm). To prepare TMA-capped Au, TMA (2.6 mg, 0.009 mmol) was first dissolved in 2 mL of ethanol. An aliquot of this TMA solution (0.05 ml) was added to 2 mL of AuTOAB. A black precipitate appeared immediately and was allowed to settle. After decanting the supernatant, excess TMA was removed by washing the precipitate with ethyl acetate (1.0 mL). The precipitate was decanted and dissolved in H_2O (2 mL) by sonication. To prepare the MUA-capped particles AuMUA, MUA (2.7 mg, 0.012 mmol) was dissolved in 2 mL of ethanol. A 0.5 mL aliquot of this MUA solution was added to 2 mL of AuTOAB. After precipitation, excess MUA was removed as above. The final AuTMA concentrations were ~600 nM, and were calculated using the known extinction coefficient of the AuTOAB particles[58].

The formulations of the nanoparticles were estimated according to a modified version of the method of Stoeva and coworkers[56] as applied by Grzybowski and coworkers[13]. For particles

of average diameter 4.4 nm, determined using TEM **(Figure 1(a) and (b))**, the approximate

composition is $Au_{3100}TMA_{760}Cl_{760}$. XPS analysis with an incident photon energy of 100 eV of

$Au_{3100}TMA_{760}Cl_{760}$ gave At% of ca. 68.8, 15.8 and 15.4 for Au, S and Cl, respectively

(calculated: Au, 67.1; S, 16.5; Cl, 16.5). This composition is also consistent with the TGA

profile which shows a total weight loss of 30.4% in the 175 to 550 °C range **(Figure 2.1)**

compared to a theoretical weight loss of 25.9%.
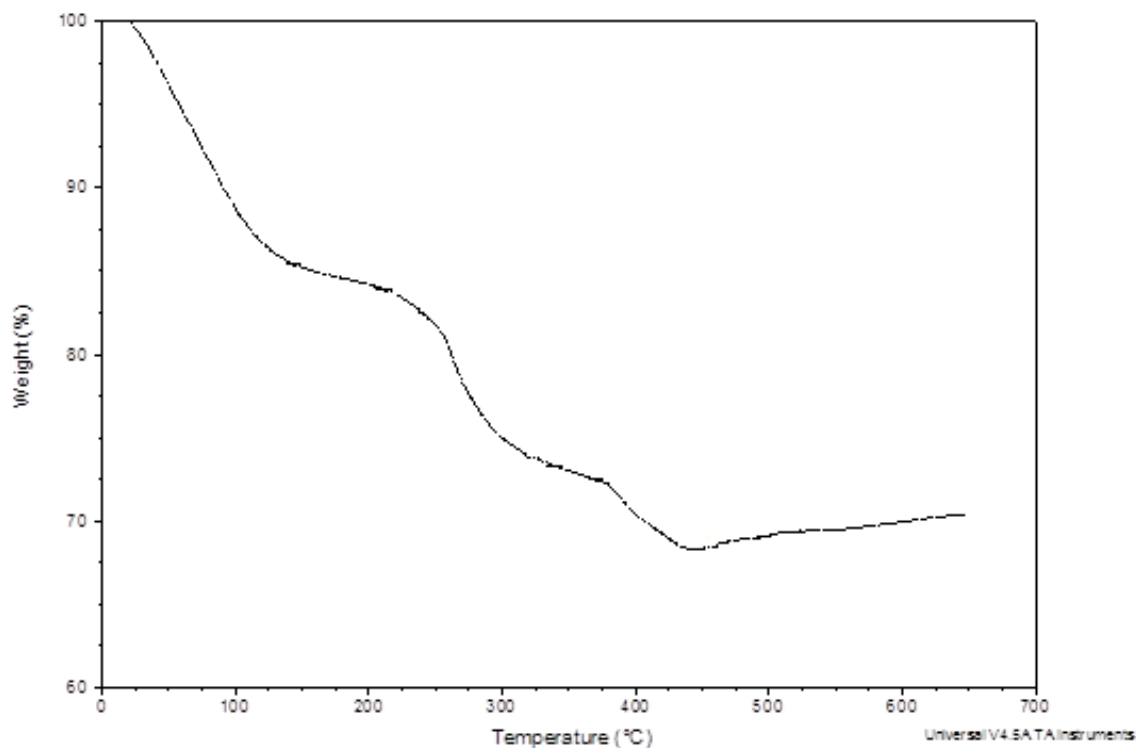
Figure 2.1 TGA profile of Mo-132a.

2.3   Instrumentation

2.3.1   Dynamic Light Scattering (DLS) and Zeta-potential Measurements (ζ-Pot)

The zeta-potentials were measured on the Malvern Zetasizer ZS in zeta analysis mode with a ζ-Pot range of -200 to +200 mV in a folded capillary cell operating at an effective voltage of 150 mV. The DLS measurements were performed on the same instrument utilizing a 173° backscattering detector. Individual solutions varying in the ratio of [Mo-132a]:[AuTMA] ranged from 0 to 40 were studied.

2.3.2   UV-visible Spectroscopy (UV-vis)

The UV-vis absorption measurements were performed on a Varian Cary 50 spectrophotometer in the wavelength range of 300 to 800 nm with a scan rate of 3000 nm/min. In a typical experiment, solutions from the ζ-Pot experiments were placed in 1.0 mL glass cuvettes.

2.3.3   Transmission Electron Microscopy (TEM)

TEM measurements were performed on a JEOL 2000EX instrument operated at 100 kV with a tungsten filament (SUNY-ESF, N.C. Brown Center for Ultrastructure Studies). Particle sizes were analyzed manually with statistical analysis performed using ImageJ software on populations of at least 100 counts.

2.3.4   Thermogravimetric Analysis (TGA):

TGA experiments were performed on a Perkin Elmer Pyris1 TGA with a thermal analysis gas station and under N_2 purge with a heating rate of 10 ^{o}C/min. The samples were dropcast as neat solutions or powders and dried thoroughly before analysis.

2.3.5   X-ray Photoelectron Spectroscopy (XPS)

XPS measurements were performed on a Surface Science Instruments (SSI) model SSX-100 at the Cornell Center for Materials Research (CCMR). It utilizes monochromated aluminum K-α x-rays (1486.6 eV) at an irradiation angle of 55°. The data was processed using CasaXPS software. The Mo-132+NP aggregates were rinsed and then dispersed on freshly cleaved HOPG substrates for analysis.

2.3.6   Electrophoretic Mobility

The CCD photograph (**Figure 2.6**) allowed estimation of the mobilities of Mo-132a and Mo-132c by taking their distances traveled, 0.7 cm and 1.2 cm, respectively, and the time run, 10 min (600 s). This allows us to calculate the velocity (v) which could then be used to find the electric field strength.

$$E = \frac{Applied\ Voltage}{Distance\ between\ electrodes} \tag{1}$$

From these experiments, the electric field strength was calculated to be 6.67 V·cm^{-1} (100V, 15cm). The electrophoretic mobility (μ_e) was calculated using Equation 2:

$$\mu_e = \frac{v}{E} \tag{2}$$

The calculated electrophoretic mobility (μ_e) of the Mo-132a and Mo-132c Keplerates is:

Mo-132a μ_e = 1.749e-4

$$\text{Mo-132c } \mu_e = 2.998e\text{-}4$$

The ratio for μ_e(Mo-132c): μ_e(Mo-132a) is ca. 1.7 while the idealized charge ratio for the Keplerates is 72:42 or 1.7.

2.3   Results and Discussion

In this section we first describe the synthesis and characterization of the molybdenum-oxide based Keplerates (Mo-132). We then describe the ability of these negatively charged clusters to mediate the electrostatic assembly of positively charged gold nanoparticles (AuTMA), and how changes in the Mo-132 charges influence assembly. **Scheme 2.1** presents an idealized view of the electrostatic assembly between the positively charged AuTMA and the negatively charged Keplerates Mo-132(a-c) to form the binary AuTMA-Mo-132(a-c) aggregates.
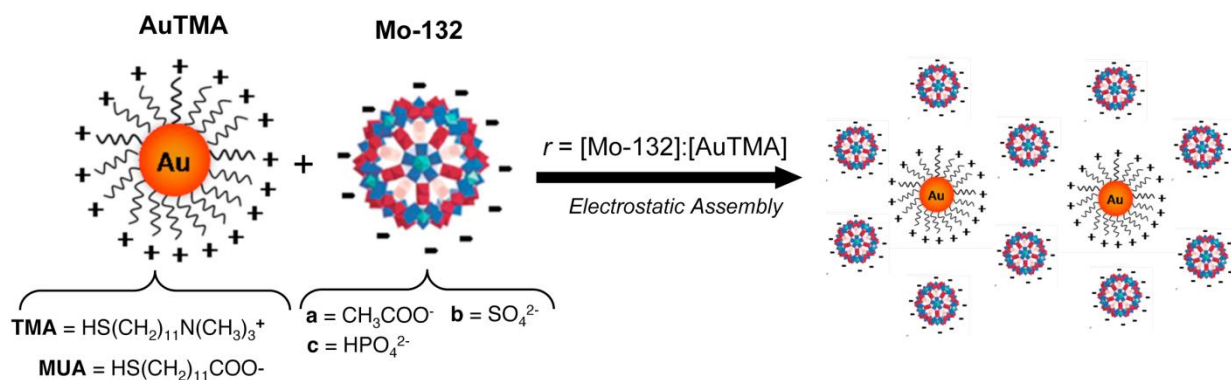
Scheme 2.1 An idealized representation of the electrostatic assembly between positively charged AuTMA and negatively charged Mo-132 analogues (a-c), forming Au-Mo-132(a-c) aggregates whose assemblies are tailored by molar ratios (*r*).

The prototypical compound $(NH_4)_{42}[Mo^{VI}_{72}Mo^V_{60}O_{372}(CH_3CO_2)_{30}(H_2O)_{72}] \cdot ca.$ {300 H_2O + 10 CH_3COONH_4} (alternatively, $(NH_4)_{42}[\{(Mo^{VI})Mo^{VI}_5O_{21}(H_2O)_6\}_{12} \{Mo^V_2O_4(CH_3COO)\}_{30}]$

41

·*ca*. {300 H_2O + 10 CH_3COONH_4} and denoted as Mo-132a) was prepared according to the literature method, exploiting the reduction of molybdate in the presence of hydrazine (eq 1)[44-48]:

132 MoO_4^{2-} + 15 $N_2H_6^{2+}$ + 30 CH_3COOH + 192 H^+ ------------->

$$[Mo^{VI}_{72}Mo^{V}_{60}O_{372} (CH_3CO_2)_{30} (H_2O)_{72}]^{42-} + 15\ N_2 + 84\ H_2O \qquad (1)$$
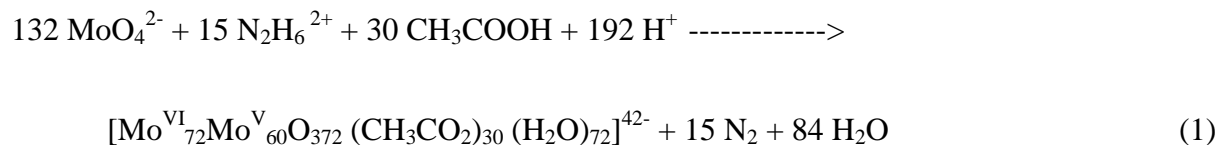
The derivatives of the type $(NH_4)_{72}[\{(Mo^{VI})Mo^{VI}_{5}O_{21}(H_2O)_6\}_{12}\{Mo^{V}_{2}O_4(L)\}_{30}]$ were prepared from the acetate-type cluster by ligand substitution (eq 2).

$[Mo^{VI}_{72}Mo^{V}_{60}O_{372} (CH_3CO_2)_{30} (H_2O)_{72}]^{42-} + 30\ H_nL$ ------------->

$$[\{(Mo^{VI})Mo^{VI}_{5}O_{21}(H_2O)_6\}_{12}\{Mo^{V}_{2}O_4(L)\}_{30}]^{(12 + 30n)-} (n = 1\ or\ 2) + \qquad (2)$$

$$30\ CH_3COOH\ + 30(n-1)H^+\ (L = SO_4^{2-}, HPO_4^{2-})$$
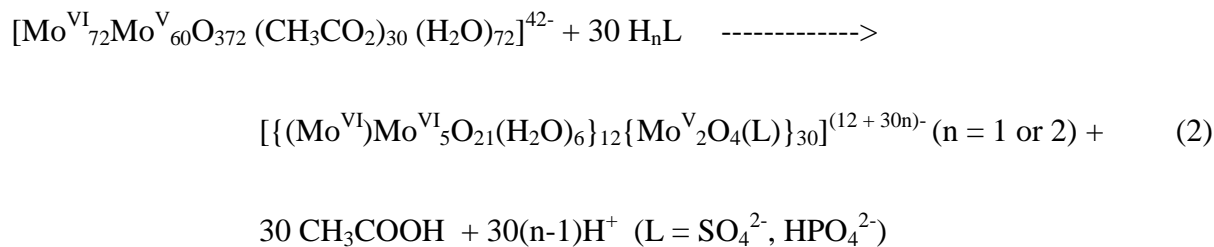
The purity of the various derivatives with L substituting for acetate ligands are readily monitored by the infrared spectra which exhibit the disappearance of the characteristic $\nu_{as,COO}$ band of the acetate at 1546 cm^{-1} (**Figure 2.2**).
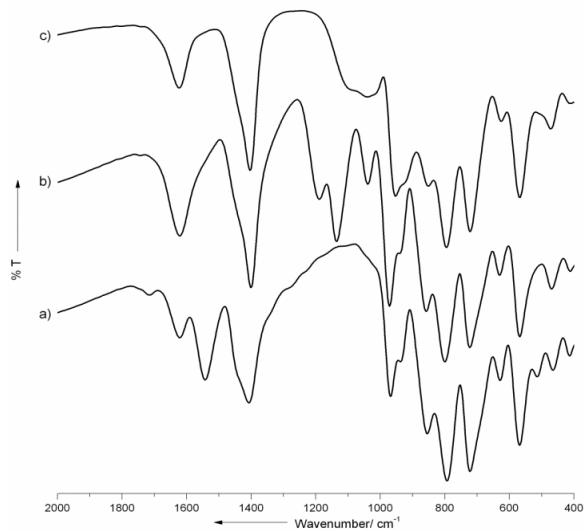
Figure 2.2. Infrared spectra (KBr disk) of a) Mo-132a, b) Mo-132b, c) Mo-132c).
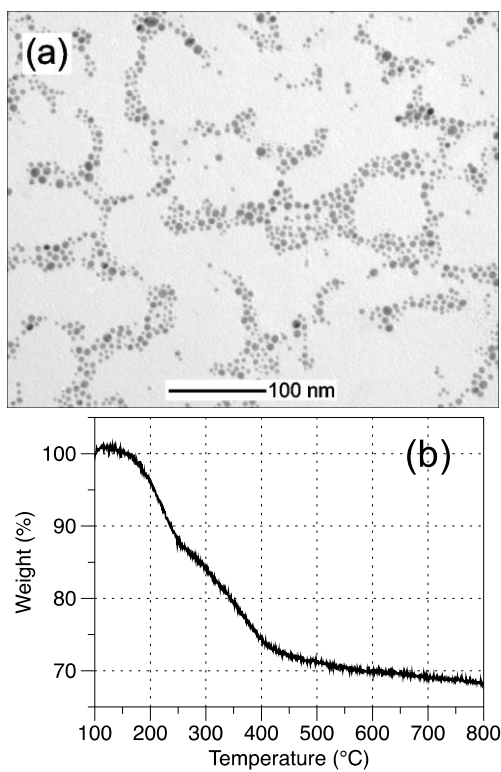
Figure 2.3 (a) TEM image of 4.4 ± 0.7 nm AuTOAB. (b) TGA analysis of the AuTMA showing a weight loss of 30.4%.

43

The gold nanoparticles were synthesized with a tetraoctyalammonium bromide (TOAB) capping, then modified with N,N,N-trimethyl(11-mercaptoundecyl)ammonium chloride (TMA) via ligand exchange. The resulting positively charged gold nanoparticles (AuTMA) had diameters of 4.4 ± 0.7 nm, as observed via transmission electron microscopy (TEM), which is shown in **Figure 2.3(a)**. Similar AuTMA have been used in a number of electrostatic assembly systems recently, including with similarly sized negative Au-NPs[12-14], NP-quantum-dot hybrids[17], and DNA[6,16]. Using previously described methods[13,56], XPS, and thermal gravimetric analysis (TGA), which determined the mass loss associated with TMA ligands **(Figure 2.3(b))**, we estimated that the AuTMA particles have the approximate composition of $Au_{3100}TMA_{760}Cl_{760}$. With both the Mo-132 clusters and the AuTMA particles in hand, we next studied their self-assembly.
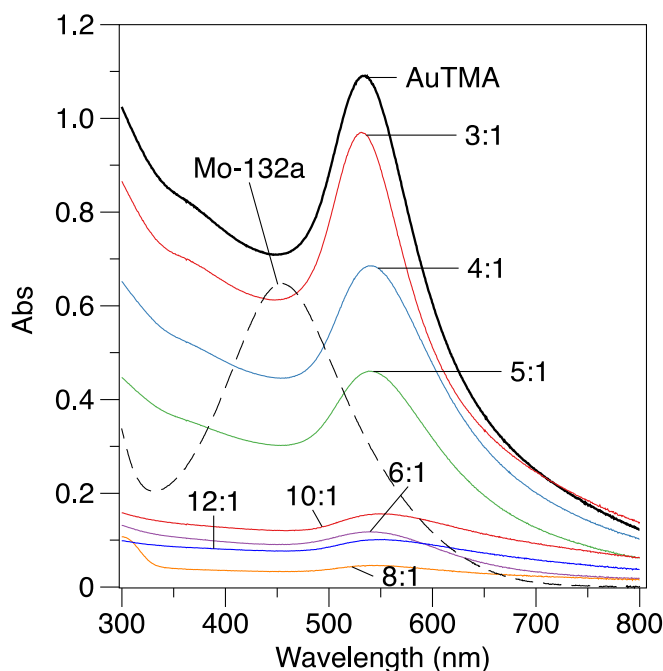
Figure 2.4 Representative UV-vis spectra of Mo-132a, AuTMA, and AuTMA+Mo-132 assemblies at r = [Mo-132]:[AuTMA] = 3:1, 4:1, 5:1, 6:1, 8:1, 10:1, 12:1.

To induce self-assembly between Mo-132a and AuTMA, an aliquot of Mo-132a was added to a solution of AuTMA ([Au] = 0.6 μM) at increasing molar ratios, r = [Mo-132]:[Au] = 1 - 35. Immediately upon addition of Mo-132a, a colorimetric transition from dark red to red was observed, and precipitates (i.e., POM-AuTMA aggregates) were noticed within minutes at increased r **(Figure 2.4)**. The progress of the assembly, the aggregate size, and the charges of the aggregates were monitored *in-situ* with UV-vis, DLS and zeta potential measurements (ζ-Pot). **Figure 2.4** shows the optical absorption characteristics of the assembly system. The Mo-132 absorption originates from intervalence charge transfer (IVCT) between Mo^V and Mo^{IV} centers of the cluster (note the presence of a string Mo-Mo bond), while the AuTMA absorption arises from the surface plasmon resonance band (SPR) of the AuNPs due to the collective oscillation of electrons in the presence of electromagnetic radiation[59-61]. Due to the much higher extinction coefficient of the AuNP, the SPR is the prominent feature in the assembly spectra. Because the SPR is sensitive to changes in particle size, local dielectric media changes, as well as coupling between particles in close proximity, it serves as a convenient method to follow self-assembly. For instance, **Figure 2.4** shows the UV-visible spectra of Mo-132a, AuTMA, and the Mo-132a+AuTMA electrostatic assemblies. At r >3, a subtle red-shift is observed, as well as a decrease in extinction, which is attributed to the first assembly of the relatively small AuTMA-Mo-132 clusters, followed by the growth of a large aggregate, which decreases extinction due to both the screening of interior particles, as well as precipitation of the material from solution. Interestingly, the spontaneous precipitation of the AuTMA-Mo-132 aggregates occurs at r =10-14. This phenomenon was then probed by ζ-Pot and DLS methods.

Figure 2.5(a) shows a representative set of ζ-Pot measurements for the Mo-132a + AuTMA system at increasing r. The initial AuTMA particle has a charge of $\zeta = 45.5 \pm 1.72$ mV, which is consistent with previous studies[12-14,16,17]. This value decreases slowly at $r = 0 - 5$, which is indicative of the Mo-132a interacting with and screening the AuTMA charge. At $r > 5$ a decrease in ζ is detected, with a neutralization ($\zeta \approx 0$ mV) occurring at $r \approx 10$. At $r > 10$ there is a negative overall charge ($\zeta \approx$ -25 mV) which remains relatively invariant, due to both the presence of excess Mo-132a, as well as the likelihood that each assembled aggregate is terminated by it. This trend towards electroneutrality corresponds closely with the bulk precipitation observed via UV-vis. For example, **Figure 2.5(b)** shows a plot of the SPR absorbance maxima (520 nm), measured in parallel to ζ-Pot measurements. At $r = 5$, a drop in absorbance is detected, correlating with the aggregation. Interestingly, control experiments using the negatively charged AuMUA showed a stable ζ-Pot of $\approx$ -40.5 mV **(Figure 2.5(a))** and little to no change in SPR. The hydrodynamic properties of the system were then probed by DLS. **Figure 2.5(b)** shows a plot of hydrodynamic diameter (D_h) with r. As observed above, rapid aggregate growth to $D_h > 600$ nm was measured at $r \approx 5$.
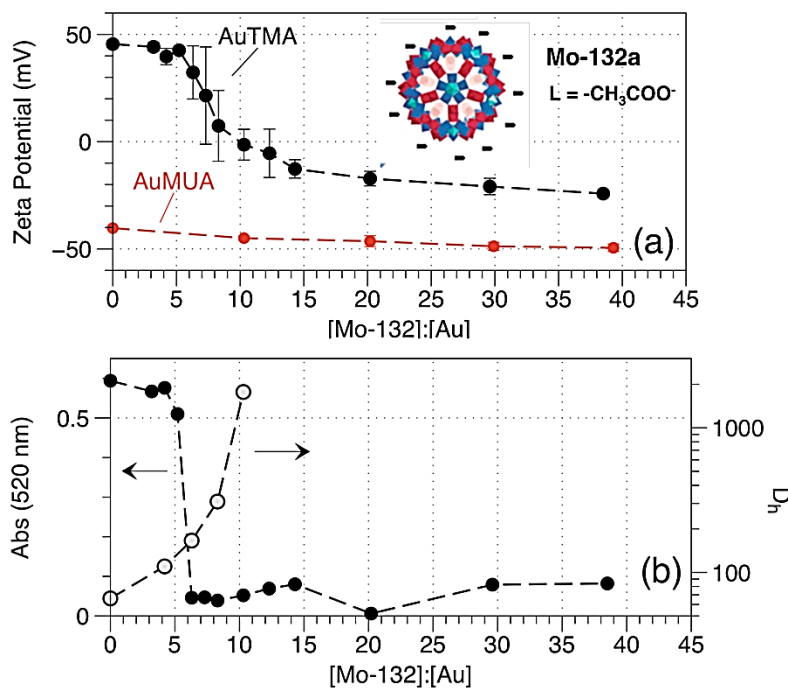
Figure 2.5 (a) Zeta potential (ζ-Pot. measurements for the Mo-132a mediated assembly of AuTMA and AuMUA control at increasing r = [Mo-132a]:[AuTMA]. (b) The corresponding plot of absorbance at 520 nm decreases, and D_h increases with r.

The Mo-132a mediated aggregation was visualized using TEM. **Figure 2.6** shows a representative set of TEM micrographs at r = 6 (a), 10 (b), and 20 (c). At r = 6, which corresponds to a scenario below the equivalence point, regions of assembled AuTMA with chain like morphologies are observed **(Figure 2.6(a))**. These assembled morphologies are in contrast to those micrographs collected for AuTMA alone **(Figure 2.3(a))**, which revealed random organization. In contrast, at the point of electroneutrality **(r = 10, Figure 2.6(b))**, micrometer sized aggregates are observed, which consist of clearly separated individual AuTMA assembled in close-packed geometries. The order and extent of the packing is disrupted by the polydispersity of AuTMA. Interestingly, above the neutrality point, chain like aggregates are

again observed, which may be due to the saturation of the AuTMA by Mo-132a, and the further

repulsion between the negative charges.
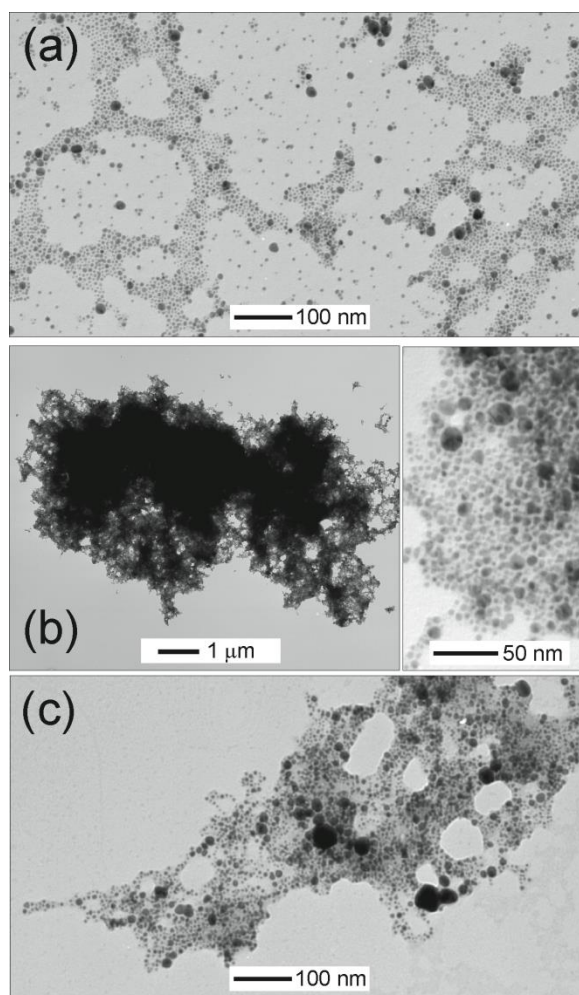
Figure 2.6 Representative TEM micrographs of Mo-132a mediated assembly of AuTMA at $r = 6$ (a), 10 (b, inset) and 20 (c).
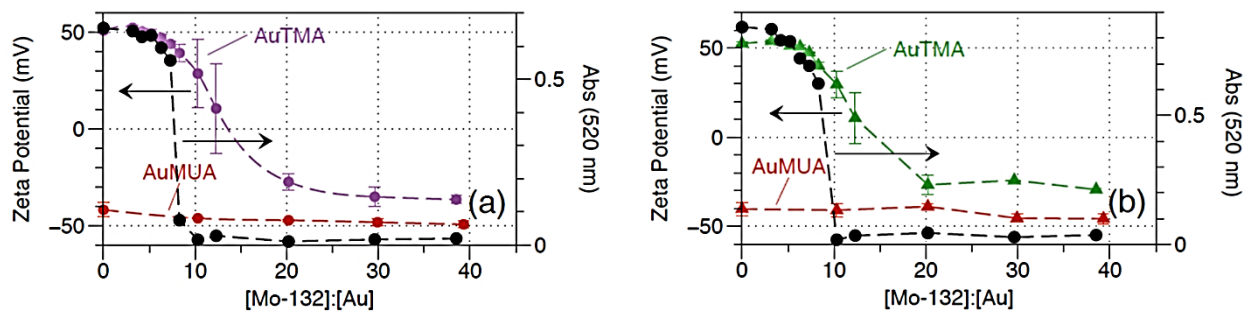
Figure 2.7 The ζ –Pot. measurements and UV-vis monitoring (black) of the electrostatic assembly of (a) Mo-132b and (b) Mo-132c with AuTMA and AuMUA.

These results indicate the successful electrostatic assembly between negatively charged Mo-132a clusters and positively charged AuTMA. The strength of the interaction, as well as the screening potential is related to the charge of the nanoscale objects, the counter ion, as well as the ionic strength of the solution. Such charges can be tailored, by either manipulating the number of TMA ligands at each Au NP, or by performing ligand substitution at the Mo-132a cluster. To probe this, we chose the latter option using a series of Mo-132 analogues. For example, **Figure 2.7(a)** shows the DLS and UV-vis monitoring of the assembly between AuTMA and Mo-132b, which in contrast to Mo-132a **(Figure 2.5(a))**, has an idealized negative charge of 72 due to its internal sulfate ligand. The actual charges associated with Mo-132a and Mo-132b are a distribution centered at these values (i.e., -42 and -72) due to the incorporation into the internal cavity of the cluster and surface adhesion of NH_4^+ cations. However, the general magnitude of these charges was substantiated by measuring the electrophoretic mobilities of Mo-132a and Mo-132c **(Figure 2.8)**, which were found to be in the ratio of 1.7:1.0, which is identical to the idealized charge ratio of 72:42.
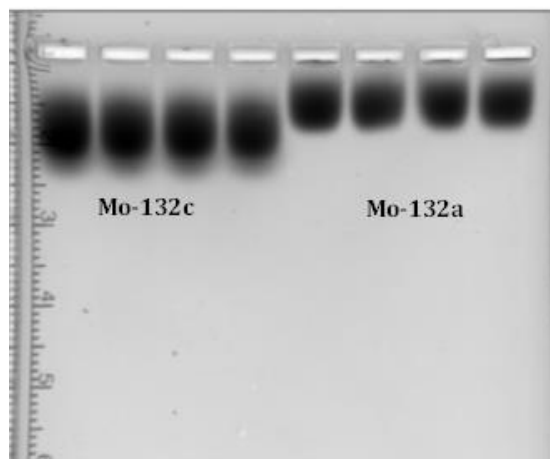
Figure 2.8. CCD camera photograph of gel electrophoresis for (Mo-132a) and (Mo-132c) (four wells each) in a 1% agarose gel.

The results for the assembly between Mo-132b and Mo-132c with both AuTMA and AuMUA are shown in **Figure 2.6**. Both show similar assembly behavior; however, the observed precipitation and electroneutrality points for both Mo-132b and Mo-132c with AuTMA are shifted towards higher Mo-132 concentrations, $r \approx 14$ **(Table 2.1)**.

Table 2.1: Correlation of Idealized Mo-132 Charges and Determined Equivalence Point.

Mo-132	R	Charge[a]	$r_{(E0)}$[b]
Mo-132a	CH_3COO^-	-42	≈ 10
Mo-132b	SO_4^{2-}	-72	≈ 14
Mo-132c	HPO_4^{2-}	-72	≈ 14

[a]POM charge based on number of negatively charged ligands for each Mo-132 determined by X-ray crystallography [b]Ratio at the point of electroneutrality (r_{E0}) determined from ζ plots.

At first sight, these results appear counterintuitive; that is, r_{E0}, the ratio at the point of electroneutrality, of 10 for a Mo-132a of charge -42 and r_{E0} of 14 for Mo-132b,c with a charge of

-72, since the latter presumably would have a greater attractive force for AuTMA. However, it must be appreciated that the zeta potential is related to colloid stability and is a measure of the electrical potential at the boundary between the Stern layer and the diffuse layer in the double layer model. Furthermore, it must be appreciated that both the AuTMA and Mo-132a-c carry a firmly attached layer of counter-ions. The incoming nanomaterial (AuTMA or Mo-132a-c) must first encounter a double-layer, and then displace the surface counter-ions. These electrostatic changes at the interfaces of the particles influence the effective ζ -Pot being measured. For instance, as the particles come together, a small cluster will first form, where a AuTMA will be covered with Mo-132a-c, or linked together by Mo-132a-c, which forms a new Stern layer, and results in a change to ζ -Pot **(Scheme 2.2)**.
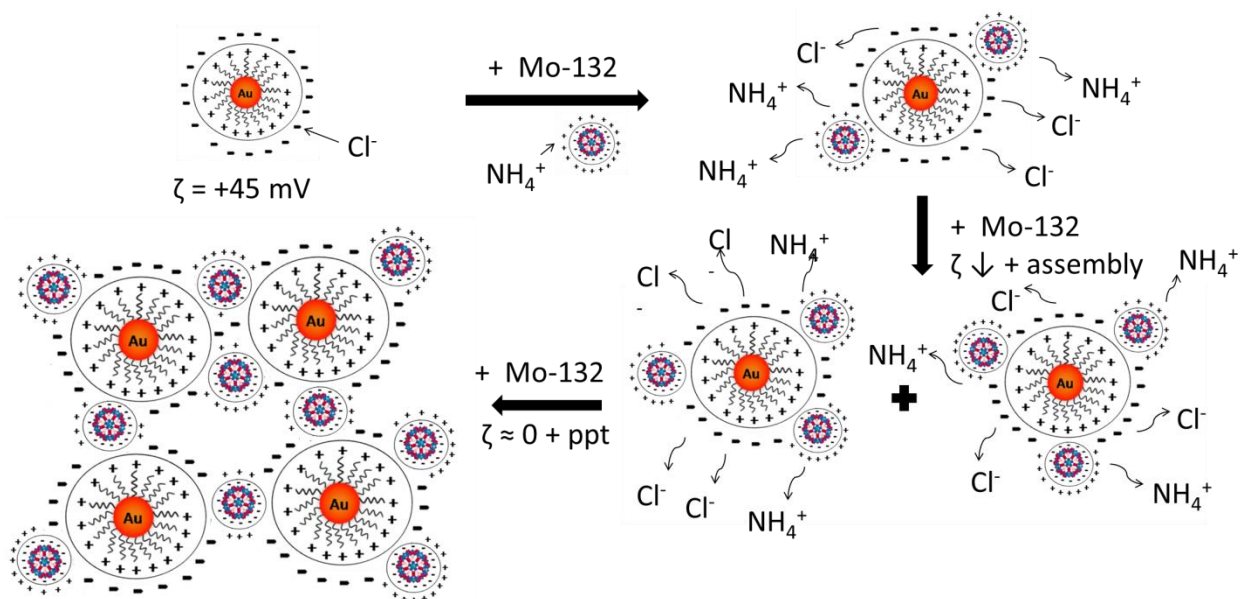
Scheme 2.2 Schematic Representation of the Charge Distribution in the Stern Layers of the AuNP and the Keplerate Particle and of the Stern Layer Surrounding the Resultant Aggregate.

This further involves the displacement of Cl^- anions from AuTMA, and NH_4^+ cations from Mo-132a-c. This ion displacement will be related to charge change, ion charge, and ionic strength (i.e. Debye length). For Mo-132a, the internal charge is -42, which regulates the strength of binding of the NH_4^+ counter-ions. For Mo-132b,c, the internal charge is -72 due to the divalent anions, which requires a higher concentration of NH_4^+ counter-ions, and a stronger coulombic attraction. This in turn lessens the attraction for AuTMA, and decreases kinetics, resulting in the higher equivalence point. To further investigate the role that counter-ions play in these assemblies, we performed AuTMA+Mo-132a assembly at different ionic strengths (0, 5, 10, 20 mM NH_4Cl). The increase in ionic strength effectively decreases the double layer at the particle interfaces, while screening their interactions. At higher ionic strengths the equivalence point was extended to larger r_{E0} (**Figure 2.9**), confirming the slower assembly kinetics.
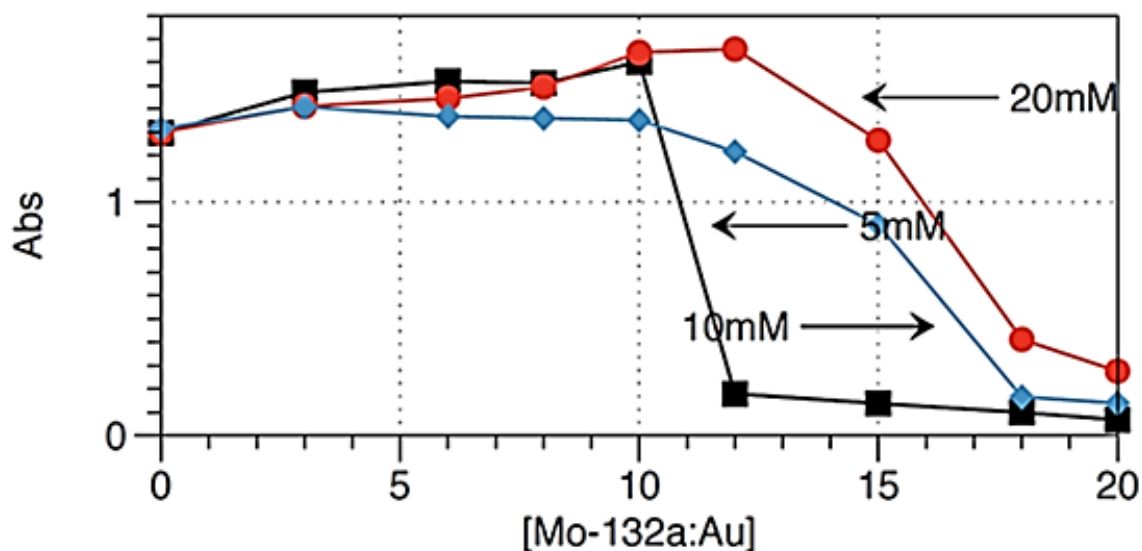
Figure 2.9. Comparison of UV-visible spectra of assemblies of Mo-132a and AuTMA in NH_4Cl solutions of different ionic strengths (5mM, 10mM, and 20mM).

Taken together, these results show that the electrostatic assembly of AuTMA by Mo-132 type Keplerates is possible, with tuning of charge allowing for manipulation of the assembly. The equivalence point is achieved at a ratio of [Mo-132a:AuTMA] of ca. 10:1, requiring that the precipitated species has the idealized composition $(Au_{3100}TMA_{760})(Mo\text{-}132a)_{10}Cl_{340+x}(NH_4)_x$, which is consistent with the XPS analysis which provides the Mo/Au ratio of 28:72 **(Table 2.2)**.

Table 2.2: Analysis of Mo-132a +AuTMA aggregates from XPS.

[Mo-132]:[Au]	Feed Ratio (At%)[1]		XPS Ratio (At%)[2]	
r	Mo	Au	Mo	Au
6	20	80	22	78
8	25	75	23	77
10	30	70	28	72
12	34	66	30	70

[1]Atomic % based on molar feed ratios (r) of Mo-132 and Au NPs after considering the number of Au atoms per NP and Mo atoms per Mo-132 cluster.

[2]Atomic % measured via XPS on sedimented Mo-132a + AuTMA aggregates.

Using a ratio of [Mo-132b]:[AuTMA] of ca. 14:1, the idealized composition will require charge balancing of the ammonium cations to balance the negative charge of Mo-132b anions $(Au_{3100}TMA_{760})(Mo\text{-}132b)_{14}Cl_y(NH_4)_{248+y}$. Thus, future work focusing on aggregates incorporating AuNPs of variable charges and of different shapes and sizes may provide further insights into the mechanism, and will be the topic of subsequent reports.

2.4   Conclusions

In summary, a series of anionic Mo-132 Keplerates with different charges has been synthesized and characterized along with a cationic AuNP capped with trimethylammonium

terminated monolayers. The electrostatic assembly between these nanomaterials was

investigated for the first time, and successful assembly was demonstrated using UV-vis, DLS,

TEM, and ζ-Pot analysis. The rapid bulk precipitation from nanoscopic entities to micron scale

aggregates was observed at the point of electroneutrality, which was typically at a [Mo-

132]:[Au] molar ratio of 10~14 depending on the ligand associated with Mo-132. These results

indicate that precipitation at the equivalence point is related to charge balance or

electroneutrality and that counterions at both the Mo-132 and AuNP play a significant role in

assembly. Furthermore, the findings suggest investigations of AuNPs of different dimensions,

modified charges and nonspherical shapes in combination with Keplerates of different

dimensions and charges to construct materials consisting of Keplerate units surrounding AuNPs

in a close-packed like arrangments, similar to traditional ionic lattices.

2.5   Acknowledgement

2.6   References

[1]   D.-L. Long, R. Tsunashima, L. Cronin, *Angew. Chem. Int. Ed.* **2010**, 47, 1736-1758.

[2]   A. Müller, S. Roy, *Oxomolybdates: From Structures to Functions in a New Era of Nanochemistry, eds.* Wiley-VCH, Weinheim, **2004,** 452.

[3]   A. Müller, P. Gouzerh, *Chem. Soc. Rev.* **2012**, 41, 7431-7463.

[4]   C. Schäffer, A.M. Todea, P. Gouzerh, A. Müller, *Chem. Commun.* **2012**, 48, 350-352.

[5]   D. Volmer, A.D. Chesne, D.G. Kurth, H. Schnablegger, P. Lehmann, M. J. Koop, A. Müller, J. Am. Chem. Soc. **2000**, 122, 1995-1998.

[6]   R. Shenhar, V. M. Rotello, *Acc. Chem. Res.* **2003**, 36, 549-561.

[7]   F. Stellacci, *Nat. Mater.* **2005**, 4, 113-114.

[8]   K. J. M. Bishop, C. E. Wilmer, S. Soh, B. A. Grzybowski, *Small* **2005**, 5, 1600-1630.

[9]   D. A. Walker, B. Kowalczyk, M. O. de la Cruz, B. A. Grzybowski, *Nanoscale* **2011**, 3, 1316-1344 and references therein.

[10]   E. V. Shevchenko, D. V. Talapin, N. A. Kotov, S. O'Brien, C. B. Murray, *Nature* **2006**, 439, 55-59.

[11]   M. E. Leunissen, C. G. Christova, A.-P. Hynninen, C. P. Royall, A. I. Campbell, A. Imhof, M. Dijkstra, R. van Roij, A. van Blaaderen, *Nature* **2005**, 437, 235-240.

[12]   A. M. Kalsin, M. Fialkowski, M. Paszewski, S. K. Smoukov, K. J. M. Bishop, B. A. Grzybowski, *Science* **2006** 420-424.

[13]   A. M. Kalsin, A. O. Pinchuk, S. K. Smoukov, M. Paszewski, G. C. Schatz, B. A. Grzybowski, *Nano. Lett.* **2006**, 6, 1896-1903.

[14]   A. M. Kalsin, B. Kowalczyk, S. K. Smoukov, R. Klajn, B. A. Grzybowski, *J. Am. Chem. Soc.* **2006**, 15046-15047.

[15]   P. D. Yates, G. V. Franks, S. Biggs, G. J. Jameson, *Colloids Surf. A-Physicochem. Eng. Asp.* **2005**, 255, 85-90.

[16]   C.-C. You, M. De, V. M. Rotello, *Curr. Opin. Chem. Bio.***2005**, 9, 639-646.

[17]   J. Kolny, A. Kornowski, H. Weller, *Nano. Lett.* **2002**, 2, 361-364.

[18]   M.-C. Daniel, D. Astruc, *Chem. Rev.* **2004**, 104, 293-346.

[19]   O. D. Velev, *Science* **2006**, 312, 376-377.

[20]   F. X. Redl, K.-S. Cho, C. B. Murray, S. O'Brien, *Nature* **2003**, 423, 968-971.

[21] E. V. Shevchemko, D. V. Talapin, C. B. Murray, S. O'Brien, *J. Amer. Chem. Soc*. **2006**, 128, 3620-3637.

[22] J. Chen, A. Dong, J. Cai, X. Ye, Y. Kang, J. M. Kikkawa, C. B. Murray, *Nano. Lett.* **2010**, 10, 5103-5108.

[23] J. Chen, X. Ye, C. B. Murray, *ACS NANO* **2010**, 4, 2374-2381.

[24] D.-L. Long, E. Burkholder, L. Cronin, *Chem. Soc. Rev.* **2007**, 36, 105-121.

[25] M. Fernandez-Garcia, A. Martinez-Arias, J. C. Hanson, J. A. Rodriguez, *Chem. Rev.* **2004**, 104, 4063-4104.

[26] M. T. Pope, A. Müller, *Polyoxometalate Chemistry: From Topology via Self-Assembly to Applications,* eds. Kluwer, Dordrecht, **2001**.

[27] M. T. Pope, *Heteropoly and Isopoly Oxometalates*, Springer, Berlin, **1983**.

[28] P. Gouzerh, M. Che, *Actualité Chimique* **2006**, 298, 9-22.

[29] D. J. Long, L. Cronin, *Chem. Eur. J.* **2006**, 12, 3698-3706.

[30] J.-M. Brégeault, M. Vennat, L. Salles, J.-Y. Piquemal, Y. Mahha, E. Briot, P. C. Bakala, A. Atlamsani, R. Thouvenot, *J. Mol. Catal. A* **2006**, 250, 177-189.

[31] N. Casan-Pastor, P. Gómez-Romero, *Front. Bioscience* **2004**, 9, 1759-1770.

[32] P. Kögerler, B. Tsukerblat, A. Müller, *Dalton Trans.* **2010**, 39, 21-36.

[33] E. Balogh, A.M. Todea, A. Müller, W. H. Casey, *Inorg. Chem.* **2007**, 46, 7087-7092.

[34] A. M. Todea, A. Merca, H. Bögge, J. van Slageren, M. Dressel, L. Engelhardt, M. Luban, T. Glaser, M. Henry, A. Müller, *Angew. Chem. Int. Ed.* **2007**, 46, 6106-6110.

[35] A. Müller, S. Sarkar, S.Q.N. Shah, H. Bögge, M. Schmidtmann, Sh. Sarkar, P. Kögerler, B. Hauptfleisch, A. X. Trautwein, V. Schünemann, *Angew. Chem. Int. Ed.* **1999**, 38, 3238-3241.

[36] A. Müller, E. Krickemeyer, S. K. Das, P. Kögerler, S. Sarkar, H. Bögge, M. Schmidtmann, Sh. Sarkar, *Angew. Chem. Int. Ed.* **2000**, 39, 1612-1614.

[37] D. Gatteschi, R. Sessoli, J. Villain, *J. Molecular Nanomagnets,* Oxford Univ. Press, Oxford, **2006**.

[38] A. Müller, M. Luban, C. Schröder, R. Modler, P. Kögerler, M. Axenovich, J. Schnack, P. Canfield, S. Bud'ko, N. Harrison, ChemPhysChem. **2001, 2,** 517-521.

[39] A. Müller, E. Krickemeyer, H. Bögge, M. Schmidtmann, F. Peters, *Angew. Chem. Int. Ed.* **1998**, 37, 3360-3363.

[40] T. Liu, *Langmuir* **2010**, 26, 9202-9213.

[41] M. L. Kistler, A. Bhatt, G. Liu, D. Casa, T. Liu, *J. Am. Chem. Soc.* **2007**, 129, 6453-6460.

[42] M. L. Kistler, K. G. Patel, T. Liu, *Langmuir* **2009**, 25, 7328-7334.

[43] T. Liu, B. Imber, E. Diemann, G. Liu, K. Cokleski, H. Li, Z. Chen, A. Müller, *J. Am. Chem. Soc.* **2006**, 128, 15914-15920.

[44] A. A. Verhoeff, M. L. Kistler, A. Bhatt, J. Pigga, J. Groenewold, M. Klokkenburg, S. Veen, S. Roy, T. Liu, W. K. Kegel, *Phys. Rev. Lett.* **2007**, 99, 066104.

[45] Q. Zhang, L. He, H. Wang, C. Zhang, W. Liu, W. Bu, *Chem. Comm.* **2012**, 48, 7067-7069.

[46] A. Buchkremer, M. J. Linn, J. U. Timper, T. Eckert, J. Mayer, W. Richtering, G. von Plessen, U. Simon, *J. Phys. Chem.* **2014**, 118, 7174-7184.

[47] O. Petina, D. Rehder, E. T. K. Haupt, A. Grego, I. A. Weinstock, A. Merca, H. Bögge, J. Szakács, A. Müller, *Angew. Chem. Int. Ed.* **2011**, 50, 410-414.

[48] A. Ziv, A. Grego, S. Kopilevich, L. Zeiri, P. Miro, C. Bo, A. Müller, A. I. Weinstock, *J. Am. Chem. Soc.* **2009**, 131, 6380-6382.

[49] A. Müller, *Nature* **2007**, 447, 1035.

[50] A. Müller, S.K. Das, E. Krickemeyer, C. Kuhlmann, *Inorg. Synth.* **2004**, 34, 191-200.

[51] L. Cronin, E. Diemann, A. Müller A., *Polyoxomolybdate Clusters: Nanoscopic Wheels and Balls in Inorganic Experiments,* Woollins, J. D., ed., Wiley-VCH, Weinheim, **2003**, pp. 340-346.

[52] A. Müller, E. Krickemeyer, H. Bögge, M. Schmidtmann, B. Botar, M. O. Talismanova, Angew. *Chem. Int. Ed.* **2003**, 42, 2085-2090.

[53] A. Müller, Y. Zhou, H. Bögge, M. Schmidtmann, T. Mitra, E. T. K. Haupt, A. Berkle, *Angew. Chem. Int. Ed.* **2006**, 45, 460-465.

[54] A. Müller, S.K. Das, S. Talismanov, S. Roy, E. Beckmann, H. Bögge, M. Schmidtmann, A. Merca, A. Berkle, L. Allouche, Y. Zhou, L. Zhang, Angew. *Chem. Int. Ed.* **2003**, 42, 5039-5044.

[55] J. Tien, A. Terfort, G. M. Whitesides, *Langmuir* **1997**, 13, 5349-5355.

[56] O. Uzun, Y. Hu, A. Verma, S. Chen, A. Centrone, F. Stellacci, *Chem. Comm.* **2008**, 196-198.

[57] N.R. Jana, X. Peng, *J. Am. Chem. Soc.* **2003**, 125, 14280-14281.

[58] M. M. Maye, I-Im S. Lim, J. Luo, Z. Rab, D. Rabinovich, T. Liu, C.-J. Zhong, *J. Am. Chem. Soc.* **2005**, 127, 1519-1529.

[59]   S. Srivastava, B. Samanta, P. Arumugam, G. Han, V. M. Rotello, *J. Mater. Chem.* **2007**, 17, 52-55.

[60]   S. Stoeva, K.J. Klabunde, C. M. Sorensen, I. Dragieva, *J. Am. Chem. Soc*. **2002**, 124, 2305-2311.

[61]   M. A. El-Sayed, *Acc. Chem. Res.* **2004**, 37, 326-333.

Chapter 3

Size Comparison of Gold Nanoparticles with Mo-132

via Electrostatic Assembly

3.1   Introduction

Nanoscience is currently thriving due to the advancements of improved nanoparticle syntheses and better understanding of the physicochemical and optoelectronic properties of these materials.[1-9] One aspect of nanoscience that has a direct impact on commercial application of nanoscale systems is their assembly into superstructures of predefined geometry either in solution or on solid interface.[2] Recently, self-assembly of various nanoscopic entities has provided the opportunity for advances in catalytic, electronic, sensing, and biological studies.[3-26] Specifically, electrostatic assembly has yielded three-dimensional binary superlattices comprised of gold nanoparticles (AuNPs) and protein cages where interparticle interactions were controlled by tuning both pH and the Debye screening length.[26] Grzybowski et.al. have extensively studied oppositely charged Au and Ag nanoparticles forming a "diamond-like" crystal structure comprised of tens of millions of individual metal nanoparticles. He established that the size selectiveness during crystallization of oppositely charged metal nanoparticles plays an important role in the crystallization of these electrostatic assemblies, where "good-quality supracrystals" would form only when an overlap in size distribution was observed.[27]
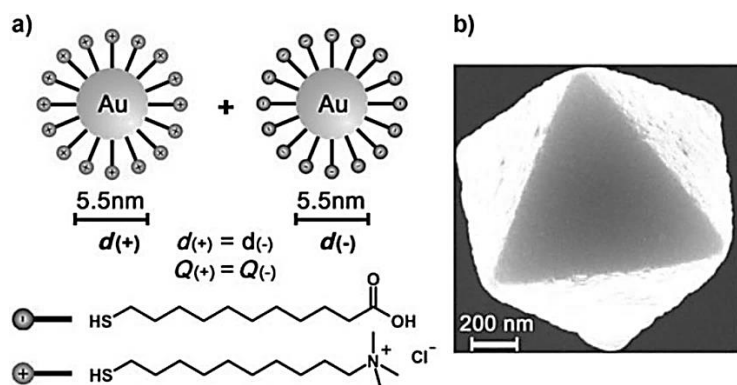
Figure 3.1: a) Scheme of the oppositely charged gold nanoparticles. Positively charged NPs are functionalized with *N,N,N*-trimethyl(11-mercaptoundecyl)ammonium chloride (TMA); negatively charged NPs are coated with a SAM of deprotonated mercaptoundecanoic acid (MUA). b) An SEM image of a supracrystal comprising ≈2.5 million NPs. Reproduced with permission from reference 27. Copyright © 2009 Elsevier.

As described in Chapter 2, we have recently observed electrostatic interactions between cationic AuNPs mediated with anionic polyoxometalates (POMs) to obtain large micron aggregate assemblies.[28] However, highly ordered structures of these nanoscopic entities were not achieved at this time. With the molecular size relation to self-assembly behavior in this system remaining unclear, a size regime with varying AuNPs may clarify the findings in our previous work and allow development of a crystal-based system with AuNPs and POM entities.
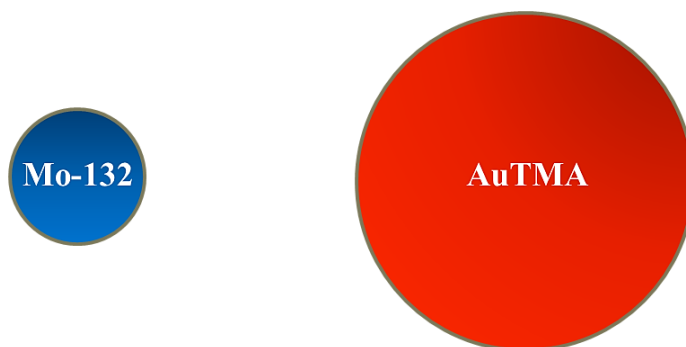
Figure 3.2: An illustration of the size comparison of the Mo-132 and 4.4 nm AuTMA nanoscopic entities.

The complexity of both the electrostatic repulsion and van der Waals attractions within the double layer has left much to be studied to understand how these nanoscopic entities interact with one another. The counter-intuitive results between AuNPs and POMs, where the more highly charged anionic POM produced a larger r_{E0}, led us to investigate the reproducibility of these observations across a size scale of AuNPs. To further examine our results, the relationship of nanoparticle curvature to electrostatic screening effects was considered. It is known that the role the curvature of the nanoparticle plays an important role in the loading of thiolated ligands onto AuNPs.[29-32] This concept can be used in determining the amount of surface area N,N,N-trimethylamine head groups occupy compared to the amount of "free" space surrounding the Au core. This "free" space can be used to predict how well other AuNPs and POMs can "see" the cationic head groups without being screened by counter-ions in the double layer.

The relationship of ligand surface density to nanoparticle curvature has been described by Grzybowski *et al.*[32] In short, it was stated that ligand surface density is higher in regions of low curvature, and vice versa, for gold nanorods and nano-dumbbells. In terms of spherical nanoparticle size, as the diameter of the nanoparticle increases, the curvature of the surface decreases. This correlates with the ligand surface density, where the distance between the TMA head groups for low-curvature (large diameter) nanoparticles is less than that for high-curvature (small diameter) nanoparticles.
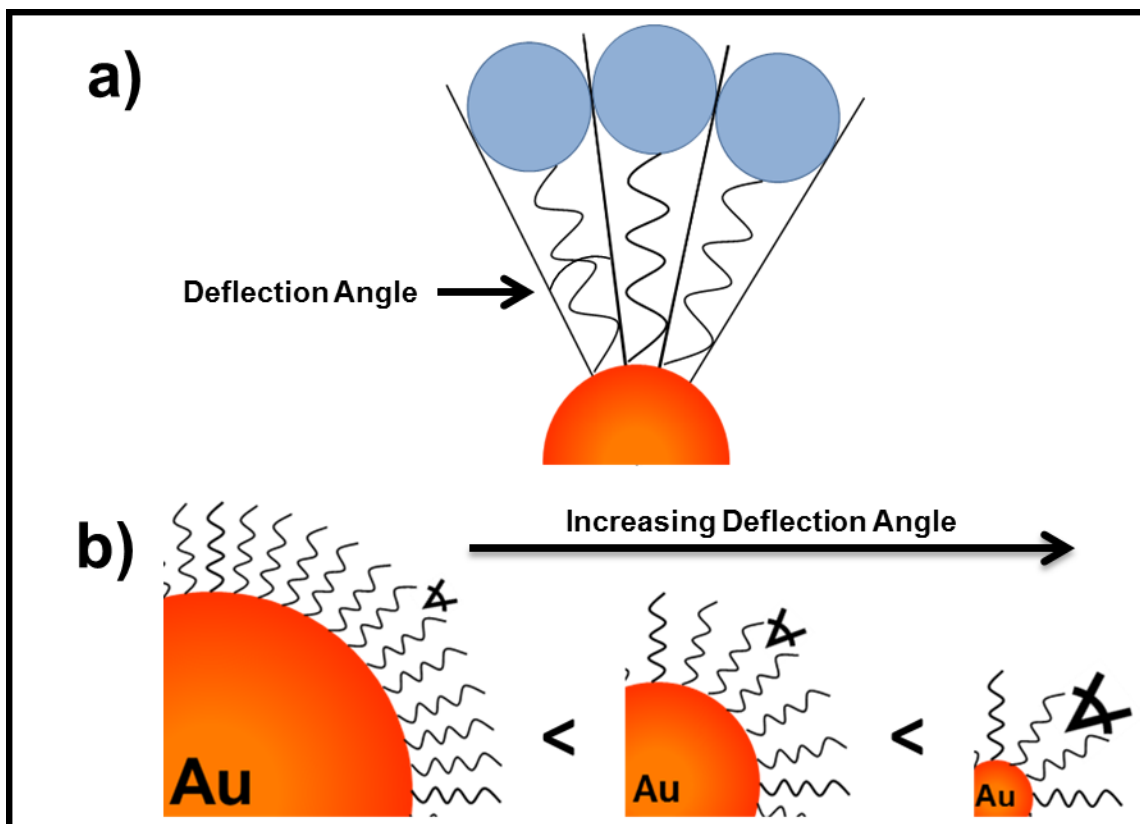
Figure 3.3: (a) Illustration of the deflection angle between NMe_3^+ head groups. **(b)** Illustration depicting an increasing deflection angle of 1.6, 4.4, and 8.6 nm Au cores as curvature of the AuNP increases. The curvature of the core plays a role in the spatial distribution of NMe_3^+ head groups.

The deflection angle relates the ligand surface density and curvature (**Figure 3.3**).[29,33] The deflection angle is directly related to the radius of curvature of the AuNP and determines the spatial arrangement of the thiolate ligands as well as how this arrangement is dependent upon the AuNP radius.[29] These factors play a crucial role in the screening effects of counter-ions in the double layer. For example, smaller nanoparticles will have a higher curvature which increases the distance between head groups on the surface. This separation lowers surface charge density, thus lowering the concentration of counter-ions in the double layer, thus allowing for the charges of both nanomaterials to be "visible" for attraction to occur.

In Chapter 2, counterintuitive findings led us to investigate a size range of AuNPs that this phenomenon encompasses. We hypothesized that changing the core diameter of AuNPs may lead to aggregates containing crystalline characteristics. In this study, AuNPs of 1.6 and 8.6 nm diameter were synthesized and functionalized with the self-assembled monolayer (SAM) of N,N,N-trimethyl(11-mercaptoundecyl)ammonium chloride (TMA), to render the surface positively charged. The electrostatic assembly between the Mo-132(a-b) clusters and AuTMA of ca. 1.6 and 8.6 nm dia. was investigated in terms of the aggregation dependence on the [Mo-132]:[Au] stoichiometry. The unanticipated results have led to a more detailed understanding to how these nanomaterials link together and parameters which may reveal key parameters to crystallization.

3.2   Experimental

All chemicals were used as obtained without further purification. Acetic acid, sulfuric acid, hydrochloric acid, ammonium acetate, sodium chloride, and sodium acetate, were all purchased from Fisher. Hydrazine sulfate, ammonium chloride, ethanol, triphenylphosphine, trisodium citrate, diethyl ether, and gold (III) chloride trihydrate were all purchased from Sigma-Aldrich. Ammonium molybdate was purchased from Alfa Aesar. Ammonium hydroxide was purchased from J.T. Baker. Ammonium sulfate was purchased from VWR. The pH of the solutions were measured using pHydrion vivid 1-11® pH paper. Water was distilled above 3.0MΩ in-house using a Barnstead Model 525 Biopure Distilled Water Center.

3.2.1   Synthesis of $(NH_4)_{42}[\{(Mo^{VI})Mo^{VI}_5O_{21}(H_2O)_6\}_{12}\{Mo^V_2O_4(CH_3COO)\}_{30}]\cdot$ $\approx 300\ H_2O \cdot \approx 10\ CH_3COONH_4$ (Mo-132a)

Prepared according to the literature[34-38]:

64

See Chapter 2 Experimental Section 2.2 for further details.

3.2.2 Synthesis of $(NH_4)_{72}[\{(Mo^{VI})Mo^{VI}_5O_{21}(H_2O)_6\}_{12}\{Mo^V_2O_4(SO_4)\}_{30}] \cdot \approx 200\ H_2O$ (Mo-132b)

Prepared according to the literature[37]:

See Chapter 2 Experimental Section 2.2 for further details.

3.2.3 Synthesis of N,N,N-trimethyl(11-mercaptoundecyl)ammonium chloride (TMA) Functionalized Gold Nanoparticles (1.6 nm core)

Triphenylphosphine stabilized gold nanoparticles were synthesized according to the literature.[39] Briefly, $HAuCl_4$ $4 \cdot H_2O$ (0.101g) and tetra-n-octylammonium bromide (0.159g, TOAB) was added to a 5mL:6.5mL solution (toluene:water, degassed Ar). After the organic layer turned orange, triphenylphosphine (0.232g) was added where the biphasic solution turned cloudy white. After at least 10 minutes, $NaBH_4$ (0.146g, 10mL water) was rapidly added and the resulting dark brown solution was stirred for 3 hours. The solution was then washed with hexanes, saturated sodium nitrite, and 2:3 methanol:water solution to yield solid black $Au_{101}(PPh_3)_{21}Cl_5$.

After purification, $Au_{101}(PPh_3)_{21}Cl_5$ (2mL, dichloromethane) was mixed with TMA (100μL, 5mM) in an EtOH solution for 3 hrs. A bi-phasic solution was obtained by adding 2 mL of ultra-pure water with ~ 2.0 mg of TMA (undissolved) to the stirring solution and left overnight. The clear dichloromethane layer was extracted and the aqueous layer was washed with (2 x 3 mL) dichloromethane to remove any excess ligand or unreacted $Au_{101}(PPh_3)_{21}Cl_5$.

3.2.4 Synthesis of N,N,N-trimethyl(11-mercaptoundecyl)ammonium chloride (TMA) Functionalized Gold Nanoparticles (8.6 nm core)

In a typical synthesis, citrate stabilized gold nanoparticles were prepared according to Maye.[40] Briefly, $HAuCl_4$ (19.7 mg, 1.0 mmol) in H_2O (50 mL) was slowly heated to 97 °C. A 10 mL aqueous solution of trisodium citrate (111.8 mg, 38 mM) was added to the warm $HAuCl_4$ solution, whereupon the solution changed from a yellow hue to a ruby red color within 5-10 minutes. After the color change, the solution was removed from heat and left to stir overnight (~16 hrs).

To prepare TMA-capped Au, TMA (2.6 mg, 0.009 mmol) was first dissolved in 2 mL of ethanol. Aliquots of the TMA solution (5μL) were added to 2 mL of Citrate-capped Au (10 min.) until the ζ-pot. stabilized at $\zeta = 32.2 \pm 2.1$ mV to confirm complete transfer of the thiolate ligand. TEM indicated the formation of citrate-capped Au ($d = 8.6 \pm 0.7$ nm).

3.3 Instrumental

3.3.1 Zeta-potential Measurements (ζ-Pot)

The effective surface charge of varying [Mo-132(a,b)]:[Au] solutions were measured on the Malvern Zetasizer ZS in zeta analysis mode with a ζ-potential range of -200 to +200 mV in a folded capillary cell operating at an effective voltage of 150 mV. Data were obtained using the Smoluchowski theory.

3.3.2 Dynamic Light Scattering (DLS)

The size of individual solutions of varying ratio of [Mo-132(a,b)]:[Au] were performed on the Malvern Zetasizer ZS utilizing a 173° backscattering detector. Individual solutions

varying in the ratio of [Mo-132a]:[Au] ranged from 0 to the corresponding precipitation point were studied.

3.3.3   UV-visible Spectroscopy (UV-vis)

Optical properties and stability of gold nanoparticle solutions were evaluated in pure water solutions using UV-vis spectroscopy (Varian Cary 50 spectrophotometer) in the wavelength range of 300 to 800 nm with a scan rate of 3000 nm/min. In a typical experiment with Mo-132(a,b), solutions from ζ-potential experiments were placed in 1.0 mL glass cuvettes.

3.3.4   Transmission Electron Microscopy (TEM)

TEM measurements were performed on a JEOL 2000EX instrument operated at 90 kV with a tungsten filament (SUNY-ESF, N.C. Brown Center for Ultrastructure Studies). Particle sizes were analyzed manually with statistical analysis performed using ImageJ software on populations of at least 200 counts.

3.3.5   Thermogravimetric Analysis (TGA)

TGA experiments were performed on a Perkin Elmer Pyris1 TGA with a thermal analysis gas station and under O_2 purge with a heating rate of 10 ^{o}C/min. The samples were drop cast as neat solutions or powders and dried thoroughly before analysis.

3.4   Results and Discussion

This section describes the synthesis and characterization of gold nanoparticles capped with N,N,N-trimethyl(11-mercaptoundecyl)ammonium chloride (AuTMA) with core diameters of ca. 1.6 and 8.6 nm. We then describe how the change in core diameter in comparison to our results in Chapter 2 influences the electrostatic assembly mediated with Mo-132 clusters. **Scheme 3.1** shows an idealized view of the electrostatic assembly between AuTMA of core

diameters ca. 1.6, 4.4, or 8.6 mediated with the negatively charged Mo-132 clusters to form the

binary AuTMA+Mo-132 aggregates. (For characterization and synthesis of gold nanoparticles of

4.4 ± 0.7 nm ca. diameter please refer to Chapter 2. Characterization of the resulting positively

charged gold nanoparticles via transmission electron microscopy (TEM), and Thermal

Gravimetric Analysis (TGA) is illustrated in **Figure 3.4**.)
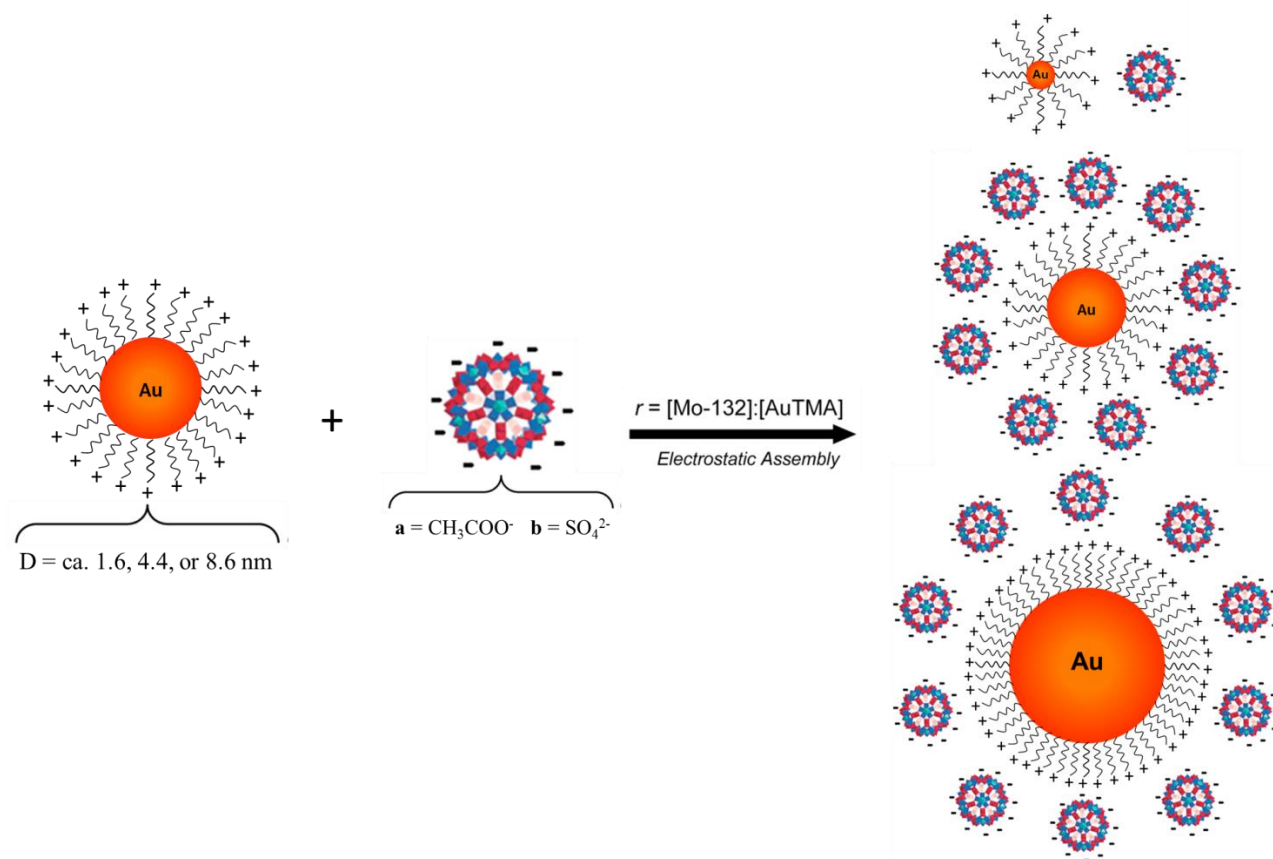
Scheme 3.1: An idealized representation of the electrostatic assembly between positively charged AuTMA of diameter 1.6, 4.4, and 8.6 nm and negatively charged Mo-132 analogues (a-b), forming Au-Mo-132(a-b) aggregates whose assemblies are tailored by molar ratios (*r*).

3.4.1 Synthesis and Characterization of 1.6 and 8.6 nm AuTMA

Gold nanoparticles coated with triphenylphosphine (PPh_3) were modified with TMA via ligand exchange which resulted in nanoparticles with diameters of ca. 1.6 nm.[39, 41] The resulting positively charged 1.6 nm AuTMA nanoparticles were characterized through TGA and Ultra-violet visible spectroscopy (UV-vis). It should be noted that low contrast due to fewer gold atoms in the nanoparticle core resulted in poor quality TEM analysis. Therefore, TEM analysis will not be provided for the characterization of 1.6 nm AuTMA.
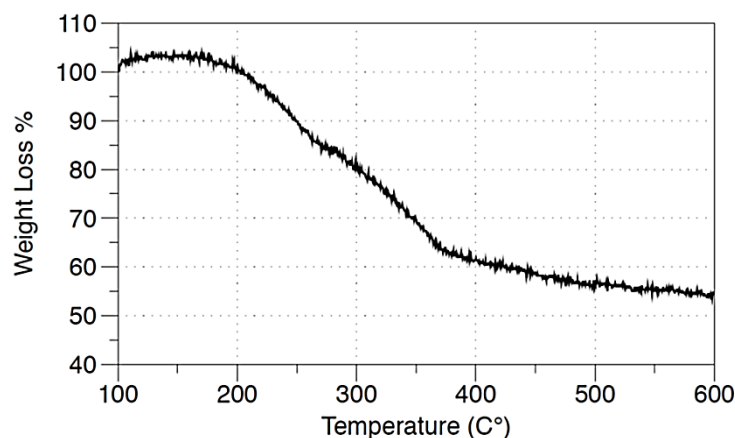
Figure 3.4: TGA analysis of 1.6 nm AuTMA showing a weight loss of 35.58%

TGA analysis was used to determine the mass loss associated with TMA ligands (**Figure 3.4**). We estimated the size, number of ligands, and composition of the gold nanoparticle to yield an approximate formula of $Au_{101}TMA_{38}Cl_{38}$. These results are consistent with the literature formulation of $Au_{101}(PPh_3)_{21}Cl_5$ from Hutchinson *et. al.* for an AuNP of similar dimensions.[39, 40]

Gold nanoparticles of diameter 8.6 nm were synthesized using a modified Turkevich method with a trisodium citrate capping ligand, then modified with TMA via ligand exchange.

The resulting positively charged 8.6 nm AuNPs were observed via transmission electron microscopy (TEM), shown in **Figure 3.5**.
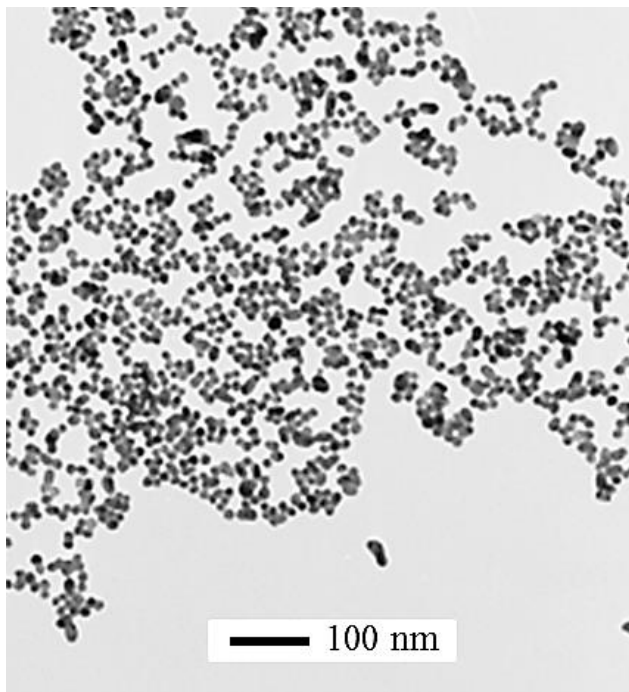
Figure 3.5: TEM image of 8.6 ± 0.7 nm AuTMA.

UV-vis spectroscopy was used to observe the surface plasmon resonance of both 1.6 nm and 8.6 nm AuNPs **(Figure 3.6)**. In plasmonic nanomaterials (i.e. gold, silver, composites, etc.) there exists a size dependent property in which electromagnetic fields arise at nanoparticle surfaces called surface plasmon resonance (SPR).[42] The SPR of noble metal nanoparticles is (1) experimentally measured using extinction spectroscopy (i.e. scattered and absorbed light);[42] (2) dependent on the distance matter is from the nanoparticle surface;[43] (3) theoretically predicted using Mie theory;[44] and (4) dictated by nanoparticle composition, shape, size, and local environment surrounding the core nanomaterial.[44-46]
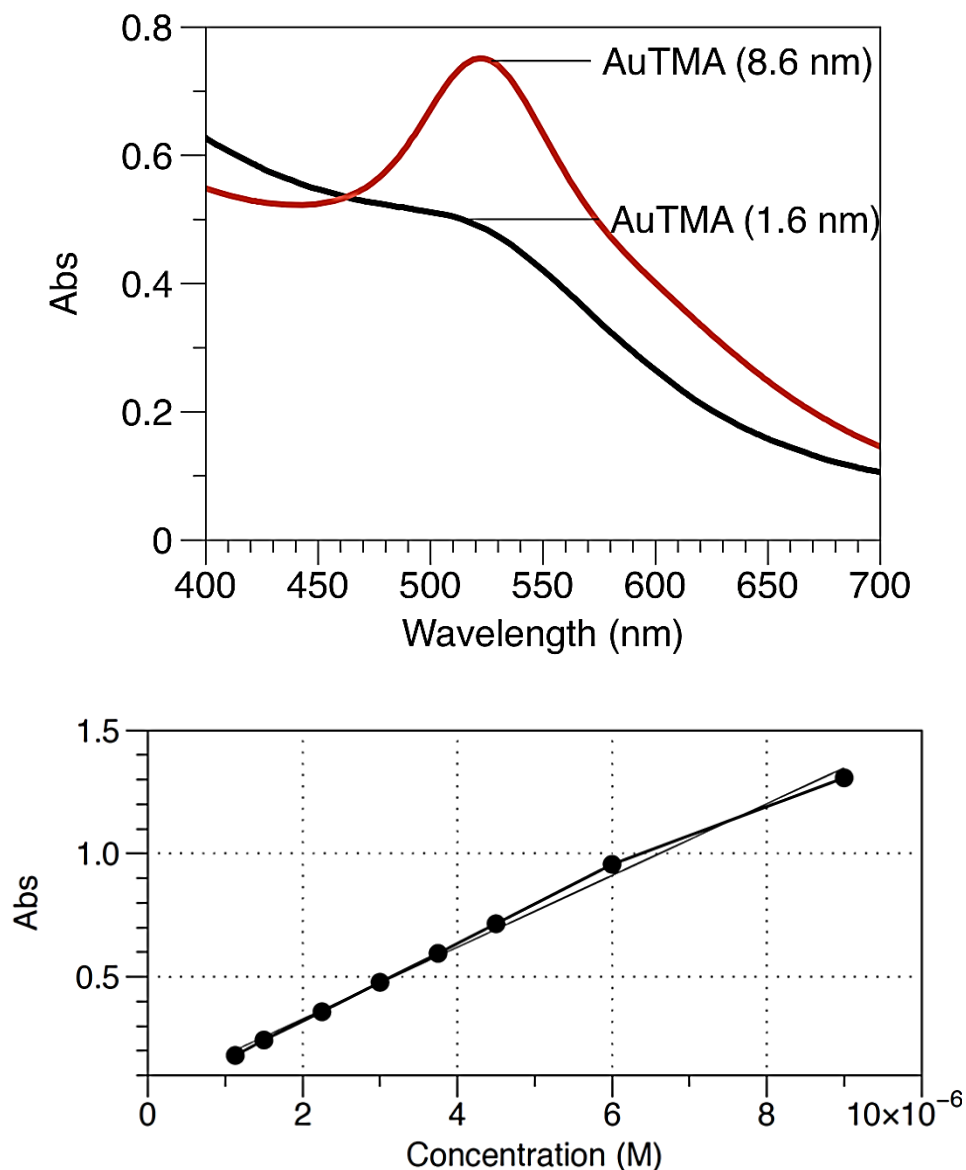
Figure 3.6: (a) Absorbance spectra of Au core sizes 1.5 and 8.6 nm. A comparison to the previously analyzed 4.4 nm Au shows a red-shift of the 8.6 nm Au that is characteristic of a larger core diameter as well as a dampening effect of the SPR band for cores smaller than 2.0 nm. **(b)** Linear plot of absorbance and concentration of 1.6 nm AuTMA to yield $\varepsilon = 1.45 \times 10^5$ M^{-1}cm^{-1}.

As it can be seen the characteristic SPR peak near 520 nm is present for 8.6 nm AuTMA. However for 1.6 nm AuTMA this characteristic SPR peak is not observed. Since the SPR peak is dependent on the size of gold nanoparticles, a decrease in the SPR peak is observed. The SPR

71

peak weakens and becomes less pronounced due to the damping effect such that the smaller sized nanoparticles yield smaller amounts of electron density of the gold core.[32, 47, 48] Concentrations of gold nanoparticles with diameters < 2.0 nm can be difficult to determine because of the absence of the SP band at ~ 520 nm. **(Figure 3.6(a))**[48, 49] In addition to concentration, the molar absorptivity (ε) needs to be determined for the gold nanoparticles for future characterization. The molar absorptivity **(Figure 3.6(b))** determined by plotting the maximum absorbance at 520 nm of varying dilutions against the concentrations was determined to be $\varepsilon = 1.45 \times 10^5$ M^{-1}cm^{-1}. With characterization of 1.6 nm AuTMA and 8.6 nm AuTMA complete, self-assembly was then studied.

3.4.2 Van der Waals Attraction in AuTMA+ Mo-132 systems

It is well known in colloid science that nanoparticles have a tendency to aggregate and form larger frameworks, superlattices, and superstructures. The driving force behind the formation of these structures is van der Waals attraction which is derived from the Derjarguin approximation. For two spherical nanomaterials of radii a_1 and a_2, the van der Waals attraction can be defined as:[50-52]

$$V_{vdW} = -\frac{A}{6}\left[\frac{2a_1 a_2}{R^2-(a_1+a_2)^2} + \frac{2a_1 a_2}{R^2-(a_1-a_2)^2} + ln(\frac{R^2-(a_1+a_2)^2}{R^2-(a_1-a_2)^2})\right] \text{ Eq. 1}$$

where R is the internuclear separation distance between the two nanomaterials, and A is the Hamaker constant. The van der Waals attraction force differs when gold nanoparticles of varying core diameter interact with Mo-132 **(Figure 3.7)**.
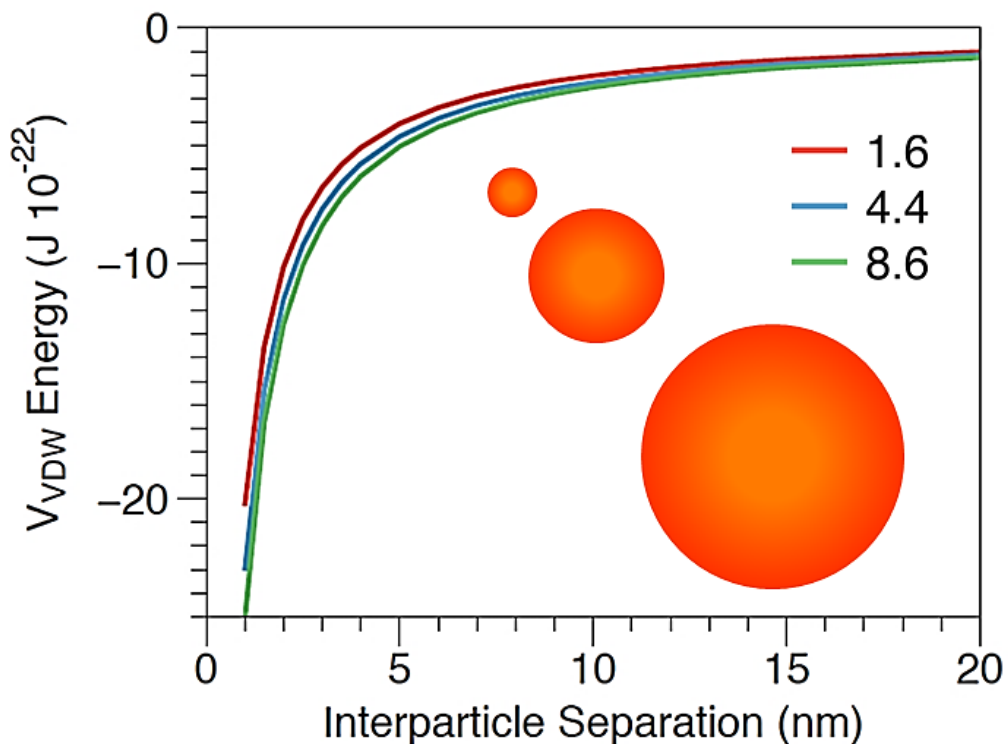
Figure 3.7: Calculated van der Waals attraction potentials for gold nanoparticles of 1.6, 4.4, and 8.6 nm core diameters with Mo-132.

Figure 3.7 represents the van der Waals attraction potentials for gold nanoparticles of 1.6, 4.4, and 8.6 nm diameters with Mo-132. The gold Hamaker constant (A_{Au-Au}) from the literature varies from $1 - 4 \cdot 10^{-19}$ J; therefore the average of $A_{Au-Au} = 2.5 \cdot 10^{-19}$ J was used.[53, 54] To the author's knowledge, no previous literature prior to this work documented a Hamaker constant of either Mo-132, Mo-154, or MoO_3. Therefore the Hamaker constant for WO_3 from the literature was used, with $A_{W-O} = 2.1 \cdot 10^{-20}$ J.[54] Since Hamaker constants of metal oxides are in the range of $1-3 \cdot 10^{-20}$ J, this value was judged adequate for Mo-132 and Mo-154.

$$A = \sqrt{(A_{Au} \cdot A_{Mo})^2} \quad \text{Eq. 2}$$

These approximations led to several observations where: (1) van der Waals attraction increases as gold nanoparticle diameters increase. (2) Since the origin of the van der Waals forces lies in the instantaneous dipole generated by the fluctuation of electron cloud surrounding the nucleus of electrically neutral atoms, the relatively small sized Mo-132 (~2.9 nm) is expected to have weaker van der Waals forces. (3) The larger Hamaker value of the more dense gold nanoparticles yield stronger van der Waals forces which are expected to predominant in the electrostatic assembly of AuTMA and Mo-132. For the purposes of crystallization, larger gold nanoparticles with stronger van der Waals forces may lead to faster kinetics and unorganized assembly.

3.3.3   Self-Assembly Investigation of 1.6 nm and 8.6 nm AuTMA

In Chapter 2, we observed a r_{E0} of ~10 for the self-assembly of Mo-132a and ~14 Mo-132b. We note here that the larger r_{E0} for Mo-132b was ascribed to increased concentration of counter-ions surrounding both the 4.4 nm AuTMA and Mo-132 nanomaterials. We looked to investigate the electrostatic interactions through a size regime of gold nanoparticles to further understand how these nanomaterials assemble. First, a comparison must be made by analyzing the equivalence point ratio, [Mo-132]:[Au], between 1.6 nm, 4.4 nm, and 8.6 nm AuTMA with the acetate and sulfate derivatives of Mo-132 clusters (Q = -42 and -72, respectively). These studies will aid in understanding the screening effects that we observed in our previous work. We first take a look at the larger 8.6 nm AuTMA nanoparticle.
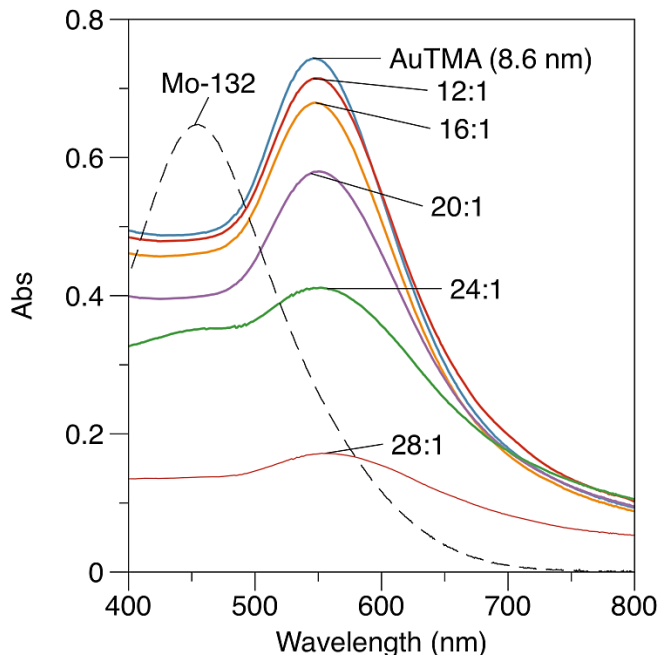
Figure 3.8: Representative UV-vis spectra of Mo-132a, 8.6 nm AuTMA, and AuTMA+Mo-132a assemblies at r = [Mo-132a]:[Au] = 12:1, 16:1, 20:1, 24:1, 28:1.

To begin, the self-assembly between Mo-132(a-b) and 8.6 nm AuTMA was induced by adding aliquots of Mo-132(a-b) ([Mo] = 25 μM) to a solution of AuTMA ([Au] = 0.6 μM) at increasing molar ratios, r = [Mo-132]:[Au] = 0 to 28. **Figure 3.8** shows the optical absorption characteristics of Mo-132a, 8.6 nm AuTMA, and the Mo-132a+AuTMA electrostatic assemblies. Upon initial addition of Mo-132(a-b), a colorimetric transition from red to pale red was observed along with an increase in absorbance. At r >20, a decrease in absorbance along with a red-shift is observed due to AuTMA+Mo-132a cluster formation. The spontaneous precipitation of the AuTMA -Mo-132 aggregates occurs at r =28. This observation was further studied with ζ-Pot. analysis for both Mo-132(a-b) clusters.
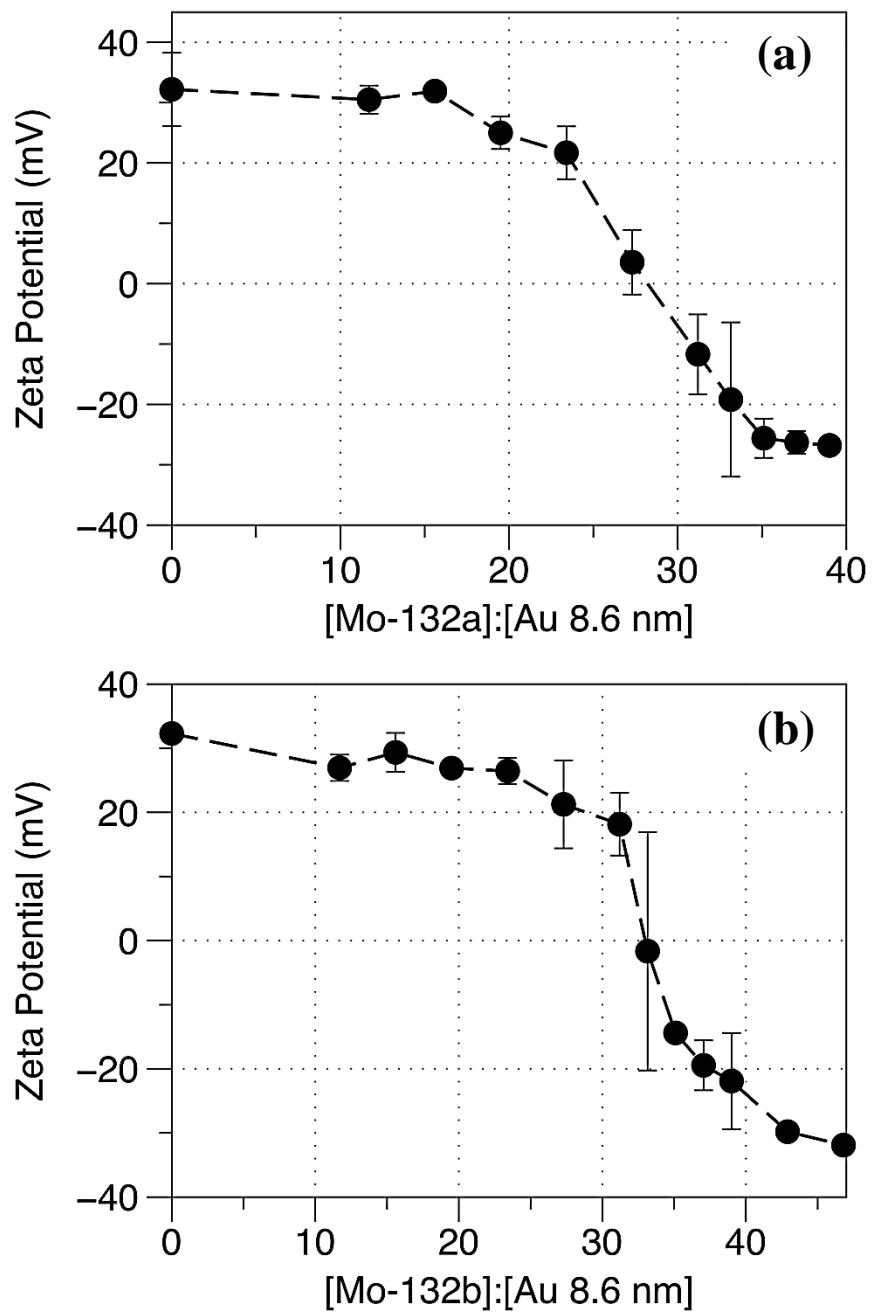
Figure 3.9: Zeta potential (ζ-pot.) measurements for **(a)** Mo-132a and **(b)** Mo-132b mediated assembly of 8.6 nm AuTMA at increasing r = [Mo-132]:[Au].

Figure 3.9(a) shows a representative set of ζ-Pot measurements for the Mo-132a + AuTMA system at increasing r. The initial 8.6 nm AuTMA particle has a charge of $\zeta = 32.2 \pm 2.1$ mV, which decreases slowly in the range $r = 0$ to 25, which is indicative of the Mo-132a interacting with and screening the AuTMA charge. At $r > 25$ a sharp decrease in ζ is detected, with neutralization ($\zeta \approx 0$ mV) occurring at $r \approx 28$. At $r > 28$ there is a negative overall charge ($\zeta \approx -28$ mV) which remains relatively invariant, due to both the presence of excess Mo-132a, as well as the likelihood that each assembled aggregate is terminated by it. In **Figure 3.9(b)**, a representative set of ζ-Pot measurements for the Mo-132b + AuTMA system is shown. At increasing r, a slow decrease is observed in the range $r = 0$ to 30. At $r > 30$ a sharp decrease in ζ is detected, with a neutralization ($\zeta \approx 0$ mV) occurring at $r \approx 33$. At $r > 33$ there is a negative overall charge $\zeta \approx -32$ mV.

The larger 8.6 nm AuNP produced an analogous counterintuitive effect as previously observed for 4.4 nm Au, where Mo-132b provided a higher equivalence point r_{E0} at ~33 compared to ~28 for Mo-132a. In a similar fashion to our previous studies with the 4.4 nm AuNP, we attribute our findings to the same effects, where the incoming nanomaterial must first encounter a double-layer, and then displace the surface counter-ions. These electrostatic changes at the interfaces of the particles influence the effective ζ-Pot being measured. For instance, as the particles come together, ion displacement of Cl^- anions from AuTMA with diameters of ca. 4.4 or 8.6 and NH_4^+ cations from Mo-132a-b must occur for the charges to become visible to one another. The ion displacement is related to charge change, ion charge, and ionic strength. Thus Mo-132b, with an internal charge of -72, is regulated by a higher concentration of NH_4^+ counter-ions than Mo-132a, internal charge is -42, resulting in stronger coulombic attraction. This in turn lessens the attraction for AuTMA, and decreases kinetics, resulting in the higher equivalence

77

point. This theory was supported by **Figure 2.7**, in which an increase in ionic strength resulted in a higher r_{E0}.

To justify our findings, 1.6 nm AuNPs were next investigated to observe whether our counter intuitive results would remain in effect for nanoparticles that were more similar in size to Mo-132 clusters.

To begin, the self-assembly between Mo-132(a-b) and 1.6 nm AuTMA was induced by adding aliquots of Mo-132(a-b) ([Mo] = 300 μM) to a solution of AuTMA ([Au] = 47.5 μM) at increasing molar ratios, r = [Mo-132]:[Au] = 0.1 to 5. **Figure 3.10(a)** shows the optical absorption characteristics of Mo-132a, AuTMA, and the Mo-132a+AuTMA electrostatic assemblies. At r >0.6, a decrease is observed due to the presence of relatively small AuTMA+Mo-132a clusters, followed by the growth of a large aggregate. **Figure 3.10(b)** shows the optical absorption characteristics of Mo-132b, AuTMA, and the Mo-132b+AuTMA electrostatic assemblies. Upon initial addition of Mo-132(a-b), a colorimetric transition from pale brown to dark brown was observed along with an increase in absorbance. This increase upon the addition of Mo-132(a-b) in solution is likely due to the SPR overlap and similar extinction coefficients (ε = 1.45×10^5 $M^{-1}cm^{-1}$ and 1.85×10^5 $M^{-1}cm^{-1}$ for AuTMA and Mo-132, respectively). Since the SPR band for AuTMA is dampened, the Mo-132 may play more of a role in the UV-vis spectra. This is evident by the flattening of the band at the wavelength (λ) 455 nm, assigned to Mo-132. At r >0.4, a decrease in absorbance is observed due to AuTMA+Mo-132b cluster formation. The spontaneous precipitation of the AuTMA -Mo-132 aggregates occurs at r =0.6 to 1. This observation was then investigated by ζ-Pot. analysis.
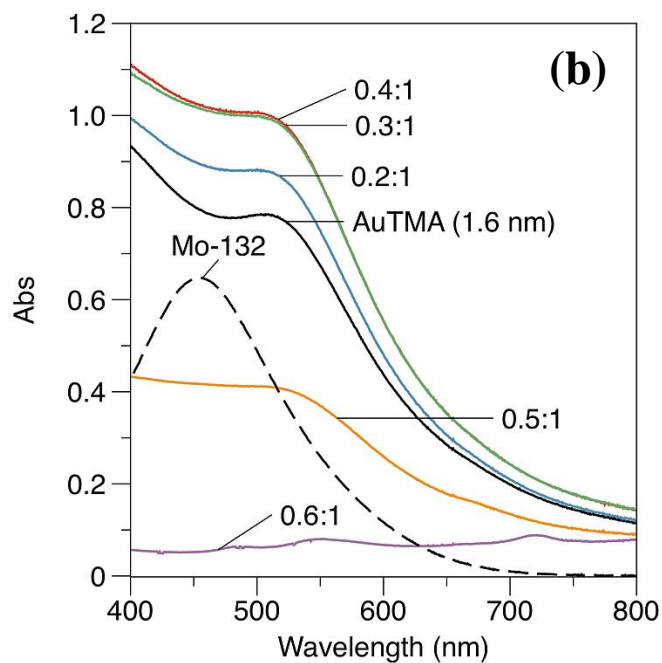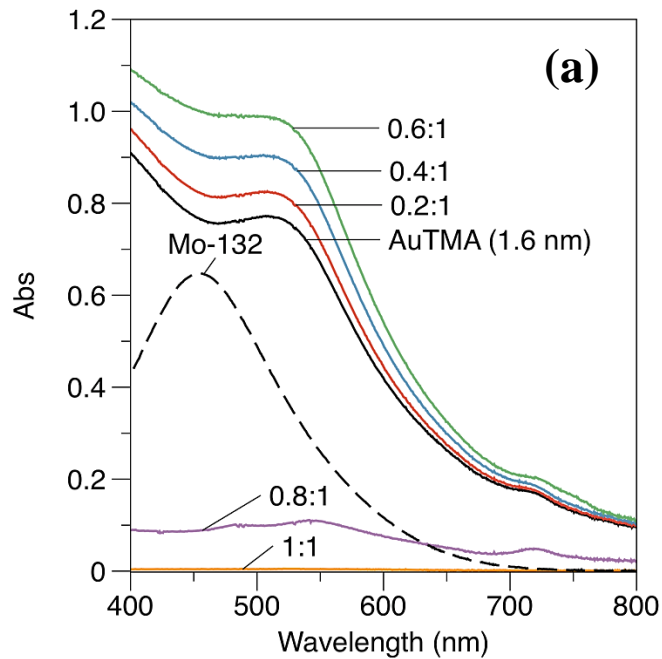
Figure 3.10: Representative UV-vis spectra of **(a)** Mo-132a, 1.6 nm AuTMA, and AuTMA+Mo-132a assemblies at r = [Mo-132a]:[Au] = 0.2:1, 0.4:1, 0.6:1, 0.8:1, 1:1. **(b)** Mo-132b, 1.6 nm AuTMA, and AuTMA+Mo-132b assemblies at r = [Mo-132b]:[Au] = 0.2:1, 0.3:1, 0.4:1, 0.5:1, 0.6:1.
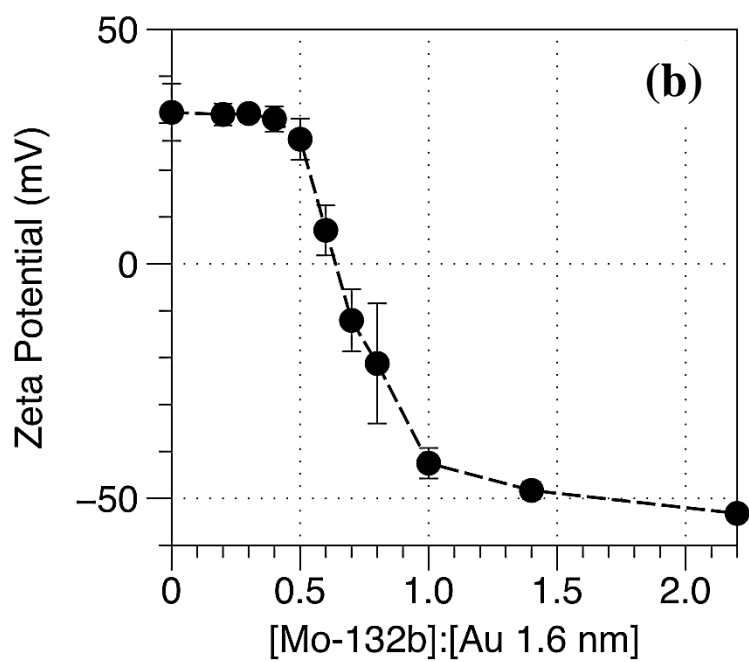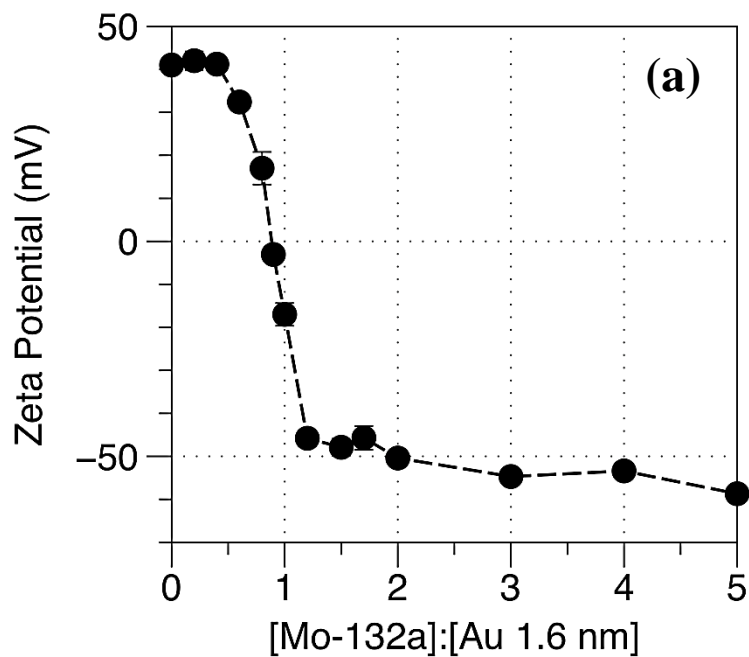
Figure 3.11: Zeta potential (ζ-pot.) measurements for **(a)** Mo-132a and **(b)** Mo-132b mediated assembly of AuTMA at increasing r = [Mo-132]:[Au].

Figure 3.11(a) shows a representative set of ζ-Pot measurements for the Mo-132a + AuTMA system at increasing r. The initial AuTMA particle has a charge of $\zeta = 40.3 \pm$ mV, which decreases slowly at $r = 0$ to 0.5, which is indicative of the Mo-132a interacting with and screening the AuTMA charge. At $r > 0.5$ a sharp decrease in ζ is detected, with neutralization ($\zeta \approx 0$ mV) occurring at $r \approx 1.0$. At $r > 1.0$ there is a negative overall charge ($\zeta \approx$ -50 mV) which remains relatively invariant, due to both the presence of excess Mo-132a, as well as the likelihood that each assembled aggregate is terminated by the molybdate cluster. In **Figure 3.11(b)**, the initial 1.6 nm AuTMA particle has a charge of $\zeta = 40.3 \pm$ mV, which has a subtle decrease between $r = 0$ to 0.5. At $r > 0.5$ a sharp decrease in ζ is detected, with neutralization ($\zeta \approx 0$ mV) occurring at $r \approx 0.6$. At $r > 0.6$ there is a negative overall charge ($\zeta \approx$ -50 mV) which remains relatively invariant, due to both the presence of excess Mo-132b, as well as the termination of each assembled aggregate is terminated by it. These trends toward electroneutrality correspond closely with the bulk precipitation observed via UV-vis **(Figure 3.10)**.

For example, **Figure 3.12** shows a plot of the SPR absorbance maxima (520 nm), measured in parallel to ζ-Pot measurements. For the assembly with Mo-132a, a drop in absorbance is detected at $r = 0.8$, correlating with the aggregation. The same effect can be observed at $r = 0.5$ for Mo-132b.
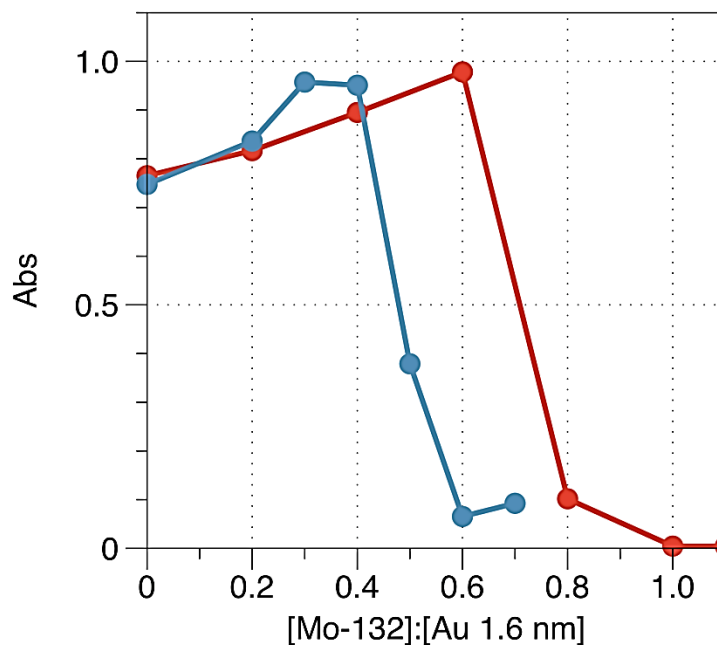
Figure 3.12: The corresponding plot of AuTMA with Mo-132(a-b) at absorbance maxima (520 nm) decreases with increasing *r*.

In comparison with both 4.4 and 8.6 nm AuTMA, we observe an intuitive effect of the higher anionic charged Mo-132b having a lower r_{E0} at the point of electroneutrality of ~0.6 compared to ~1.0 for Mo-132a. This reversal can be supported by the higher anionic charge of -72 for Mo-132b generating a stronger coulombic attraction with the smaller 1.6 nm AuTMA. It can be suggested that these results can be rationalized by several factors. First, the smaller diameter of the 1.6 nm Au allows for better size compatibility to Mo-132 (~2.9 nm) than that of 4.4 and 8.6 AuNPs. This allows for more of an "ion-ion" interaction compared to Mo-132 acting more as a surfactant for the larger 4.4 nm AuNPs. It also can be suggested that the composition of 4.4 nm Au yields a higher concentration of Cl⁻ counter-ions with approximately a 20 fold increase when comparing $Au_{3100}TMA_{760}Cl_{760}$ to $Au_{101}TMA_{38}$.

Another influence can be attributed to the deflection angle of between ligands on a particle surface **(Figure 3.3)**. A simple approximation can be calculated by:[26, 55]

$$R = \sqrt{\frac{0.0324 \, nm^2}{\pi}} = 0.102 \, nm^2 \quad \textbf{(Eq. 1)}$$

where R is the radius approximation of the surface area that one TMA ligand takes up on the nanoparticle surface. $0.102 \, nm^2$ is the area per Me_3N^+ molecule on the gold nanoparticle surface.

$$Deflection \; angle \; (\theta) = \left[\frac{2R}{r}\right] \cdot \frac{180}{\pi} \quad \textbf{(Eq. 2)}$$

Using Eq. 1, the deflection angle between TMA ligands can be approximated using Eq. 2, where r is the gold nanoparticle radius. To simplify calculations, the approximation assumes that R remains the same throughout the range of nanoparticle sizes, the numbers of smaller or larger AuNPs were equal, a uniform distribution of Me_3N^+ across the AuNP surface, and complete ligand coverage on the gold nanoparticle surface.[16]

Table 3.1: As the gold diameter decreases the deflection angle between two TMA ligands on AuTMA of diameter ca. 1.6, 4.4, or 8.6 increases.

Gold Diameter (nm)	Deflection Angle ($\theta°$)
1.6	14.6
4.4	5.3
8.6	2.7

For particles of size 1.6 nm, 4.4 nm, and 8.6 nm we have approximated deflections angles of 14.6°, 5.3°, and 2.7°, respectively. The increase in angle as the gold nanoparticle diameter

decreases allows for TMA head groups to be further apart which in turn decreases their repulsive forces. This results in weaker coulombic forces requiring fewer Cl⁻ counter-ions to counterbalance this effect. This decrease in counter-ions allows for lower counter-ion screening between Mo-132 and the 1.6 nm Au in turn allowing the anionic Mo-132 to interact with the Me_3N^+ head groups more readily and favoring the higher charged Mo-132b.

3.5   Conclusions

A great deal has been learned about the self-assembly of these nanomaterials that may bring us closer to our aim of achieving crystallization. In solutions of gold nanoparticles of opposite charge two key parameters control the crystallization process. (1) The charge on both entities must be of equal magnitude ($Q^+ = Q^-$) and (2) The size of both entities must be approximately equivalent.[20] In this chapter, we observed a r_{E0} of ≈ 1.0 for the 1.6 nm AuTMA+ Mo-132a system, suggesting that one of these key parameters has been realized. Since amorphous aggregates still occurred for this system, size equivalence should also be considered. When discussing size equivalence, one must not only take into account the core diameter, but include the TMA ligands (~1.9 nm). When these are taken into account, the diameters of 1.6, 4.4, and 8.6 nm AuNPs grow to ca. 5.4, 8.2, and, 12.4 nm, respectively. These observations are relevant for the pursuit of crystalline composites, and the next step in these studies is to synthesize a gold nanoparticle of ~3.0 nm dimensions when the ligand length is included. Future work will incorporate both parameters and may possibly lead to a novel superlattice structure.

3.5   References

[1]   A.K. Suresh, Metallic *Introduction to Nanocrystallites, properties, Synthesis, Characterization and Potential Applications in Molecular Science* **2012**, The Authors, Springer, pp1-23.

[2]   S.D. Perrault W.C.W. Chan *J. Am. Chem. Soc.* **2009**, 131, 47, 17042–17043.

[3]   F. Schulz, T. Homolka, N.G. Bastús, V. Puntes, H. Weller, T. Vossmeyer, *Langmuir*. **2014**, 30, 10779-10784.

[4]   C.C. Yang, Y-W. Mai, *J. Phys. Chem C.* **2013**, 117, 2421-2426.

[5]   C. Burda; X. Chen; R. Narayanan; M.A. El-Sayed, *Chem. Rev.* **2005**, 105, 1025-1102.

[6]   K. Saha, S.S. Agasti, C. Kim, X. Li, V.M. Rotello, *Chem. Rev.* **2012**, 112, 2739-2779.

[7]   B. Pelaz, S. Jaber, D. J. de Aberasturi, V. Wulf, T. Aida, J. M. de la Fuente, J. Feldmann, H.E. Gaub, L. Josephson, C. R. Kagan, N. A. Kotov, L.M. Liz-Marzán, H. Mattoussi, P. Mulvaney, C. B. Murray, A. L. Rogach, P.S. Weiss, I. Willner, W.J. Parak, *ASC Nano.* **2012**, 6, 10, 8468-8483.

[8]   D. Yanover, R. Vaxenburg, J. Tilchin, A. Rubin-Brusilovski, G. Zaiats, R.K. Capek, A. Sashcuiuk, E. Lifshitz, *J. Phys. Chem. C.* **2014**, 118, 17001-17009.

[9]   X. Ye, C. Zheng, J. Chen, Y. Gao, C.B. Murray, *Nano Lett.* **2013**, 13, 765-771.

[10]   E.V. Shevchenko, D.V. Talapin, N.A. Kotov, S. O'Brien, C.B. Murray, *Nature*. **2006**, 439, 5, 55-59.

[11]   J.J. Urban, D.V. Talapin, E.V. Shevchenko, C.R. Kagan, C.B. Murray, *Nature Materials.* **2007**, 6, 115-121.

[12]   J.N. Anker, W.P. Hall, O. Lyandres, N.C. Shah, J. Zhao, R.P. Van Duyne, *Nature Materials*. **2008,** 7, 442-453.

[13]   R.J. Macfarlane, B. Lee, M.R. Jones, N. Harris, G.C. Schatz, C.A. Mirkin, *Science.* **2011,** 14, 334, 204-208.

[14]   M. Sastry, M. Rao, K.N. Ganesh, *Acc. Chem. Res.* **2002,** 35, 847-855.

[15]   Q. Yao, Z. Luo, X. Yuan, Y. Yu, C. Zhang, J. Xie, J.Y. Lee, *Scientific Reports.* **2014,** 4, Article # 3848 1-8.

[16]   M.J. Polking, J.J. Urban, D.J. Milliron, H. Zheng, E. Chan, M.A. Caldwell, S. Raoux, C.F. Kisielowski, J.W. Ager, III, R. Ramesh, A.P. Alivisatos, *Nano Letters*. **2011,** 11, 1142-1152.

[17]   Z. Wei, Y. Qiu, H. Chen, K. Yan, Z. Zhu, Q. Kuang, S. Yang, *J. Mater. Chem. A*. **2014,** 2, 5508-5515.

[18]   R.D. Cadena-Nava, M. Comas-Gracia, R.F. Garmann, L.N. Rao, C.M. Knobler, W.M. Gelbart, *Journal of Virology*. **2011,** 3318-3326.

[19]   H-B. Yao, H-Y. Fang, X-H. Wang, S-H. Yu, *Chem. Soc. Rev.* **2011,** 40, 3764–3785.

[20]   Q. Zhang, J. Xie, J. Yang, J.Y. Lee, *ACS Nano*. **2009,** 3, 1, 139–148.

[21]   C-C. Huang, Z. Yang, K-H. Lee, H-T. Chang, *Angew. Chem. Int. Ed*. **2007,** 46, 6824 – 6828.

[22]   O.A. Balitskii, M. Sytnyk, J. Stangl, D. Primetzhofer, H. Groiss, W. Heiss, *ACS Appl. Mater. Interfaces*. **2014,** 6, 17770−17775.

[23]   L. Xu, W. Ma, L. Wang, C. Xu, H. Kuang, N.A. Kotov, *Chem. Soc. Rev.* **2013,** 42, 3114-3126.

[24]   K.E. Lee, J.E. Kim, U.N. Maiti, J. Lim, J.O. Hwang, J. Shim, J.J. Oh, T. Yun, S.O. Kim, *ACS Nano*. **2014,** 8, 9, 9073-9080.

[25]   T. Wang, D. LaMontagne, J. Lynch, J. Zhuang, Y.C. Cao, *Chem. Soc. Rev.* **2013,** 42 2804-2823.

[26]   M.A. Kostianinen, P. Hiekkataipale, A. Laiho, V. Lemieux, J. Seitsonen, J. Ruokolainen, P. Ceci, *Nature Nanotech.* **2013,** 8, 52-56.

[27]   B. Kowalczyk, A.M. Kaslin, R. Orlik, K.J.M. Bishop, A.Z. Patashinskii, A. Mitus, B.A. Grzybowski, *Chem. Eur. J.* **2009,** 15, 9, 2032-2035.

[28]   J. Gooch, A. Alan, S. Jones, C.R. Hine, R. Alam, S. Garai, M.M. Maye, A. Müller, J. Zubieta, *Journal of Colloid and Interface Science.* **2014,** 432, 144–150.

[29]   H.D. Hill, J.E. Millstone, M.J. Banholzer, C.A. Mirkin, *ACS NANO*, **2009**, 3, 2, 418-424.

[30]   W.D. Luedtke, U. Landman, *J. Phys. Chem.* **1996,** 100, 32, 13323-13329.

[31]   W.D. Luedtke, U. Landman, *J. Phys. Chem B* **1998,** 102, 6566-6572.

[32]   D.A. Walker, E.K. Leitsch, R.J. Nap, I. Szleifer, B.A. Grzybowski, *Nature Nanotechnology.* **2013,** 8, 676-681.

[33]   F. Schreiber, *Prog. Surf. Sci.* **2000**, 65, 151–256.

[34]   A. Müller, S.K. Das, E. Krickemeyer, C. Kuhlmann, *Inorg. Synth.* **2004,** 34, 191-200.

[35] L. Cronin, E. Diemann, A. Müller, Polyoxomolybdate Clusters: Nanoscopic Wheels and Balls in *Inorganic Experiments*, Woollins, J. D., ed., Wiley-VCH, Weinheim, **2003**, 340-346.

[36] A. Müller, E. Krickemeyer, H. Bögge, M. Schmidtmann, B. Botar, M.O. Talismanova, *Angew. Chem. Int. Ed.* **2003,** 42, 2085-2090.

[37] A. Müller, Y. Zhou, H. Bögge, M. Schmidtmann, T. Mitra, E.T.K. Haupt,A. Berkle, *Angew. Chem. Int. Ed.* **2006**, 45, 460-465.

[38] A. Müller, S.K. Das, S. Talismanov, S. Roy, E. Beckmann, H. Bögge, M. Schmidtmann, A. Merca, A. Berkle, L. Allouche, Y. Zhou, L. Zhang, *Angew. Chem. Int. Ed.* 42 (2003) 5039-5044.

[39] W.W. Weare, S.M. Reed, M.G. Warner, J.E. Hutchison, *J. Am. Chem. Soc.* **2000**, 122,12890-12891.

[40] M.M. Maye, D. Nykypanchuk, D. van der Lelie, O. Gang, *J. Am. Chem. Soc.,* **2006**, 128, 43, 14020-14021.

[41] G.H. Woehrle, L.O. Brown, J.E. Hutchison, *J. Am. Chem. Soc.* **2005**, 127, 2172-2183.

[42] G.H. Chan, J. Zhao, G.C. Schatz, R.P. Van Duyne, *J. Phys. Chem. C*, **2008,** 112, 36, 13958–13963.

[43] M.S. Golden, A.C. Bjonnes, R.M. Georgiadis, *The Journal of Physical Chemistry C* **2010**, 114, 19, 8837-8843.

[44] G. Mie; *Beiträge zur Optik trüber Medien, speziell kolloidaler Metallösungen*. Annalen der Physik 330, 3, **1908**, 377–445

[45] K.L. Kelly, E. Coronado, L. Zhao, G.C. Schatz, *Journal of Physical Chemistry B* **2003**, 107, 3, 668-677.

[46] M. M. Maye, J. Luo, I. S. Lim, L. Han, N. N. Kariuki, D. Rabinovich, T. Liu, C.J. Zhong, *J. Am. Chem. Soc*., **2003**, 125, 9906-9907.

[47] S.K. Ghosh; T. Pal; *Chem. Rev.* **2007**. 107, 11, 4797-4862.

[48] M.M. Maye, W.X. Zheng, F.L. Leibowitz, N.K. Ly, C.J. Zhong, *Langmuir*, **2000,** 16, 490-497.

[49] M.M. Maye, L. Han, N.N. Karinki, N.K. Ly, W. Chan, J. Luo, C. Zhong, *Analytica Chimica Acta,* **2003,** 17-27.

[50] K. Lee, A.N. Sathyagal, A.V. McCormick, *Colliods and Surfaces A Physicochemical and Engineering Aspects*, **1998**, 144, 115-125.

[51]   R.J. Hunter, Foundations of Colloid Science, 2nd Ed. **2001**, Oxford University Press, Oxford.

[52]   T. Doane, C. Burda, *Advanced Drug Delivery Reviews*. **2013**, 65, 607-621.

[53]   S. Biggs, M.K. Chow, C.F. Zukoski, F. Grieser, *J. Colloid Interface Sci.* **1993**, 160, 511.

[54]   K. Anderson, **2004**. *Aqueous Processing of WC-Co Powders*. Doctoral Dissertation.

[55]   A. Essaidi, M' B. Chakif, B. Schops, A. Aumman, S. Xiao, C. Esen, A. Ostendorf, *Journal of Laser Micro/Nanoengineering*, **2013**, 8, 2, 131-136.

[56]   Calculated using Advanced Chemistry Development (ACD/Labs) Software V11.02 (© 1994-2015 ACD/Labs)

Chapter 4

Electrostatic Assembly of Gold Nanoparticles Meditated by $(NH_4)_{28}[Mo_{154}(NO)_{14}O_{420}(OH)_{14}(H_2O)_{70}] \cdot 350\ H_2O$ (Mo-154)

4.1   Introduction

Today, nanotechnology focuses on the development of optical, electrical, and magnetic properties of nanomaterials with respect to their size, shape, and surface chemistry.[1-8] In terms of shape, non-spherical nanomaterials have only recently been a focus of interest the field. This observation may be due to two challenges: (1) non-spherical morphologies present difficulties in the understanding of solid state fundamentals and (2) the interfacial adsorption and reaction involved in crystal growth and mineralization are not well understood.[9] These considerations have been a cause of the limitations for expansion of novel nanomaterials. However, recent innovative approaches to particle syntheses have yielded nanowires[10], nanotubes[11], nanorods[12], nanocubes[13], and many other exotic structures[14-16], which have led to a remarkable variety of nano-sized building blocks of different shapes, compositions, patterns, and functionalities.

The geometry of these building blocks can lead to optical, electronic, magnetic and/or chemical anisotropy which has attracted attention to the role of shape in self-assembly.[3,6,8,17] This anisotropy likely leads to these nanomaterials interacting in completely different ways than their spherical counterparts.[2,18] For example, Fe_2O_3 superparamagnetic nanorods conjugated with anti-MAP antibodies were efficiently used as magnetic sensors for the detection of bacteria, where due to their magnetic and shape anisotropy, they were found to be superior to similar spherical nanoparticles.[18] The influence of shape of nanomaterials affects the geometry of their close-packing, the directionality of the interactions, the selectivity of the interactions, the connectivity between nanomaterials in their assembly, the attraction between the individual nanomaterials, and the dynamic aspects of their assembly.[19-21]

In terms of directionality, long range interactions such as electrostatic and magnetic interactions of non-spherical nanomaterials results in anisotropic electric and magnetic

90

polarizabilities, possibly exploiting directional interaction potentials.[17] For example, the curvature of a surface regulates the distribution of surface charge, affecting the strength of electrostatic forces between nanomaterials.[22-24]

Since shape affects numerous parameters, it will become an essential part in the understanding and use of self-assembly. Its interactions with matter, independent of scale, allows the investigation of multi-scale processes such as self-assembly. The nanoscale, affected by forces in both molecular and microscopic scales, provides a perfect scale to investigate shape interactions.[19] However, the nanoscale also provides challenges such as polydispersity that may hinder the development of a systematic understanding of these interactions.

The precise diameter of 3.5 nm and quantized 28 negative charge makes the ring-shaped $(NH_4)_{28}[Mo_{154}(NO)_{14}O_{448}H_{14}(H_2O)_{70}] \cdot 350 \ H_2O$ (Mo-154) an ideal candidate in the investigation of electrostatic self-assembly. Mo-154 is a strong electrolyte that completely dissociates in aqueous solution to give a nanoscopic cluster.[25-27] The intriguing feature of this compound is its ring shape that may offer a unique approach for analyzing the electrostatic interactions between this class of polyoxomolybdates and gold nanoparticles. This ring-shaped structure is comprised of 140 MoO_6 units and 14 pentagonal bipyramidal sites with a central cavity size in the nanometer range and a high surface area with the outer edges of the ring having a high electron density, which explains its high affinity for adsorbents.[25] This localized electron density leads to a polarizability which may influence the directionality of electrostatic interactions between Mo-154 and spherical gold nanoparticles.

The electrostatic attraction between the Mo-154 and gold nanoparticles brings a new dimension into the self-assembly of gold nanoparticles and polyoxomolybdates. Specfically, the

ring shape structure of Mo-154 leads to asymmetric factors such as electron density and connectivity that may affect the self-assembly. The higher electron density regions of the Mo-154 are located at the edges of the ring structure, whereas in Mo-132, a relatively equal distribution across the sphere is present. This permits attractive forces of equivalent strength to take place regardless of the orientation of the Mo-132. The orientation of the Mo-154 in the presence of the Au nanoparticle may have an effect on its attraction toward the nanoparticle.

Along with electron density, the connectivity of the Mo-154 with the Au nanoparticles may also play a crucial role in the precipitation point of the assembled aggregates. In **Scheme 4.1**, we see two possible ways that the Mo-154 could be attached to the Au nanoparticle. It is possible that the Mo-154 clusters all attach in the same orientation around the Au nanoparticle, however, it can also be suggested that there is a mixed orientation of the Mo-154 surrounding the nanoparticles and this may affect how the zeta potential is interpreted.
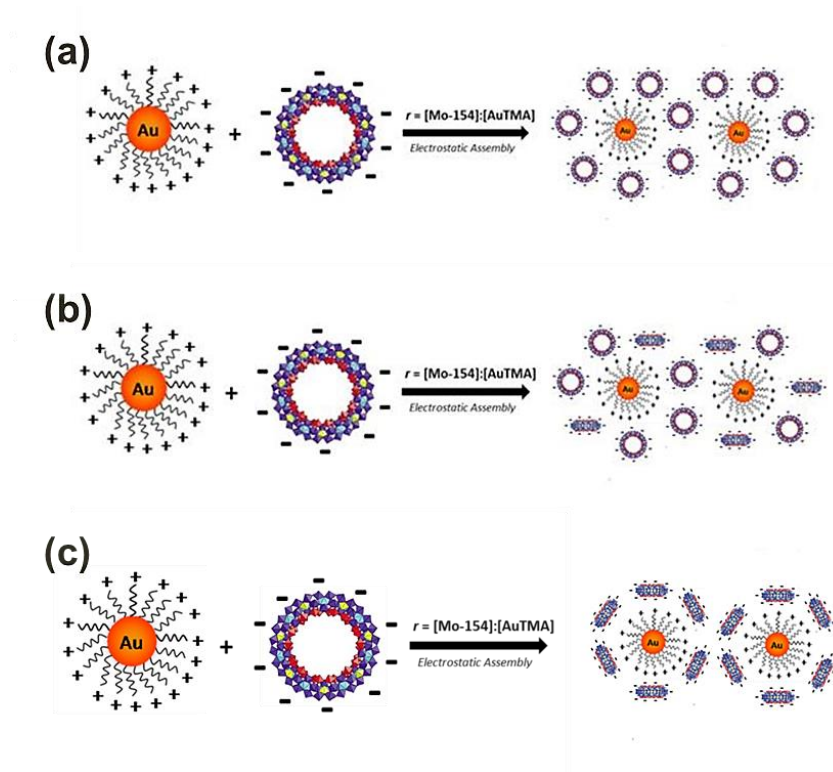
Scheme 4.1: An idealized representation of the electrostatic assembly between positively charged AuTMA and negatively charged Mo-154 forming Au-Mo-154 aggregates whose assemblies are tailored by molar ratios (*r*). (a) Attachment of the Mo-154 by the outer ring diameter to the AuTMA. (b) Mixed orientation of Mo-154 attachment to AuTMA, where attachment occurs by the outer ring diameter as well as the side surface of the ring structure. (c) Attchment occurs between AuTMA and the side surface of the ring structure of Mo-154.

We hypothesize that electrostatic assembly between the $(NH_4)_{28}[Mo_{154}(NO)_{14}O_{448}H_{14}(H_2O)_{70}]^{-28}$ clusters and AuTMA will be affected by shape which may directly play a role in the [Mo-154]:[Au] stoichiometry of tailored aggregation. A comparison between these results and results from Chapters 2 and 3 may enlighten our observations. First, gold cores of 1.6 and 4.4 nm diameter functionalized with N,N,N-trimethyl(11-mercaptoundecyl)ammonium chloride (TMA) self-assembled monolayers and $(NH_4)_{28}[Mo_{154}(NO)_{14}O_{448}H_{14}(H_2O)_{70}]$ clusters are synthesized. Then the tailored aggregations

dependent on the [Mo-154]:[AuTMA] stoichiometry are studied by dynamic light scattering (DLS), zeta-potential analysis (ζ-Pot), and absorption spectroscopy (UV-vis) of the Au TMA surface plasmon resonance band (SPR).

4.2   Experimental

All chemicals were used as obtained without further purification. Acetic acid, sulfuric acid, hydrochloric acid, ammonium acetate, sodium chloride, and sodium acetate, were all purchased from Fisher. Hydrazine sulfate, ammonium chloride, ethanol, triphenylphosphine, hydroxyl amine, diethyl ether, and gold (III) chloride trihydrate were all purchased from Sigma-Aldrich. Ammonium molybdate was purchased from Alfa Aesar. Ammonium hydroxide was purchased from J.T. Baker. Ammonium sulfate was purchased from VWR. The pH of the solutions were measured using pHydrion vivid 1-11® pH paper. Water was distilled above 3.0MΩ in-house using a Barnstead Model 525 Biopure Distilled Water Center.

4.2.1   Synthesis of $(NH_4)_{28}[Mo_{154}(NO)_{14}O_{448}H_{14}(H_2O)_{70}] \cdot 350 \ H_2O$ (Mo-154)

Prepared according to the literature[25]:

Water (200 mL), $Na_2MoO_4 \cdot 2 \ H_2O$ (7.46 g, 30.8 mmol), NH_4VO_3 (1.19 g, 10.2 mmol), $NH_2OH \cdot HCl$ (12.83 g, 184.6 mmol), and HCl (3.5% v/v, 9.5 mL) were added to a 500 mL Erlenmeyer flask The mixture was stirred for 2 minutes, then heated to 65°C in a 500 mL Erlenmeyer flask covered with a watch glass for 20 hours without stirring Dark blue crystals precipitated out during this time, which were filtered out using filter paper. These crystals were washed with EtOH and diethyl ether then placed in a desiccator under argon to dry.

94

4.2.3 Synthesis of N,N,N-trimethyl(11-mercaptoundecyl)ammonium chloride (TMA) Functionalized Gold Nanoparticles (1.5 nm core)

See Chapter 3 Experimental Section 3.2 for further details.

4.2.4 Synthesis of N,N,N-trimethyl(11-mercaptoundecyl)ammonium chloride (TMA) Functionalized Gold Nanoparticles (4.4 nm core)

See Chapter 2 Experimental Section 2.2 for further details.

4.3 Instrumental

4.3.1 Zeta-potential Measurements (ζ-Pot)

The effective surface charge of varying [Mo-154:Au] solutions were measured on the Malvern Zetasizer ZS in zeta analysis mode with a ζ-potential range of -200 to +200 mV in a folded capillary cell operating at an effective voltage of 150 mV. Data were obtained using the Smoluchowski theory.

4.3.2 Dynamic Light Scattering (DLS)

The size of individual solutions of varying ratio of [Mo-154]:[Au] were performed on the Malvern Zetasizer ZS utilizing a 173° backscattering detector. Individual solutions varying in the ratio of [Mo-154]:[Au] ranged from 0 to the corresponding precipitation point were studied.

4.3.3 UV-visible Spectroscopy (UV-vis)

Optical properties and stability of gold nanoparticle solutions were evaluated in pure water solutions using UV-vis spectroscopy (Varian Cary 50 spectrophotometer) in the wavelength range of 300 to 800 nm with a scan rate of 3000 nm/min. In a typical experiment with Mo-154, solutions from ζ-potential experiments were placed in 1.0 mL glass cuvettes.

4.4   Results and Discussion

4.4.1   Self-assembly of $(NH_4)_{28}[Mo_{154}(NO)_{14}O_{448}H_{14}(H_2O)_{70}] \cdot 350\ H_2O$ with 4.4 nm AuTMA

In Chapters 2 and 3, the self-assembly using various derivatives of the spherical Mo-132 was observed with gold nanoparticles within a specified size domain. We now explore the electrostatic interactions of gold nanoparticles with the non-spherical ring-shaped polyoxomolybdate $(NH_4)_{28}[Mo_{154}(NO)_{14}O_{448}H_{14}(H_2O)_{70}] \cdot 350\ H_2O$ (Mo-154) to further investigate their self-assembly. This study will first describe the equivalence point ratio, [Mo-154]:[Au], of 1.6 and 4.4 nm AuTMA with Mo-154 . Next, a comparison will be made between the equivalence point analysis of Mo-154 and previously investigated Mo-132(a-b). We begin with the observation of the electrostatic assembly of 4.4 nm AuTMA mediated by Mo-154.

Self-assembly is effected by the addition of Mo-154 aliquots to a solution of 4.4 nm AuTMA ([Au] = 0.7 μM) at increasing molar ratios, r = [Mo-154]:[Au] = 1 to 30. The progress of the assembly, the aggregate size, and the charges of the aggregates were monitored *in-situ* with UV-vis, DLS and zeta potential measurements (ζ-Pot). **Figure 4.1** shows the optical absorption characteristics of the assembly system. Because the SPR is sensitive to changes in particle size, local dielectric media changes, as well as coupling between particles in close

proximity, it serves as a convenient method to follow self-assembly. For instance, **Figure 4.1**

shows the UV-visible spectra of Mo-154, 4.4 nm AuTMA, and the Mo-154+AuTMA

electrostatic assemblies. At $r > 6$, a subtle red-shift is observed, as well as a decrease in

extinction, which is attributed to the assembly of the relatively small AuTMA-Mo-154 clusters,

followed by the spontaneous precipitation of the AuTMA-Mo-154 aggregates occuring at $r \approx 8$.
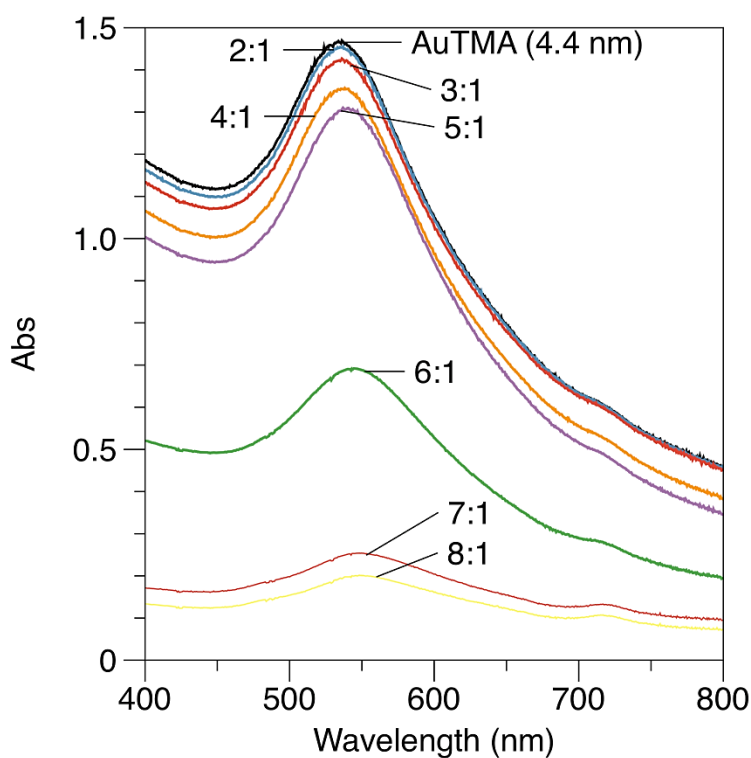
Figure 4.1: Representative UV-vis spectra of Mo-154, 4.4 nm AuTMA, and AuTMA+Mo-154 assemblies at r = [Mo-154]:[Au] = 2:1, 3:1, 4:1, 5:1, 6:1, 7:1, and 8:1.
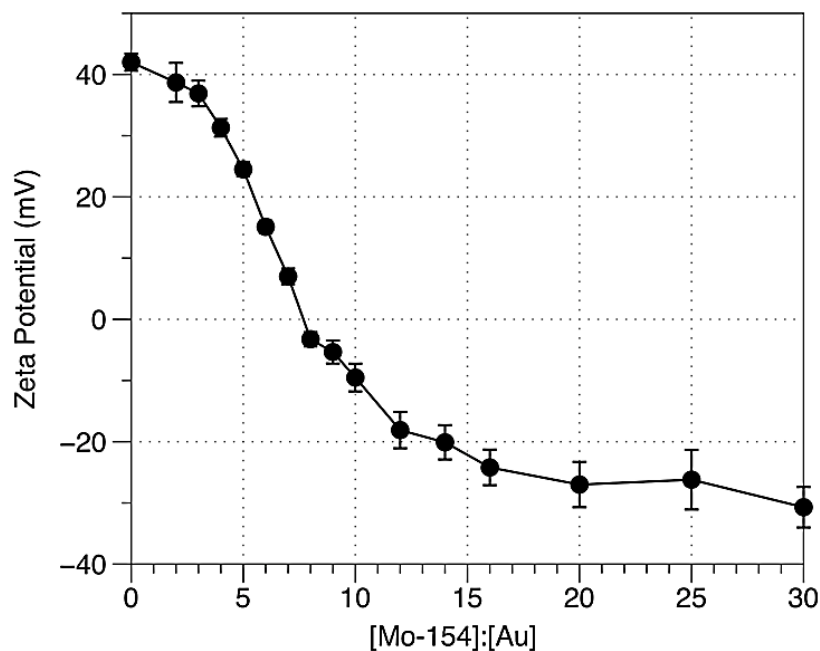
Figure 4.2: Zeta potential (ζ-pot.) measurements for Mo-154 mediated assembly of 4.4 nm AuTMA at increasing r = [Mo-154]:[Au].

Figure 4.2 demonstrates a set of ζ-Pot measurements for the Mo-154 + AuTMA system at increasing r. The initial 4.4 nm AuTMA particle has a charge of ζ = 42.0 ± 1.39 mV, which is consistent with previous studies.[28-34] This value decreases slowly at r = 0 to 3, which is indicative to the interaction between Mo-154 with AuTMA as the charges are screened. At $r > 3$ a decrease in ζ is detected, with neutralization ($\zeta \approx 0$ mV) occurring at $r \approx 8$. At $r > 8$ there is a negative overall charge ($\zeta \approx$ -30 mV) which remains relatively invariant, due to both the presence of excess Mo-154, as well as the likelihood that each assembled aggregate is terminated by it. This trend towards electroneutrality corresponds closely with the bulk precipitation observed via UV-vis **(Figure 4.3).**
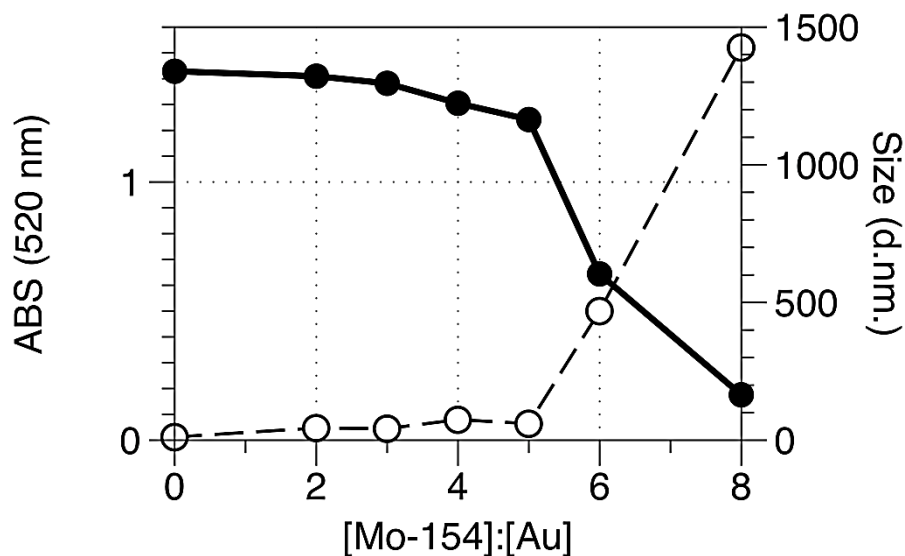
Figure 4.3: Absorbance maxima at 520 nm and hydrodynamic radius (D_h) corresponding to the self-assembly of Mo-154 and 4.4 nm AuTMA, where absorbance decreases as [Mo-154]:[Au] increases to $r = 8$ and D_h increases with r.

For example, **Figure 4.3** shows a plot of the SPR absorbance maxima (520 nm), measured in parallel to ζ -Pot measurements. At $r = 8$, a drop in absorbance is detected, correlating with the aggregation. The hydrodynamic properties of the system were then probed by DLS. **Figure 4.3** shows a plot of hydrodynamic diameter (D_h) with r. As observed above, rapid aggregate growth to $D_h > 1400$ nm was measured at $r \approx 8$.

The results were in good agreement to data previously shown in Chapter 2, where the r_{E0}, ratios at the point of electroneutrality for Mo-132a of charge -42 and Mo-132b of charge -72 were 10 and 14, respectively.[34] Just as in Chapter 2, the assembly between 4.4 nm AuTMA and Mo-154 involves the displacement of Cl^- and NH_4^+ counter-ions in the double layer. Since the relative charge of -28 mV for Mo-154 requires a lower concentration of NH_4^+ counter-ions and

weaker coulombic attraction, it in turn strengthens the attraction for 4.4 nm AuTMA and increases kinetics. This resulted in a lower equivalence point of $r_{E0} \approx 8$.

4.3.2 Self-assembly of $(NH_4)_{28}[Mo_{154}(NO)_{14}O_{448}H_{14}(H_2O)_{70}] \cdot 350\ H_2O$ with 1.6 nm AuTMA

For self-assembly between Mo-154 and 1.6 nm AuTMA, aliquots of Mo-154 were added to a solution of AuTMA ($[Au] = 47.5\ \mu M$) at increasing molar ratios of $r = 0.2\text{-}0.9$. **Figure 4.4** shows the optical absorption characteristics of Mo-154, AuTMA, and the Mo-154+AuTMA electrostatic assemblies in the UV-visible spectra. At $r < 0.25$, an increase in extinction is observed, which is attributed to the addition of Mo-154 in solution. When $r > 0.25$ assembly of the relatively small AuTMA-Mo-154 clusters produces a decrease in extinction, followed by the growth of a large aggregate at $r \approx 0.4$. This decrease in extinction is attributed to both the screening of interior particles, as well as precipitation of the material from solution. The spontaneous precipitation of the AuTMA-Mo-154 aggregates occurs at $r \approx 0.4$.
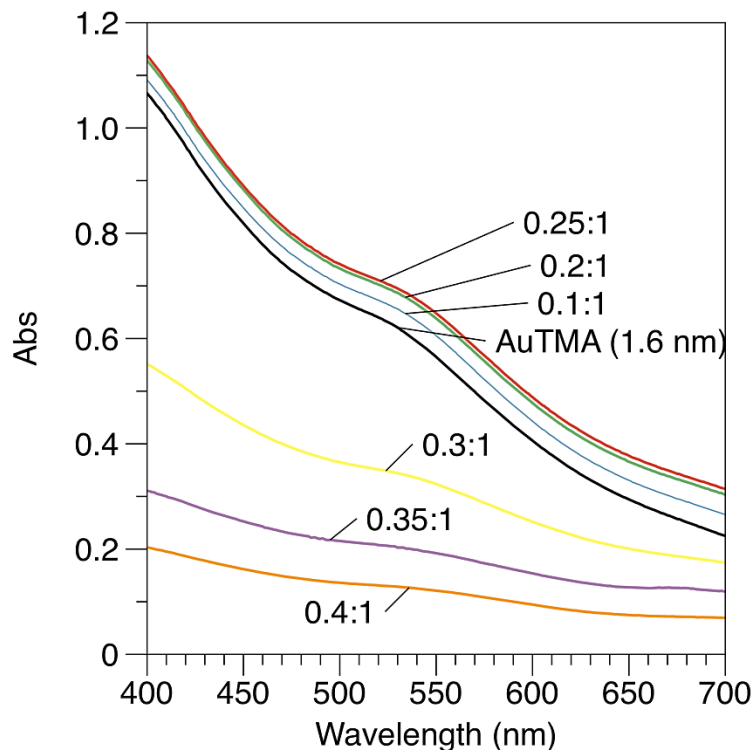
Figure 4.4: Representative UV-vis spectra of Mo-154, 1.6 nm AuTMA, and AuTMA+Mo-154 assemblies at r = [Mo-154]:[Au] = 0.2:1, 0.25:1, 0.3:1, 0.35:1, and, 0.4:1.

Figure 4.5 shows a set of ζ-Pot measurements for the Mo-154 + AuTMA system at increasing r. The initial 1.6 nm AuTMA particle has a charge of $\zeta = 40.3 \pm 2.92$ mV. This value decreases slowly at $r = 0$ to 0.3, indicative of the charge screening of the interaction between Mo-154 with AuTMA. At $r > 0.3$ a decrease in ζ is detected, with neutralization ($\zeta \approx 0$ mV) occurring at $r \approx 0.4$. At $r > 0.4$ there is a negative overall charge ($\zeta \approx -30$ mV) due to the presence of excess Mo-154, as well as the likelihood that each assembled aggregate is terminated by the negatively charged particle. This trend towards electroneutrality corresponds closely with the bulk precipitation observed via UV-vis **(Figure 4.6).**
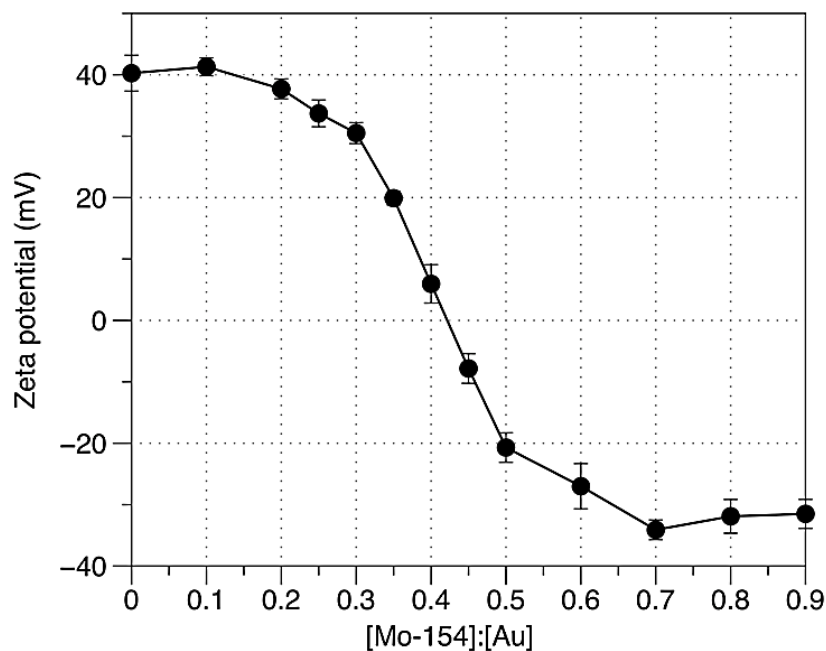
Figure 4.5: Zeta potential (ζ-pot.) measurements for Mo-154 mediated assembly of 1.6 nm AuTMA at increasing r = [Mo-154]:[Au].

In **Figure 4.6**, a plot of the SPR absorbance maxima (520 nm), measured in parallel to ζ -Pot measurements is depicted. At r = 0.35, a drop in absorbance is detected, correlating with the onset of aggregation. The hydrodynamic properties of the system were then probed by DLS, where a plot of hydrodynamic diameter (D_h) with r shows rapid aggregate growth to D_h > 4000 nm at $r \approx 0.4$.
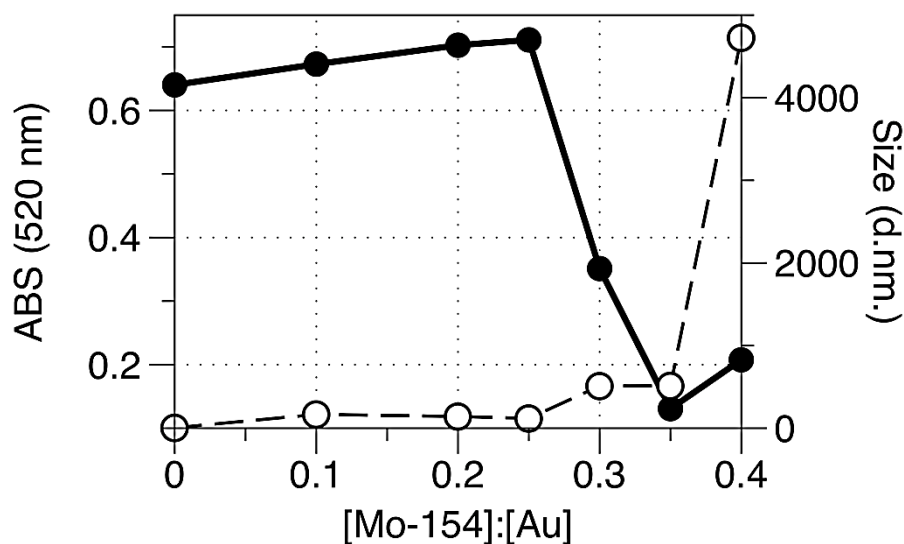
Figure 4.6: Absorbance maxima at 520 nm and hydrodynamic radius (D_h) corresponding with the self-assembly of Mo-154 and 1.6 nm AuTMA, where absorbance decreases as [Mo-154]:[Au] increases to $r = 0.4$ and D_h increases with r.

These results appear counterintuitive to our findings with respect to 1.6 nm AuTMA in Chapter 3, in which we observed a r_{E0} of 1 for a Mo-132a of charge -42 and r_{E0} of 0.6 for Mo-132b with a charge of -72. The lower charge of -28 for Mo-154 would presumably be expected to have a higher r_{E0} than 1. However, with an observed r_{E0} of 0.4, the introduction of the Mo-154 Keggin ion introduces some profound questions about the role of shape in these self-assemblies. It can be suggested that the size and shape of the Mo-154 structure has a degree of contribution to the lower r_{E0}. Several theories may be proposed to account for each of these contributions: (1) regions of higher electron density around the periphery of the ring may lead to a stronger attraction force with the cationic trimethylamine groups of AuTMA. (2) Compared to the spherical shape of the Mo-132 (a,b), the ring shape of the Mo-154 may allow for reduced repulsion of counter-ions in the double layer due to the presence of the ~1.5 nm inner cavity of the ring. This theory may be plausible because compared to a spherical hydrodynamic radius of

103

both the Mo-132(a,b) and 1.6 nm AuTMA, the Mo-154 will have a unique hydrodynamic radius

with a thinner radius around the inner cavity, which may allow for counter-ions to flow freely

through its central "void". The most plausible explanation for such results may be (3) the van

der Waals interactions between Mo-154 and 1.6 nm AuTMA are stronger than those with Mo-

132 (a,b). **Figure 4.7** illustrates the results of calculations of the van der Waals attraction forces.
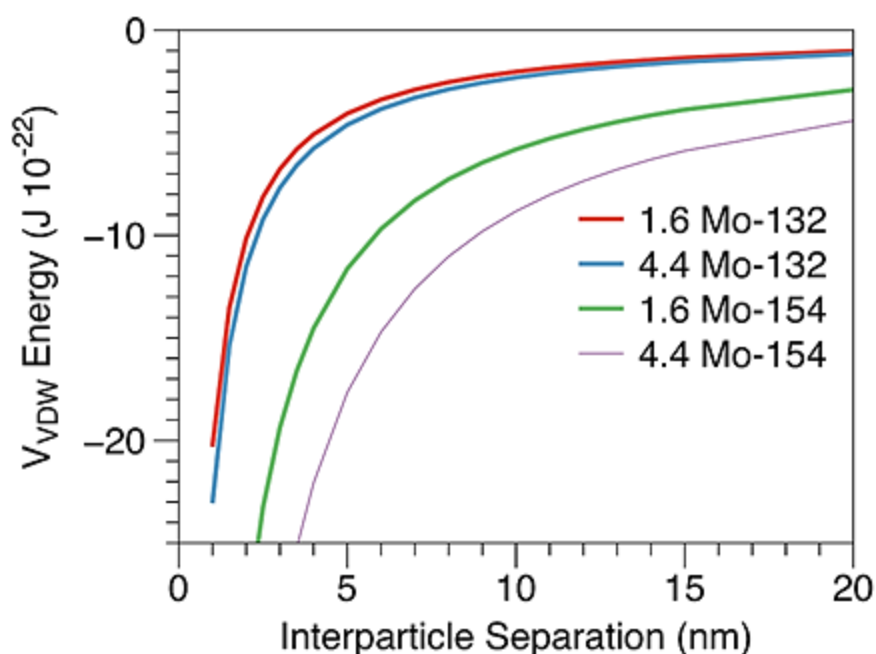
Figure 4.7: Comparison of van der Waals attraction forces of AuTMA of size 1.6 and 4.4 nm
with Mo-132a and Mo-154. It is observed that Mo-154 has a stronger attraction force which
may lead to charge compensation at lower r_{E0}.

      Figure 4.7 represents the van der Waals attraction potentials for gold nanoparticles of 1.6

and 4.4 diameters with Mo-132 and Mo-154. The gold Hamaker constant (A_{Au-Au}) from the

literature varies from $1 - 4 \cdot 10^{-19}$ J; therefore the average of $A_{Au-Au} = 2.5 \cdot 10^{-19}$ J was used. [35,36] To

the author's knowledge, no previous literature prior to this work documented a Hamaker constant

of either Mo-132, Mo-154, or MoO_3, Therefore the Hamaker constant for WO_3 from the literature was used, with $A_{W-O} = 2.1 \cdot 10^{-20}$ J.[36] Since Hamaker constants of metal oxides are in the range of $1\text{-}3 \cdot 10^{-20}$ J, this value was judged adequate for Mo-132 and Mo-154.

$$A = \sqrt{(A_{Au} \cdot A_{Mo})^2} \quad \text{Eq. 1}$$

For the van der Waals interactions between gold nanoparticles and Mo-132, Equation 2 for sphere-sphere interactions is used.

$$V_{vdW} = -\frac{A}{6}\left[\frac{2a_1 a_2}{R^2 - (a_1 + a_2)^2} + \frac{2a_1 a_2}{R^2 - (a_1 - a_2)^2} + ln\left(\frac{R^2 - (a_1 + a_2)^2}{R^2 - (a_1 - a_2)^2}\right)\right] \text{Eq. 2}$$

However, for the approximation of gold nanoparticles interacting with Mo-154, a different van der Waals equation must be used due to the non-spherical shape of Mo-154. Equation 3 describes the interactions between a sphere and a flat surface.[37-39] It is assumed that in the case that the flat surface of Mo-154 is interacting with AuTMA. **(Scheme 4.1(c))**

$$V_{vdW} = -\frac{Aa}{6R}\left[1 + \frac{R}{2a+R}\right] \text{Eq. 3}$$

where a is the radius of AuTMA, R is the internuclear separation distance between the two nanomaterials, A is the Hamaker constant.

The interaction of AuTMA with Mo-154 is much greater than AuTMA with Mo-132. This clearly suggests that even though Mo-154 has a lower negative charge than Mo-132 (a,b), differences in van der Waals attraction forces play a predominant role in self-assembly of 1.6 nm AuTMA.

4.5   Conclusions

In summary, the electrostatic assembly between Mo-154 and gold nanoparticles was investigated for the first time, and successful assembly was demonstrated using UV-vis, DLS, and ζ-Pot analysis. The rapid bulk precipitation from nanoscopic entities to micron scale aggregates was observed at the point of electroneutrality, which was dependent upon the [Mo-154]:[Au] molar ratio. In comparison to results reported in Chapter 2 and 3, these findings indicate that shape plays an important role in the self-assembly process, where the equivalence point is related to charge balance and van der Waals forces of the nanomaterials. Furthermore, the findings suggest that investigations of AuTMA of different dimensions, modified charges and nonspherical shapes in combination with polyoxomolybdates of different dimensions and charges may lead to novel suprastructures with advanced optical, electronic, and catalytic properties.

4.6　References

[1]　C. Burda, X. Chen, R. Narayanan, M.A. El-Sayed, *Chem. Rev.* **2005,** 105, 1025-1102.

[2]　R.M. Fratila, S. Rivera-Fernández, J.M. de la Fuente, *Nanoscale* **2015**, 7, 8233-8260.

[3]　G. Chen, J. Seo, C. Yang, P.N. Prasad, *Chem. Soc. Rev.* **2013**, 42, 8304-8338.

[4]　A. Albanese, P.S. Tang, W.C.W. Chan, *Annu. Rev. Biomed. Eng.* **2012,** 14, 1-16.

[5]　A.P. Alivisatos, *ACS Nano* **2008,** 2, 1514–16.

[6]　S. Campione, C. Guclu, R. Ragan, F. Capolino, *ACS Photonics* **2014**, 1, 254−260.

[7]　Shevchenko, E.; Talapin, D.V.; Kotov, N.A.; O'Brien, S.; Murray, C.B. *Nature* **2006**, 438, 55-59.

[8]　J.A. Fan, K. Bao, L. Sun, J. Bao, V.N. Manoharan, P. Nordlander, F. Capasso, *Nano Lett.* **2012**, 12, 5318−5324.

[9]　*Encyclopedia of Surface and Colloid Science 2nd Ed.* **2012,** Taylor&Francis, Boca Raton, Fl., 6183-6207.

[10]　C.M. Knoedler. *J. Appl. Phys.* **1990,** 68, 1129-1137.

[11]　Z.G. Li, P.J Fagan, L. Liang, *Chemical Physics Letters.* **1993,** 207, 148–152.

[12]　H. Dai, E.W. Wong, Y.Z. Lu, S. Fan, C.M. Lieber, *Nature.* **1995,** 375, 769-772.

[13]　R. Liu, F. Oba, E.W. Bohannan, F. Ernst, J.A. Switzer, *Chem. Mater.* **2003,** 15, 4882-4885.

[14]　F.M. van der Kooij, K. Kassapidou, H.N.W. Lekkerkerker, *Nature.* **2000,** 406, 868-871.

[15]　L-H. Gao, X. Chen, L. Shan, K-Z. Wang, *J. Nanoscience Nanotechnology.* **2014,** 14, 5, 3808-3812.

[16]　P.F. Damasceno, M. Engel, S.C. Glotzer, *Science.* **2012,** 337, 453-457.

[17]　S.C. Glotzer, M.J. Solomon, *Nature Materials* **2007,** 6, 557-562.

[18]　a) C. Kaittanis, S.A. Naser, J.M. Perez, *Nano Letters.* **2007,** 2, 7, 380-383. b) S. Nath, C. Kaittanis, S. Ramachandran, N.S. Dalal, J.M. Perez, *Chem. Mater.* **2009,** 291, 1761-1767.

[19]　L. Cademartiri, K.J.M. Bishop, P.W. Snyder, G.A. Ozin, *Phil. Trans. R. Soc. A* **2012,** 370, 2824-2847.

[20] X. Ye, J.A. Millan, M. Engel, J. Chen, B.T. Diroll, S.C. Glotzer, C.B. Murray, *Nano Lett.* **2013**, 13, 4980−4988.

[21] X. Ye, J. Chen, M. Engel, J.A. Millan, W. Li, L. Qi, G. Xing, J.E. Collins, C.R. Kagan, J. Li, S.C. Glotzer, C.B. Murray, *Nature Chem.* **2013**, 5, 466-473.

[22] K.J.M. Bishop, C.E. Wilmer, S. Soh, B.A. Grzybowski, *Small* **2009,** 5, 14, 1600-1630.

[23] D.A. Walker, C.E. Wilmer, B. Kowalczyk, K.J.M. Bishop, B.A. Grzybowski, *Nano Lett.* **2010,** 10, 2275–2280.

[24] D.A. Walker, E.K. Leitsch, R.J. Nap, I. Szleifer, B.A. Grzybowski, *Nature Nanotechnology* **2013,** 8, 676-681.

[25] A. Müller, E. Krickemeyer, J. Meyer, H. Bögge, F. Peters, W. Plass, E. Diemann, S. Dillinger, F. Nonnenbruch, M. Randerath, C. Menke, *Angew. Chem. Int. Ed. Engl.* **1995***, 34*, 2122-2124.

[26] A. Müller, C. Serain, *Acc. Chem. Res.* **2000***, 33*, 2-10.

[27] A. Müller, *Chemical Intelligencer*: Springer-Verlag: New York, **1997**.

[28] A.M. Kalsin, M. Fialkowski, M. Paszewski, S. K. Smoukov, K. J. M. Bishop, B. A. Grzybowski, *Science* **2006,** 420-424.

[29] A.M. Kalsin, A.O. Pinchuk, S. K. Smoukov, M. Paszewski, G. C. Schatz, B. A. Grzybowski, *Nano. Lett.* **2006**, 6, 1896-1903.

[30] A.M. Kalsin, B. Kowalczyk, S. K. Smoukov, R. Klajn, B.A. Grzybowski, *J. Am. Chem. Soc.* **2006,** 15046-15047.

[31] P. D. Yates, G. V. Franks*,* S. Biggs, G. J. Jameson, *Colloids Surf. A-Physicochem. Eng. Asp.* **2005**, 255, 85-90.

[32] C.-C. You, M. De, V. M. Rotello, *Curr. Opin. Chem. Bio.* **2005**, 9, 639-646.

[33] J. Kolny, A. Kornowski, H. Weller, *Nano. Lett.* **2002**, 2, 361-364.

[34] Gooch, J.; Anan, A.; Jones, S.; Hine, C.R.; Alam, R.; Garai, S.; Maye, M.M.; Müller, A.; Zubieta, J. *J. Colloid Interface Sci.* **2014,** 432, 144-150.

[35] Biggs, S.; Chow, M. K.; Zukoski, C. F.; Grieser, F. *J. Colloid Interface Sci.* **1993**, 160, 511.

[36] Anderson, K. **2004**. *Aqueous Processing of WC-Co Powders*. Doctoral Dissertation.

[37] R.J. Hunter, *Foundations of Colloid Science*; Clarendon Press: Oxford, U.K., **1992.**

[38] B.V. Derjaguin, *Kolloid Zeits* **1934**, 69, 155-164.

[39]   J.N. Israelacvili, *Intermolecular and Surface Forces 3rd Ed.*; Academic Press: London **2011.**

Chapter 5

Conclusions and Future Outlook

5.1   Conclusions

The description of this research detailed the investigations of electrostatic assembly of

gold nanoparticles (AuNPs) mediated by the giant polyoxomolybdate clusters

$(NH_4)_{42}[\{(Mo^{VI})Mo^{VI}_5O_{21}(H_2O)_6\}_{12}\{Mo^V_2O_4(CH_3COO)\}_{30}] \cdot \approx 300\ H_2O \cdot \approx 10\ CH_3COONH_4$

(Mo-132a), $(NH_4)_{72}[\{(Mo^{VI})Mo^{VI}_5O_{21}(H_2O)_6\}_{12}\{Mo^V_2O_4(SO_4)\}_{30}] \cdot \approx 200\ H_2O$ (Mo-132b) and

$Na_{10}(NH_4)_{62}[\{(Mo^{VI})Mo^{VI}_5O_{21}(H_2O)_6\}_{12}\{Mo^V_2O_4(HPO_4)\}_{30}] \cdot \approx 300\ H_2O \cdot \approx 2Na^+ \cdot \approx 2NH_4^+ \cdot \approx 4$

H_2PO_4 (Mo-132c) and $(NH_4)_{28}[Mo_{154}(NO)_{14}O_{420}(OH)_{14}(H_2O)_{70}] \cdot 350\ H_2O$ (Mo-154). These

studies have shown the successful assembly between AuNPs and this series of anionic clusters.

These self-assembled systems have revealed the effects of size, shape, and ionic strength on the

electrostatic assembly between the nanomaterials. Furthermore, we have shown that the

crystallization process between these nanomaterials is dependent on charge and size

compatibility.

Table 5.1: Summary of r_{E0} values for the varying AuNPs and different types of POM clusters

Gold Size (nm)	r_{E0}^a = [Mo]:[Au]			
	Mo-132a	Mo-132b	Mo-132c	Mo-154
	(2.9 nm, Q = -42)	(2.9 nm, Q = -72)	(2.9 nm, Q = -72)	(3.5 nm, Q = -28)
1.6	1.0	0.6	-	0.4
4.4	10	14	14	8
8.6	28	33	-	-

a r_{E0} is the molar ratio between the Mo species and Au species at the equivalence point

In Chapter 2, a series of anionic Mo-132 Keplerates with different charges were

synthesized and characterized as well as AuNPs functionalized with a self-assembled monolayer

(SAM) of cationic thiolate N,N,N-trimethyl(11-mercaptoundecyl)ammonium chloride (TMA)

ligands. A detailed investigation of the electrostatic assembly of AuNPs mediated by various

polyoxomolybdate clusters of the Keplerate class demonstrated successful assembly using UV-vis, DLS, TEM, and ζ-Pot analysis. The rapid bulk precipitation from nanoscopic entities to micron scale aggregates was observed at the point of electroneutrality, which was typically at a [Mo-132]:[Au] molar ratio of 10~14 depending on the ligand associated with Mo-132. These results indicate that precipitation at the equivalence point is related to charge balance or electroneutrality and that counter-ions at both the Mo-132 and AuNP play a significant role in assembly.

In Chapter 3, we observed that electrostatic assembly of AuNP core diameter of 8.6 nm mediated by Mo-132a and Mo-132b gave r_{E0} values of $\approx$ 35 and 45, respectively. The behavior of AuNPs of 8.6 nm core diameter suggests a correlation between counter-ions and the deflection angles of the ligands of the AuNPs. Furthermore, we learned that two key parameters control the crystallization process. (1) The charge on both entities must be of equal magnitude ($Q^+ = Q^-$) and (2) The size of both entities must be approximately equivalent. Electrostatic assembly of cationic AuNPs of 1.6 nm core diameter with Mo-132 resulted in $r_{E0} \approx 1.0$ for the 1.6 nm AuTMA+ Mo-132a system which suggests that one of these key parameters has been realized. Since amorphous aggregates still occurred for this system, size equivalence should also be considered.
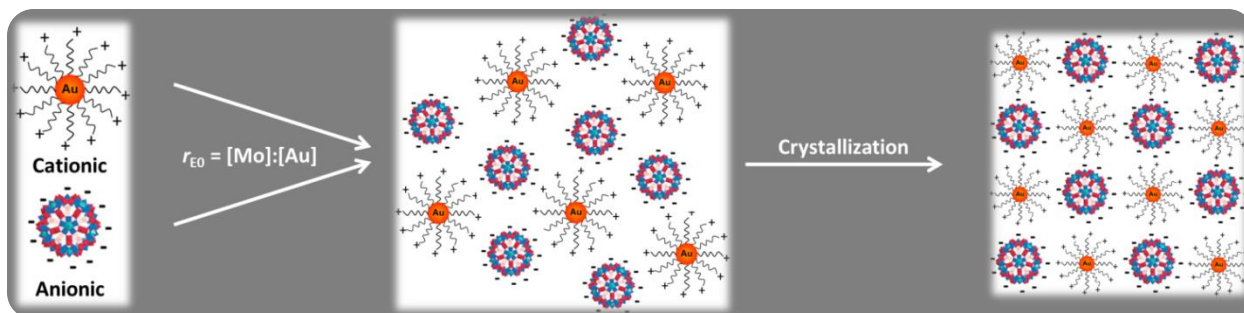
Scheme 5.1: An idealized representation of the proposed mechanism for the crystallization of cationic AuNPs and anionic POM clusters. When r_{E0} is achieved and aggregation of unorganized AuNPs and POM occurs, crystallization can take place under certain conditions. This may include the heating of the solution with addition of other solvents, such as DMSO, to control the solubility and allow for organization of the entities to occur.

In the fourth Chapter, the electrostatic assembly between Mo-154 and gold nanoparticles was investigated for the first time, and successful assembly was demonstrated using UV-vis, DLS, and ζ-Pot analysis. The rapid bulk precipitation from nanoscopic entities to micron scale aggregates was observed at the point of electroneutrality, which was dependent upon the [Mo-154]:[Au] molar ratio. In comparison to results reported in Chapter 2 and 3, these findings indicate that shape plays an important role in the self-assembly process, where the equivalence point is related to charge balance and van der Waals forces of the nanomaterials. Specifically, an observed $r_{E0} \approx 8$ for AuNPs of 4.4 nm core diameter mediated with Mo-154 was in good agreement, in terms of polyoxomolybdate surface charge, with observed values of $r_{E0} \approx 10$ and $r_{E0} \approx 14$ for Mo-132a and Mo-132b, respectively. AuNPs of 1.6 nm core diameter mediated with Mo-154 gave an $r_{E0} \approx 0.4$, which cannot be explained by polymolybdate surface charge alone. Therefore, van der Waals attractive forces were calculated to reveal a stronger attractive force for the ring shaped Mo-154 compared to the spherical Mo-132, which may explain the lower r_{E0}.

5.2 Future Outlook
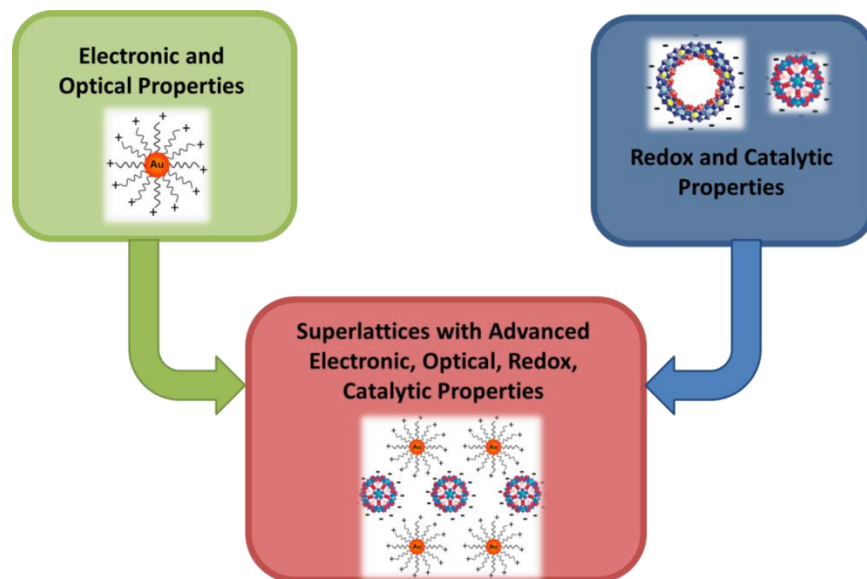
Scheme 5.2: Illustration depicts the proposed advancement in electronic, optical, redox, and catalytic properties of AuNPs and POM systems when organization of aggregates occurs.

The optical properties of AuNPs combined with the reduction-oxidation and catalytic properties of Mo-132 may lead to fascinating novel superlattice structures. The research in this dissertation provides the framework for understanding and forming such structures. Future studies may focus on parameters such as size uniformity, where one must not only take into account the core diameter, but include the TMA ligands (~1.9 nm). When these are taken into account, the AuNP core diameters of 1.6, 4.4, and 8.6 nm expand to ca. 5.4, 8.2, and, 12.4 nm, respectively. These observations are relevant for the pursuit of crystalline composites, and the next step in these studies is to synthesize a gold nanoparticle of ~3.0 nm diameter when the ligand length is included. At 0.8 nm, 2-aminoethanethiol has the desired length to yield AuNPs of approximately 3.2 nm in diameter, if the AuNP core diameter had dimensions of 1.6 nm. The difficulty with attaching a thiol of this length involves the stability of the Au-S bond. In general,

AuNPs remain stable in solution due to electrostatic repulsion and steric hinderance of the ligands. Shorter alkane thiols lack high chemical stability against displacement because of low packing densities, low order, and decreased thickness of the inner hydrophobic shell. This allows for a decrease in the electrostatic repulsion of AuNPs, which results in particle coagulation. Nevertheless, preliminary results of this synthesis have had some success yielding a 2-aminoethanethiol capped AuNP with a cationic charge between 45 and 50 mV.

For crystallization to occur with electrostatic, either the assembly process must have slower kinetics or the assembled aggregates must be allowed to reorganize to allow for crystal lattices to form. The former could be done through means of a combination of higher ionic strength solutions and sucrose gradient ultracentrifucation, where the viscosity of the surcose layer slows the kinetic interactions between AuNPs and Mo-132. The ionic strength would allow for more charge screening as seen in Chapter 2, but a wash process may be needed to rid the materials of excess ions around the aggregates. This is where assembled aggregates may need to go through a wash process, where removal of Cl^- and NH_4^+ ions allows for higher levels of purity in the crystal lattice. To obtain the crystal lattice after wash, a heated mixed solvent, such as $DMSO:H_2O$, may allow for individual AuNPs and Mo-132 to reorganize within the aggregate and develop a ordered structure. Methods such as SEM and SAXS can provide evidence of any crystallinity.

Another study of interest would involve using Cd/Se quantum dots in exchange for AuNPs. Utilizing TMA capped Cd/Se quantum dots as a mediator for the electrostatic self-assembly of Mo-132 clusters may provide interesting flouresence and energy transfer studies. Similar to AuNPs, Cd/Se quantum dots possess unique physiochemical and optoelectronic properties that allow for a wide range of applications. One difference between AuNPs and Cd/Se

quantum dots involves their optical properties. Unlike AuNPs, which have a relatively simliar

SPR with change to diameter, Cd/Se quantum dots go through a wide range of colors throughout

the UV-visible and even IR regions of the electromagnetic spectrum. This property is in large

part due to the quantum confinement of energy levels in the density of states (**Figure 5.1**). For

smaller Cd/Se quantum dots, quantum confinement can also manipulated by the growth of the

Cd/Se shell, yielding varying sized quantum dots.
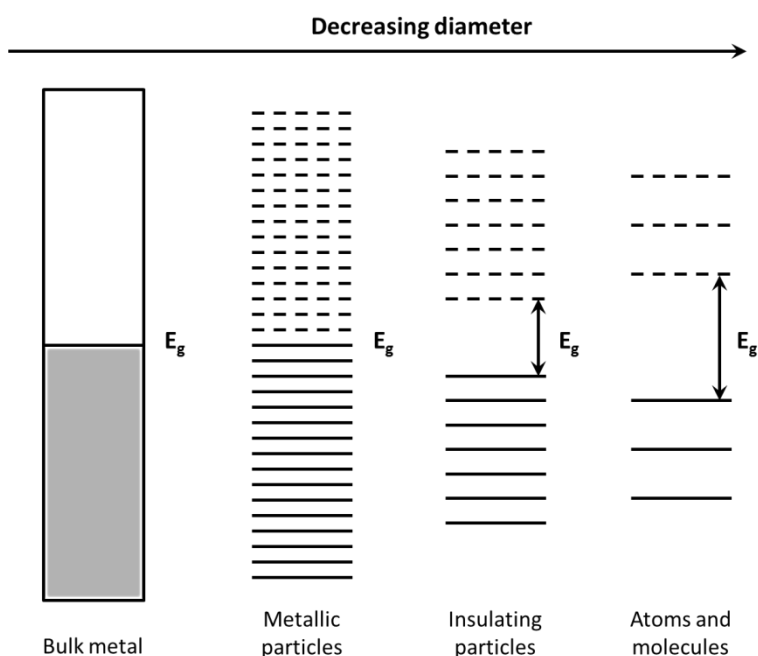
Decreasing diameter

E_g E_g E_g E_g

Bulk metal   Metallic particles   Insulating particles   Atoms and molecules

Figure 5.1: Illustration of the density of states. For bulk metals, condensed energy levels lead to formation of the valence and conduction band. As diameter of particles decreases, these energy levels separate and form discrete energy levels which yield a band gap (E_g).

Excited quantum dots typically display a Stokes shift, where the emitted radiation has a

lower frequency than the absorbed radiation. This is present when the electron is excited above

the first vibrational level of the excited state and non – radiative vibrational relaxation can occur

before radiative electronic relaxation to minimize the lifetime of the excited state. Depending on

the application, a smaller or larger stokes shift is preferred. For self-assembly and energy transfer applications, a small stokes shift is desired to minimize non-radiative energy losses, decrease co-excitation and increase the amount of energy available for the system.

Furthermore, the findings in Chapter 4 suggest that investigations of AuNPs of different dimensions, modified charges, and nonspherical shapes in combination with polyoxomolybdates of variable dimensions and charges may lead to fascinating novel superstructures with advanced optical, electronic, and catalytic properties. The ability to engineer and design structures by using the anisotropic dimensions of building blocks gives a powerful tool in creating specifically targeted structures of particular shape and size. Our investigations have shown the complexity of designing such super structures with the spherical Mo-132 clusters. However, utilizing the ring-shape of Mo-154 can lead to denser crystal lattice packing, which may eradicate excess counter ions that may be hindering the crystallization process. If crystallization does occur within the Mo-132 clusters with AuNPs, then Mo-154 would also lead to varying types of lattice structures.

There is an abundant amount of possibilities that these systems can contribute to the scientific community. Utilization of AuNPs is seen across a wide spectrum, such as electronics, where they are used to connect resistors and conductors in electronic chips. They are also seen in photodynamic, sensory, and other imaging applications utilizing their optical properties. Potential applications for polyoxomolybdates range from catalysts using their reduction-oxidation properties to storage devices for energy storage and conversion. It has also been reported that the distinct size of the Mo-132 pores and cavities allows for chemistry to be conducted inside these structures.

To conclude, AuNPs and giant polyoxomolybdates have made remarkable advancements in the scientific community. Combined together these nanoscopic entities open up possibilities for even more fascinating discoveries.

Jonathan Gooch

1-014 Center for Science and Technology
111 College Place, Syracuse, NY 13244
(570) 878-2984
jwgooch@syr.edu

Education

PhD.   Chemistry, Syracuse University, Syracuse, New York, August 2015
Advisor: Professor Jon A. Zubieta
Investigations of the *Electrostatic Assembly of Gold Nanoparticles Mediated with Giant Polyoxomolybdate Clusters*

M.Phil. Chemistry, Syracuse University, Syracuse, New York, April 2012
Advisor: Professor Jon A. Zubieta
Electrostatic Assembly of Gold Nanoparticles Mediated with the Polyoxometalate Mo-132

B.S.   Chemistry, Misericordia University, Dallas, Pennsylvania, May 2010
Identification of Cellulose-Degrading Enzyme Using Bioassay-Guided Fractionation
Advisor: Professor Xuegang Jia

Research Portfolio

- Synthesis and purification of gold nanoparticles including Au sizes of 1.6, 4.4, and 8.6 nm
- Synthesis and characterization of polyoxometalates systems including Mo-12, Mo-132, and Mo-154 derivatives.
- Ligand exchange mechanisms of Au precursors with alkyl thiols.
- Observed electrostatic assembly of Au nanoparticles and polyoxometalates by UV-visible, Dynamic Light Scattering, and Zeta Potential Analysis.
- Characterization of Au nanoparticles, polyoxometalates, and other small molecules using a full scope of instrumentation.
- Hydrothermal synthesis of transition metals, phosphonate ligand derivatives, and nitrogen based ligands.

Training

Instrumentation:	Single Crystal X-ray Diffractometer, Zetasizer Nano Z, Dynamic Light Scattering, Transmission Electron Microscopy,

Thermogravimetric Analysis, NMR Spectroscopy, Infrared
Spectroscopy, and, UV-visible Spectroscopy.

Relevant Work Experience

Fall 2010-present   Graduate Teaching Assistant, Syracuse University, Syracuse, NY
- **Physical Chemistry Lab**: Preparation of weekly experiments.
  Teaching concepts on experiments. Helping students throughout
  the lab. Grading lab reports. Holding office hours to assist
  students with questions. Consisted of 8-12 students. (2 semesters)
- **Organic Chemistry Lab**: Preparation of weekly experiments.
  Teaching concepts on experiments. Helping students throughout
  the lab. Grading lab reports. Consisted of 24 students. (1
  semester)
- **General Chemistry Recitation**: Teaching concepts from lecture
  by reviewing end of chapter problems and Mastering Chemistry.
  Holding office hours to assist students with questions. Consisted
  of sections of 25 students. (3 semesters)
- **General Chemistry Honors Recitation**: Teaching concepts from
  lecture by reviewing end of chapter problems. Teaching the
  lecture while the professor was unavailable. Holding office hours
  to assist students with questions.   Consisted of 20-40 students. (4
  semesters)

Spring 2009   Senior Research Experience, Misericordia University, Dallas, PA
- Conducted independent research under advisor Dr. Xuegang Jia
- Project title: *Identification of Cellulose-Degrading Enzyme Using
  Bioassay-Guided Fractionation*

Publications

Gooch, Jonathan; Jalan, Abhishek A.; Jones, Stephanie; Hine, Corey R.; Alam, Rabeka; Garai,
Somenath; Maye, Mathew M.; Müller, Achim; Zubieta, Jon, *Keplerate cluster (Mo-132)
mediated electrostatic assembly of nanoparticles*. Journal of Colloid and Interface Science, 432,
2014, 144-150.

Gooch, Jonathan; Walter, Shannon; Maye, Mathew M.; Zubieta, Jon, *Electrostatic assembly of
various sized nanoparticles mediated by Mo-132 Keplerate cluster.* **2015.** (Working Title - In
preparation)

Ruggiero, Michael T.; **Gooch, Jonathan**; Zubieta, Jon; Korter, Timothy M., *The Role of Both
Long and Short Range Corrected Hartree-Fock Exchange on Pi-Stacking in Pyridinium Ring
Systems.* (Working Title -In Preparation)

Ouellette, Wayne; Luquis, Stephanie; **Gooch, Jonathan**; Zubieta, Jon A. *Anion Influences On The Solid State Coordination Chemistry of Copper-bispyrazole Materials*.**2014** (Accepted in Inorganica Chimica Acta)

Smith, Tiffany M.; Zhang, Y.-Z.; **Gooch, Jonathan**; Lau, Adam; McLeish,Sharde; Dunbar, Kim R.; Zubieta, Jon A. *Hydrothermal syntheses and structures of cobalt(II) and copper(II) coordination polymers with 1-tetrazole-phenyl-4-methylphosphonate ligands*.